

The copyright of this thesis vests in the author. No quotation from it or information derived from it is to be published without full acknowledgement of the source. The thesis is to be used for private study or non-commercial research purposes only.

Published by the University of Cape Town (UCT) in terms of the non-exclusive license granted to UCT by the author.

**AN INVESTIGATION INTO THE FIBRE INSTRUMENT
FEED FOR THE SOUTHERN AFRICAN LARGE
TELESCOPE (SALT)**

Nicholas James Adam Sessions, BSc (Eng), University of Cape Town

February 2001

Submitted to the University of Cape Town in partial fulfilment for the degree of
Master of Science in Engineering.

ABSTRACT

This thesis is an investigation into the Fibre Instrument Feed (FIF) for SALT. Its goal is to provide the groundwork that will lead to the detailed design and manufacture of such an instrument that is to be completed by the time SALT is commissioned in mid-2004.

Three major parts are presented.

The first part provides a background to the investigation. It begins with an introduction to telescope design and optical concepts. It then gives a brief history and discussion of the Hobby-Eberly Telescope (HET), on which the design of SALT is based. That being a fixed-altitude, segmented spherical primary mirror, which is restricted to observing objects that pass through a "window" 12° wide offset from the vertical. This design also means that the light collecting area of the telescope (the pupil) moves off the primary mirror array, changing in size and shape, to track an object. This migrating pupil is significant in the following section. In addition, the reader is introduced to the properties of fibre optics that are of interest, i.e. scrambling and Focal Ratio Degradation (FRD), to the design of a Fibre Instrument Feed. After which, a history of multiple object spectroscopy is presented, and finally the HET's FIF is discussed with the problem of telecentric angle variation. This is an effect where by the chief ray of a light bundle increases its angle from the focal plane's normal as its radial position in the field increases – the HET's telecentric angle is 1.6°.

The second part presents a detailed investigation into the effects that the migrating pupil has on the fibre optic's output beam on a bench mounted pupil simulator at the Pennsylvanian State University. This rig was used to study the variations in modulation (ratio of the trough depth to the peak intensity in the fibre's output beam profile) and Full Width Half Maximum (the width of the beam at half the maximum intensity; FWHM). In one case, the modulation was found to vary from 17 – 37% and the FWHM by 3%. Such variations will cause systematic errors in precision radial velocity measurements. For these types of demanding observations, a fibre scrambler might need to be employed to increase the radial scrambling.

In the third part, a test rig to further investigate the scrambling and FRD properties of different fibres is proposed, because it is recognised that to build a successful FIF for SALT its fibres need to be well characterised. Additionally, in this part, the SALT's focal surface is discussed and corresponding fibre positioners. The SALT will have a field that is twice as large at the HET's but the telecentric angle variation, when the field is flat, increases to 4.6°. To prevent light loss, mechanisms that can move in X,Y,θ and φ are presented to align the fibre optic with the chief ray. It is shown that the telecentric angle variation can be removed optically with a doublet but adds field curvature with sag amounting to ~3mm. This would simplify the fibre positioner to motions in X,Y and Z. A design of two perpendicularly mounted linear translation stages on a parallelogram flexure mechanism is recommended.

ACKNOWLEDGEMENTS

For the many times he read the draft; for the number of times he corrected mistakes, sometimes more than once; for the hours that he gave me even at short notice; and, for this incredibly interesting topic that has lead me to want to pursue a career in astronomical instrumentation, I have to express my appreciation to my co-supervisor Dr. David Buckley at the South African Astronomical Observatory (SAAO). As he well knows, I have not been able to make words gush while writing this up and so what more can I write than: thank you.

I also want express my gratitude to my co-supervisor Mr. Brandon Reed, University of Cape Town (UCT). He taught me way back in a first year engineering class, he supervised my undergraduate thesis and he saw me through this Masters. Through all those years, he has always had abounding enthusiasm and energy for what I do; again, there is little to write that will do my thank yous justice.

I would also like to thank my supervisor, Prof. Jasson Gryzgoridis (UCT), for the NRF Grant; Dr. Larry Ramsey and Mr. Leland Engel of the Pennsylvanian State University for their assistance and support when I worked on the HET pupil simulator.

I thank Veronique Kazie-Ravat for the use of her computer and my brother, Oliver Sessions, for his mathematical assistance and probing conversations. Further, I mention the contributions from Leonie Joubert, James O'Connor, and Andy Sass. Finally, I would like to thank the staff at the SAAO, in particular Dr. Patricia Whitelock and Ethleen Lastovica.

I acknowledge the bursaries from the SAAO, the NRF and NRF travel assistance.

TABLE OF CONTENTS

Abstract	2
Acknowledgements	3
Table of Contents	4
List of Figures	6
List of Tables	9
Glossary and Acronyms	10
1. Introduction.....	12
2. Background.....	13
2.1. Introduction.....	14
2.2. The Telescope.....	15
2.2.1. Basic Concepts	15
2.2.1.1. The Celestial Coordinate System	15
2.2.1.2. Atmospheric Effects on Image	15
2.2.1.3. Magnitude System	15
2.2.1.4. Optical Concepts	16
2.2.2. General Telescope Design	16
2.2.2.1. Optical Designs.....	16
2.2.2.2. Telescope Mountings	17
2.2.3. Existing Large Telescopes (>5m) and their Observatories.....	19
2.2.4. HET's History.....	19
2.2.5. The Concept.....	20
2.2.6. HET Facts and Figures.....	21
2.2.7. Cost Savings	22
2.2.8. Interesting Technical Intricacies of the Telescope	23
2.3. Fibre Optics.....	25
2.3.1. General Introduction to Fibre Optics	25
2.3.2. Fibre Materials.....	26
2.3.3. Fibre Classes	27
2.3.4. Fibre Properties of Astronomical Consideration.....	27
2.3.5. Output Beam Pattern.....	29
2.3.5.1. Near Field Pattern:.....	29
2.3.5.2. Far Field Pattern:	29
2.4. Review of Fibre-Fed Multiple Object Spectroscopy.....	30
2.4.1. Once-Off or Fixed Positioners.....	30
2.4.1.1. Aperture Plates	30
2.4.2. Reusable Positioners	32
2.4.2.1. Multi-Fibre / Multi-Positioner (MX-Type).....	32
2.4.2.2. Multi-Fibre / Single Positioner (AUTOFIB-Type)	34
2.4.2.3. Hybrid Designs	36
2.4.2.4. Novel Designs.....	36
2.5. The Fibre Instrument Feed – The HET Example	38
2.5.1. Overview	38
2.5.2. Telecentric Angle Variation.....	40
3. The HET Pupil Simulator	42
3.1. Introduction and Objective	43
3.2. Experimental Description	43
3.2.1. Overview	43
3.2.2. Source Beam	45
3.2.3. Rig Alignment	47
3.2.4. Output	48
3.2.5. Images	49
3.2.5.1. Image Processing	49
3.2.5.2. Naming Convention for image file results	50
3.2.6. Fibre Preparation	51
3.3. General Results and Analysis	52
3.3.1. Introduction	52
3.3.2. Comprehensive Data for Set 31 (9m x 400 μ m Fibre)	52
3.3.2.1. Far Field Patterns	52
3.3.2.2. Near Field Pattern	60
3.3.3. Modulation and Width Results, Set 31 – 35	62
3.3.3.1. Set 31 - 9m 400 μ m Fibre - After Rig Re-Alignment (day 0)	62
3.3.3.2. Set 32 - 30m 600 μ m Fibre (day 1)	64
3.3.3.3. Set 33 - 9m 400 μ m Fibre - No Epoxy on Exit Face (day 14)	66

3.3.3.4	Set 34 - 30m 600 μ m fibre - Re-Polished Faces (day 14).....	68
3.3.3.5	9m 400mm fibre - no epoxy on entrance or exit face (day 16)	70
3.3.4	Discussion.....	72
3.3.4.1	400 μ m Fibres	72
3.3.4.2	600 μ m Fibres	74
3.3.5	Conclusion and Recommendations	76
3.4	Focal Ratio Degradation (FRD) Analysis.....	77
3.5	Conclusion	80
 4.		
4.1	Concept Development.....	81
4.2	Introduction.....	82
4.3	Proposed Investigation into Fibre Optics.....	82
4.4	The SALT's Telecentric Angle Problem.....	84
4.4	Concepts for the Uncorrected Focal Plane.....	85
4.4.1	Analysis of the HET's Field	85
4.4.2	Possible Manipulating Elements	90
4.4.2.1	Nanomotors®:	90
4.4.2.2	Shape Memory Alloys.....	91
4.4.2.3	Piezoelectric Benders	92
4.4.3	Concept Schemes.....	94
4.4.3.1	Concept One: Goniometric Cradles	94
4.4.3.2	Concept Two: Cross mounted translations stages mounted on a tip-tilt stage.....	95
4.5	Concepts for the Telecentric Corrected Focal Surface	96
4.5.1	Concept One: Three Axis Modules	96
4.5.2	Concept Two: Parallelogram Flexure Mechanism	97
4.6	Conclusion to Concept Development.....	99
 5.	Conclusions and Recommendations.....	100
 Appendices		101
Appendix A.	Additional Photographs	102
Appendix B.	Experimental Apparatus	104
Appendix C.	Source beam	105
Appendix D.	Colour Tests	106
Appendix E.	Code to Calculate the Intensity vs. Time Data of the Source Lamp	110
Appendix F.	Alignment Tests	111
Appendix G.	Justification on taking the Bare Field	114
Appendix H.	VisualBASIC Code for Image Reduction in EXCEL	118
Appendix I.	Program to Find the Centroid	122
Appendix J.	Comparing Centroid Results to Those Using IRAF	128
Appendix K.	Code to find the Focal Ratio Degradation	129
Appendix L.	Optimising FRD Code	130
Appendix M.	Scrambling Effects	131
Appendix N.	Breakdown for Suggested Test Rig	135
 References		137

LIST OF FIGURES

Figure 1: HET Pictures (photographs courtesy of McDonald Observatory).....	14
Figure 2: Yerkes 40-inch refractor (YERKES OBSERVATORY PHOTOGRAPH).....	17
Figure 3: Equatorial Mount (used by permission of Craig Hill).....	18
Figure 4: Schematic of Keck 1 showing the Altitude-Azimuth mount of modern telescope and the dome that encloses the telescope in a efficient manner (used by permission of WMKO).....	18
Figure 5: Dan Weedman's 1984 Model of the PSSST (courtesy McDonald Observatory, photograph by Weedman).	19
Figure 6: The 305m Arecibo Radio Telescope in Puerto Rico. Photographs: courtesy of NAIC - Arecibo Observatory, a facility of the NSF, Tony Acevedo and David Parker.....	20
Figure 7: Schematic of the HET and facility that shows the primary mirror mounted at a fixed angle and the Tracker Beam that follows the focus as an object tracks across the sky due to the rotation of the Earth (Ramsey, 1995).....	21
Figure 8: Telescope costs vs. mirror diameter (Buckley et al, 2000).	22
Figure 9: HET's Migrating Pupil (courtesy of McDonald Observatory, photograph by Sebring).....	23
Figure 10: Schematic of the HET's Spherical Aberration Corrector (SAC) in relation to the primary mirror (Ramsey, 1995).....	23
Figure 11: A general form of the Stewart-Gough Platform (Nof, 1999).....	24
Figure 12: Internal Structure of a Fibre Optic.....	25
Figure 13: Fibre Materials (Barden, 1998).....	26
Figure 14: Fibre Modes and Types (Nagel, 1993).....	27
Figure 15: Radial and Azimuthal Scrambling (Ramsey, 1988).....	28
Figure 16: Effect of Focal Ratio Degradation. Curves reveal that the fibre causes the speed of the output beam to increase, becoming more prominent at slower input beams (Ramsey, 1988).....	28
Figure 17: Location of near and far field patterns.....	29
Figure 18: MEDUSA, showing the box with the aperture plate at the top and the slit at the bottom.....	31
Figure 19: MX Spectrometer field configuration showing the "Fisherman-around-the-Pond" arrangement.....	33
Figure 20: AUTOFIB field configuration showing the fibres mounted equiangularly about the field.....	34
Figure 21: AAO, 2dF schematic (Lewis, 1998)	35
Figure 22: Prototype of SPALTSPINNE: A = Base plate, B = Ring with 36 pivot point assemblies, C = Rotary table, D = Linear table, E = Interlock tool, F = Two magnet-rod assemblies, G = Three fibre support rods protruding in the field of view of the telescope (Pitz, 1988).....	36
Figure 23: Solid Model of MEKASPEK showing the steel bands wrapped around rotating drums that position the fibre bundles in the field of view by winding and unwinding each of the drums individually	37
Figure 24: Schematic of the Prime Focus Instrument Platform showing the FIF situated on the top (Buckley & Sessions, 2000).....	38
Figure 25: A picture showing the mounted FIF on the Telescope (Buckley & Sessions, 2000).....	38
Figure 26: Field coverage of the probe (Horner, et al, 1998a,b).....	38
Figure 27: Solid Model of Actuator Layout showing three levels, two probes are actuated from the first level and the other eight are on two levels above that.	39
Figure 28: Prototype for the HET's FIF showing the elbow-like probe (indicated by the arrow) carrying the fibre optic to the focal plane.....	39
Figure 29: Telecentric variation explained. The image of star (A) on the optical axis is brought focus, the image of another star (B) is focused to the same plane but because it is off axis and the bisector of the angle is not normal to the plane, the chief ray describing the bundle of light rays from that star is inclined. This is called the telecentric angle.....	40
Figure 30: ZEMAX ray trace illustrating the telecentric angle problem for the HET.....	41
Figure 31: Telecentric angle over the field of view increasing as a function of radius from the centre ($x = 0$; $y = 0$)	41
Figure 32: Schematic – Pupil Simulator. Note the central obstruction, the moving pupil mask and the test rig to record the near and far field patterns.....	44
Figure 33: Two limits in mask positions. The left image corresponds to on-axis (0°) and the right to the maximum off-axis position (6°).	44
Figure 34: Source assembly.....	45
Figure 35: Lamp Intensity vs. Time. Note the initial peak.....	46
Figure 36: Central assembly.....	47
Figure 37: Setup to record far field (bare field) pattern.....	48
Figure 38: Setup to record near field pattern.....	48
Figure 39: Using IRAF to obtain values of modulation and FWHM.....	49
Figure 40: Machine drawing of ferrule (dimensions in mm).....	51
Figure 41: pss0m0n31.jpg.....	53
Figure 42: bfs0m0n31.jpg.....	53
Figure 43: pss0m0n31cross-section (Section A-A).....	53
Figure 44: bfs0m0n31cross-section (Section B-B).....	53
Figure 45: pss0m1n31.jpg.....	54
Figure 46: bfs0m1n31.jpg.....	54
Figure 47: pss0m1n31cross-section.....	54
Figure 48: bfs0m1n31cross-section.....	54
Figure 49:pss0m2n31.jpg.....	55
Figure 50: bfs0m2n31.jpg.....	55
Figure 51: pss0m2n31cross-section.....	55
Figure 52: bfs0m2n31cross-section.....	55
Figure 53: pss0m3n31.jpg.....	56
Figure 54: bfs0m3n31.jpg.....	56
Figure 55: pss0m3n31cross-section.....	56
Figure 56: bfs0m3n31cross-section.....	56
Figure 57: pss0m4n31.jpg.....	57
Figure 58: bfs0m4n31.jpg.....	57
Figure 59: pss0m4n31cross-section.....	57
Figure 60:bfs0m4n31 cross-section.....	57

Figure 61: pss0m5n31.jpg.....	58
Figure 62: bfs0m5n31.jpg.....	58
Figure 63: pss0m5n31cross-section.....	58
Figure 64: bfs0m5n31cross-section.....	58
Figure 65: pss0m6n31.jpg.....	59
Figure 66: bfs0m6n31.jpg.....	59
Figure 67: pss0m6n31cross-section.....	59
Figure 68: bfs0m6n31cross-section.....	59
Figure 69: nfs0m0n31.jpg.....	60
Figure 70: nfs0m3n31.jpg.....	60
Figure 71: nfs0m6n31.jpg.....	60
Figure 72: Set 31 Near field cross-section.....	61
Figure 73: Set 31 Near field cross-section normalised.....	61
Figure 74: Set 31 overplot of cross-sections.....	62
Figure 75: Set 31 modulation curve.....	63
Figure 76: Set 31 full width curves.....	63
Figure 77: Set 32 overplot of cross-sections.....	64
Figure 78: Set 32 modulation curve.....	64
Figure 79: Set 32 full width curves.....	65
Figure 80: Set 33 overplot of cross-sections.....	66
Figure 81: Set 33 modulation curve.....	66
Figure 82: Set 33 full width curves.....	67
Figure 83: Set 34 overplot of cross-sections.....	68
Figure 84: Set 34 modulation curve.....	68
Figure 85: Set 34 full width curves.....	69
Figure 86: Set 35 overplot of cross-sections.....	70
Figure 87: Set 35 modulation curve.....	70
Figure 88: Set 35 full width curves.....	71
Figure 89: Modulation curves – Set 31, 33, 35.....	72
Figure 90: Trough value curves – Set 31, 33, 35.....	73
Figure 91: FWHM curves – Set 31, 33, 35.....	73
Figure 92: FW13.5 curves – Set 31, 33, 35.....	74
Figure 93: Modulation curves – Set 32, 34.....	74
Figure 94: Trough value curves – Set 32, 34.....	75
Figure 95: FWHM curves – Set 32, 34.....	75
Figure 96: FW13.5 curves – Set 32, 34.....	76
Figure 97: Set 31 (400 μ m x 9m) enclosed counts vs. radius from centroid.....	77
Figure 98: Set 31 (400 μ m x 9m) FRD test results.....	78
Figure 99: Set 34 (600 μ m x 30m) enclosed counts vs. radius from centroid.....	79
Figure 100: Set 34 (600 μ m x 30m) FRD Results.....	79
Figure 101: Proposed FRD test rig.....	82
Figure 102: ZEMAX ray-trace (courtesy of D. O'Donoghue) showing the telecentric angle variation in the SALT's uncorrected field of view (Buckley & Sessions, 2000).....	84
Figure 103: ZEMAX ray-trace (courtesy of D. O'Donoghue) showing the telecentric angle variation removed in the SALT's corrected field of view with a doublet (Buckley & Sessions, 2000).....	84
Figure 104: Type 0 MOS probes. The XY plane (units in inches) represents the area that the probe covers in the focal plane (Figure 26), X is the longer axis, which extends beyond the centre of the field. The Y axis only represents half the mapped out area (because of symmetry). The vertical axis represents the fractional loss of light, which increases as the probe moves outside its zoned limit.....	85
Figure 105: Similar to Figure 104, for Type 1 MOS probes. Showing light loss in the central regions by the probes.....	86
Figure 106: Coordinate system defined to verify angle on Type 1 probes.....	86
Figure 107: Line of analysis shown by bold line starting at a radius of 30% on the Y Axis to the full radius of 100% along the hypotenuse of the area mapped out by the linear translation stages.....	87
Figure 108: Probe optimised to 1 degree.....	87
Figure 109: Plot of $\arccos(\frac{\hat{L}}{\hat{P}})$ – Case 1.....	89
Figure 110: Plot of $\arccos(\frac{\hat{L}}{\hat{P}})$ – Case 2.....	89
Figure 111: Plot of $\arccos(\frac{\hat{L}}{\hat{P}})$ – Case 3.....	89
Figure 112: Nanomotor® linear table.....	90
Figure 113: Nanomotor® arrangement into a triplet to provide tip and tilt of the probe.....	91
Figure 114: Scheme to manipulate fibres using "muscle wire".....	92
Figure 115: Piezoelectric bender.....	92
Figure 116: Force diagram for uniformly loaded beam. W = Total Load, Z = Section modulus of cross-section.....	93
Figure 117: Tilting force required to bend fibre.....	94
Figure 118: Goniometric cradle.....	94
Figure 119: Tip Tilt Scheme.....	95
Figure 120: Three axis manipulator.....	96
Figure 121: Layout for three axis manipulator.....	97
Figure 122: Parallellogram mechanism.....	97
Figure 123: Layout for parallellogram mechanism.....	98
Figure 124: Bench mounted pupil simulator. At the far end, the first mirror is seen which collimates the light onto the second mirror (lower right). This focuses the light via the pellicle beamsplitter into the test fibre. The inspection optics are seen to the right of the central assembly.....	102
Figure 125: Fibre magnified on monitor. The light spot to the left of the indicated fibre is the focused beam from the simulator.....	102

Figure 126: Backlighting test fibre with a laser. This fills the fibre with low order modes that can be used to position (tip/tilt) the input (or other end) of this fibre. Alignment is ensured when the laser spot is focused on the output of the source fibre after the reflections on the second and first mirrors.....	103
Figure 127: Original far field imaging with opal sheet.....	103
Figure 128: Source beam taken with digital camera.....	105
Figure 129: Source beam cross-section.....	105
Figure 130: Red filter (10 second exposure).....	107
Figure 131: Yellow filter (10 second exposure).....	107
Figure 132: Green filter (90 second exposure).....	107
Figure 133: Blue/Green filter (60 second exposure).....	107
Figure 134: Blue filter (180 second exposure).....	108
Figure 135: White - no filter (7 second exposure).....	108
Figure 136: Plot of Modulation vs. Colour.....	108
Figure 137: Filter Colour vs. FWHM & FW 13.5.....	109
Figure 138: 0.00 degrees.....	111
Figure 139: 0.25 degrees.....	111
Figure 140: 0.50 degrees.....	111
Figure 141: 0.75 degrees.....	111
Figure 142: 1.00 degrees.....	111
Figure 143: 1.25 degrees.....	111
Figure 144: 1.50 degrees.....	112
Figure 145: 1.75 degrees.....	112
Figure 146: 2.00 degrees.....	112
Figure 147: Plot of Modulation vs. Tilt Angle.....	113
Figure 148: Plot of Pixel Value of FWHM & FW13.5 vs. Tilt Angle.....	113
Figure 149: I0 Cross-section – d = 2.8mm.....	114
Figure 150: I1 Cross-section – d = 5.3mm.....	114
Figure 151: I2 Cross-section – d = 7.8mm.....	115
Figure 152: I3 Cross-section – d = 10.3mm.....	115
Figure 153: I4 Cross-section – d = 12.8mm.....	115
Figure 154: I5 Cross-section – d = 15.3mm.....	115
Figure 155: I6 Cross- section – d = 17.8mm.....	115
Figure 156: I7 Cross-section – d = 20.3mm.....	115
Figure 157: I8 Cross-section – d = 22.8mm.....	115
Figure 158: I9 Cross-section – d = 25.3mm.....	115
Figure 159: I10 Cross-section – d = 27.8mm.....	116
Figure 160: I11 Cross-section – d = 30.3mm.....	116
Figure 161: I12 Cross-section – d = 32.8mm.....	116
Figure 162: FWHM and modulation vs. camera position.....	117
Figure 163: The image used in this appendix -bfs0m0n32.jpg.....	122
Figure 164: Plot of average line pixel values vs. line number for method 1.....	124
Figure 165: Plot of average line pixel values vs. line number for method 2.....	125
Figure 166: Plot of beam width vs. line number for method 3.....	126
Figure 167: Excerpt from manual for method 4.....	127
Figure 168: Input beam to fibre.....	131
Figure 169: Plot of the input and output profiles to and from the fibre.....	132
Figure 170: Overplot of the two curves with their centroids coinciding about 1000 on the X-Axis.....	133
Figure 171: Scaled flux levels, where the areas under both curves are now equal. The scale factor in this case, k = 13.....	133

LIST OF TABLES

Table 1: Existing Large Telescopes (>5m), their Observatories and Location.....	19
Table 2: HET Facts and Figures.....	21
Table 3: Table of data sets.....	52
Table 4: Distance between fibre and chip related to code used.....	114
Table 5: Method 1 & 2 results compared to IRAF, the brackets are percentages of the IRAF result.....	128
Table 6: Full widths.....	131
Table 7: Table of Apparatus, Notes and Descriptions	135
Table 8: Table of apparatus, costs	135

University of Cape Town

GLOSSARY AND ACRONYMS

AAO	Anglo-Australian Observatory.
AAT	The 3.9m Anglo-Australian Telescope at Siding Spring near Coonabarabran, Australia.
Aperture Stop	The diameter of a lens or mirror that allows a bundle of unobstructed rays to pass.
Astigmatism	Aberration of a lens where the horizontal and vertical lines have different focal points.
CCD	Charge Couple Device.
Celestial Sphere	The projection of the sky onto an imaginary sphere that can then be described by spherical coordinates.
Chief Ray	The ray that passes through the centre of the aperture stop in an optical system.
Critical Angle	There is a critical angle, θ_c , under which a ray at an interface of two media will propagate along the interface. Consider Snell's Law, $n_i \sin \theta_i = n_t \sin \theta_t$, with $\theta_t = 90^\circ$, then
	$\theta_c = \theta_i = \arcsin \left(\frac{n_t}{n_i} \right)$
Declination	A coordinate on the celestial sphere equivalent to earth's latitude.
Exitance	Flux leaving a surface per unit area.
FIF	Fibre Instrument Feed.
Fisherman-around-the-Pond	A Style of Multi-Fibre / Multi Positioner MOS where the probes are individually controlled by actuators distributed about the focal surface. Each probe accesses a proportion of the total area.
f/Ratio	or f/# or f/Number, Ratio of the focal length of an optical system to the diameter of the aperture i.e. $f/\# = f/d$
	Note: When d is large compared to f , the $f/\#$ is small. This beam is referred to as "fast" dating to the early photographic days because photographs taken with faster $f/\#$ required shorter exposure times, conversely "narrow" beams where d is small compared to f , are termed "slow". Consequently the $f/\#$ of a beam may be referred to in terms of "speed".
Focal Ratio Degradation	or FRD, the effect whereby the speed of the input beam becomes faster upon emergence from the fibre optic. It is a result of rays scattering as they undergo reflection at the core/cladding interface.
FW13.5	Full Width at $1/e^2$ or 13.5% maximum intensity.
FWHM	Full Width Half Maximum (i.e. 50% maximum intensity).
HET	Hobby-Eberly Telescope. The progenitor of the Southern African Large Telescope sited at McDonald Observatory in West Texas.
IRAF	Image Reduction and Analysis Facility, a data reduction package.
Irradiance	Amount of energy incident on a surface per unit time per unit area.
LRS	The Low Resolution Spectrograph mounted on the tracker at the HET.
Magnitude	The scale used by astronomers to measure the intensity of an object in the sky

	$(m \propto -2.5\log_{10}(\text{intensity}))$.
MOS	Multiple Object Spectroscopy.
n	Index of refraction of a material, which is the ratio of the speed of an electromagnetic wave in a vacuum ($c = 2.998 \times 10^8 \text{ m/s}$) to the speed in that material. $(n_{\text{air}} \approx 1.0003, n_{\text{water}} \approx 1.333, n_{\text{diamond}} \approx 2.419)$
PFIP	Prime Focus Instrument Platform on the HET.
Pupil	An image of the aperture stop in an optical system. The first pupil in an optical system is called an entrance pupil and the last pupil is referred to as the exit pupil. It is useful in describing whether a ray will pass through an optical system or not.
Right Ascension	A coordinate on the celestial sphere equivalent to earth's longitude.
SAC	Spherical Aberration Corrector.
SALT	Southern African Large Telescope.
Snell's Law	Law of refraction, $n_i \sin \theta_i = n_t \sin \theta_t$, where n is the index of refraction (refer n), θ is the angle the ray makes with the normal to the interface, the subscripts i refer to the incident ray and t to the transmitted ray.
Spherical Aberration	The effect where rays at different distances from the optical axis of a spherical element are brought to a different focal point which cause a zone of confusion.
TIR	Total Internal Reflection.
Total Internal Reflection	Occurs once an incident ray exceeds the critical angle for an optical interface as described by Snell's Law.
UKST	United Kingdom Schmidt Telescope sited at Siding Spring Observatory.
UV	Ultraviolet light ($1\text{nm} < \lambda < \sim 300\text{nm}$).
VB	VisualBASIC
Zenith	The point on the celestial sphere that is directly above the observer.
ZEMAX	Optical Design Program by Focus Software, Inc.

1. INTRODUCTION

When one looks through the eyepiece of a telescope many celestial objects are seen – each a massive structure of radiating gas and dust. Some are stars in various stages of evolution – blue hot infants or cooler red giants, grandfather white dwarfs; binary systems with mass transfer; violent supernovae, globular clusters; satellite galaxies; spiral and elliptical galaxies or even on a much larger scale: clusters of galaxies. These all have a different light signature: each whispering the secret of its nature, and any of these objects in the field of view of the telescope are observable. To study these objects, astronomers have a number of tools at their disposal; perhaps the most common is the spectrograph that disperses the object's light into its component wavelengths or colours, called a spectrum. Except to increase the resolution of its spectrum, a slit needs be placed over the object of interest. That literally throws away the other objects! Imagine if there was a way to simultaneously take the spectra of a number of these objects and increase observing efficiency by many times.

Fibre optics have the ability to guide light and can be used to arrange the random pattern of objects in the field of view and reconfigure it into the entrance slit of a spectrograph. We now have a means of simultaneously taking many spectra. Such an instrument is called the Fibre Instrument Feed or FIF on the HET.

South Africa is building the largest optical telescope in the southern hemisphere, it is called the Southern African Large Telescope (SALT) and is based on the design of a telescope in West Texas called the Hobby-Eberly Telescope (HET). These deviate from classical telescopes by not having a steerable parabolic primary mirror as in the classical design but a fixed-altitude spherical mirror. It means that the focus and the entrance pupil migrate across the primary reflector as an object is tracked across the sky. This lends itself to fibre fed spectroscopy because it is desirable to minimise the tracking mass to increase the positioning and pointing accuracy of the telescope. By not having the astronomical spectrograph up at the focus point, the scrambling properties of the fibres can then be used to remove some of the memory of the changing input due to the migrating pupil. It also means that the spectrograph can be placed on an optical bench in an environmentally controlled room. Because there is no changing gravitational component on the instrument (it is not riding the telescope), cheaper mounting techniques can be employed and because flexure is no longer a consideration, more money can be spent on improved optics. Other advantages are that humidity and temperature can be held constant and that the instrument can be mounted in an evacuated chamber. In the SALT/HET design the spectrograph is located in a basement beneath the telescope for these reasons.

In the second section, a general background is presented. This includes an introduction to the HET; fibre optics; a short history of multi-object spectroscopy and some examples of instruments. The section ends with the examination of the HET's FIF.

The third section is an examination into the effects that the migrating pupil has on the output of fibres, carried out at the Pennsylvania State University. This investigation underlines the importance of careful selection of fibres for the instrument and in particular the characterisation of the fibres.

The fourth section proposes a test rig to characterise the properties of fibre optics used in the design of a Fibre Instrument Feed and develops the concept for such an instrument for SALT.

2. BACKGROUND

University Of Cape Town

2.1 INTRODUCTION

When completed in 2004, the Southern African Large Telescope (SALT) will be the largest optical telescope in the southern hemisphere – a 10 metre-class telescope. It will have approximately 25 times the collecting area of the largest telescope presently in South Africa: the 1.9m Radcliffe reflector at Sutherland, the South African Astronomical Observatory's field station in the Karoo, Northern Cape. SALT is based on the Hobby-Eberly Telescope (HET; see Figure 1) at the University of Texas at Austin's McDonald Observatory in West Texas (Buckley, 2000; Buckley, et al, 2000; Stobie, et al, 2000).

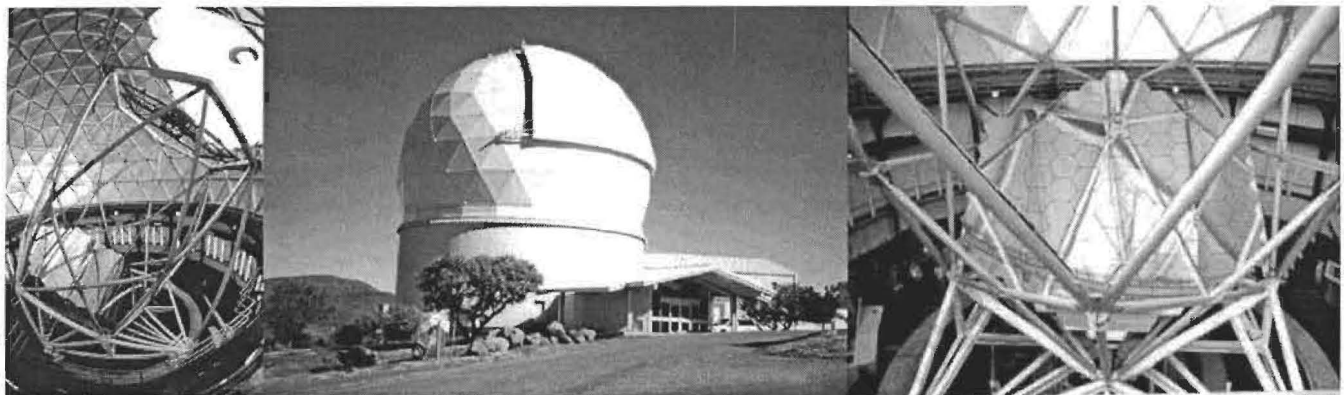


Figure 1: HET Pictures (photographs courtesy of McDonald Observatory).

SALT will be built by an international collaboration of partners including (Stobie, et al, 2000; SALT Web site¹):

- The National Research Foundation of South Africa.
- Nicolaus Copernicus Astronomical Centre of the Polish Academy of Sciences.
- The Hobby-Eberly Telescope Board.
- Rutgers, the State University of New Jersey.
- Georg-August-Universität Göttingen.
- The University of Wisconsin-Madison.
- Carnegie Mellon University.
- The University of Canterbury, New Zealand.
- A consortium of United Kingdom universities and institutions.

The Hobby-Eberly Telescope Board is a consortium of universities: University of Texas at Austin, Pennsylvania State University, Ludwig-Maximilians-Universität München, Georg-August-Universität Göttingen and Stanford University. They are providing the designs, expertise, and possibly some hardware and software (Ramsey, et al, 1998).

On 1st June 1998, the South African Department of Arts, Culture, Science and Technology (DACST) committed itself to funding 50% of the capital construction cost over 5 years; it backed this project as its “flagship” for Science and Technology. However, conditions outlined in the SALT Collateral Benefits Plan (Stobie, et al, 1999) are attached to this support. This plan essentially states that, wherever possible, spending must be maximised within South Africa, technology transfer must be accomplished, and additional educational benefits be realised.

On the 25th November 1999, Dr Ben Ngubane, Minister of DACST gave the approval for the construction of SALT (Stobie, et al, 2000) and the groundbreaking occurred on 1st September 2000.

In this section, attention is paid to the novel design of the telescope and how it is suited to fibre optics. This is followed by a discussion of fibres themselves and the history of multiple object spectroscopy, including examples of instruments that use fibre optic technology. The section ends with an examination of the instrument that positions fibres in the field of view of the HET, the Fibre Instrument Feed (FIF).

¹ www.salt.ac.za/team/index.html

2.2 THE TELESCOPE

SALT will be the southern hemisphere's "sister" of the HET, which acquired its first spectra in 1997 (Ramsey, et al, 1998). The SALT and HET are a first in a new concept of telescope design of large aperture, fixed altitude, segmented spherical primary mirror.

2.2.1 Basic Concepts

2.2.1.1 *The Celestial Coordinate System*

The celestial sphere is an imagined sphere of infinite radius centred on the observer with all astronomical objects projected onto this sphere. Positions of objects can thus be described by two orthogonal angles. The two coordinate systems used are the equatorial system and altitude and azimuth system (Ridpath, 1997).

2.2.1.1.1 *The Equatorial System*

The equatorial system uses right ascension (RA or α) and declination (Dec or δ). If the terrestrial coordinate system is projected onto the celestial sphere then α corresponds to longitude and δ corresponds to latitude. It follows that the angular distance between the zenith, i.e. the point directly overhead the observer, and the celestial pole, i.e. the projection of the Earth's rotation axis onto the celestial sphere, is the co-latitude of the observer. α is measured eastwards from the "First Point of Aries" (corresponding to the Sun's position at the Autumn Equinox [near March 20]) and expressed in hours, minutes and seconds, while δ is measured positive from the celestial equator for northern declinations, negative for the southern declinations, and is expressed in degrees, arc-minutes and arc-seconds.

2.2.1.1.2 *The Altitude & Azimuth System*

The Altitude & Azimuth System can be imagined as a projection of the Earth's latitude and longitude onto the *celestial sphere* which has been rotated so that the equator corresponds to the observer's horizon. The position of the celestial object can then be described in terms of degrees both along the horizon from the Northern point, called azimuth, and the elevation of the object, called altitude.

2.2.1.1.3 *Atmospheric Effects on Image*

The Earth's atmosphere causes two main effects on starlight: changes in irradiance and in direction. Changes in irradiance can be attributed to extinction (or absorption) and scintillation, the latter due to moving pockets of air acting as lenses that increase and decrease the intensity of a star, causing it to twinkle. The light changes direction due to refraction (through an increasing mass as the pressure rises) and *seeing*. Seeing is caused by the light passing through atmospheric cells of different densities and hence refractive index that are constantly moving with a frequency ~10 to 100Hz. The result of seeing is a moving blurred disc of the objects in the focal plane. Seeing is measured by quoting the *Full Width Half Maximum (FWHM)* of the energy distribution, or the radius of the circle that encloses 50 or 80% of the energy of the beam (either EE50 or EE80).

2.2.1.1.4 *Magnitude System*

A system to classify the brightness of stars adopted from the ancient Greeks who named the brightest stars first magnitude and the faintest they could see sixth magnitude. All visible stars could be placed on this scale. Thus, counter intuitively, a larger magnitude corresponds to a fainter source. In modern times, luminosity has been correlated to the magnitude system with a logarithmic function.

2.2.1.4 Optical Concepts

2.2.1.4.1 Beam Speed

Beam speed is the characterisation of the angular size of a converging beam. The term comes from photography where the setting on the camera that has a large angular measurement exposes quickly and is thus called a “fast beam”, conversely, one that is small, and “pencil” like, exposes in a longer period of time and is called a “slow beam”. The focal ratio (*f/ratio*) or focal number (*f/number*, *f/#*) is the measure of that beam speed and is expressed:

$$f\# = \frac{f}{d}$$

where *f* is the focal length and *d* is the *aperture*. It can be seen that the smaller the aperture for a given focal length, the larger the *f/#* is, thus a larger *f/#* corresponds to a slower beam.

2.2.1.4.2 Plate Scale

Plate scale is the ratio of the angular distance between two objects on the sky to the linear distance in the focal surface (Parker, 1997). It is often expressed in arc-seconds per millimetre, or for *CCD* detectors, arc-seconds per pixel. A fast beam, with a greater beam angle, thus has a larger plate-scale than a slower beam for the same linear dimension at the image surface.

2.2.2 General Telescope Design

2.2.2.1 Optical Designs

A telescope may use either refracting (lenses) or reflecting (mirrors) elements in its design. A telescope will be named after the element it uses. One that uses both refracting and reflecting elements is called a catadioptric telescope.

2.2.2.1.1 Refracting Telescopes

Hans Lippershy is credited for the invention of the refracting telescope in 1608. However, Galileo was the first person to turn the invention to the sky a year later. He used a twenty-magnification telescope in his discovery of the Galilean moons about Jupiter and the “imperfections” (craters) on the Moon. He also saw the phases of Venus and Sun spots. These discoveries revolutionised the way man thought about the Universe in which he dwelled because they confirmed that the Universe was not perfect as predicted by the religious beliefs at the time.

A refracting telescope uses lenses, typically made of glass, to focus the light. The power of the lens is determined by the index of refraction of the material. The index of refraction is wavelength dependent, which means that different wavelengths passing through a lens have different focal lengths. When white light, or light composed of many wavelengths, is focused there is no unique focus. This is termed chromatic aberration and can be corrected by bonding different types of glass with differing refractive index together to form a compound lens.

Refracting telescopes are limited in size by the diameter of the lens. The glass begins to severely distort under its own weight beyond a certain diameter, at approximately a metre. Figure 2 shows the largest refractor in the world - the Yerkes 40-inch (1m) refractor, which was built in 1897, and is located at the University of Chicago’s Yerkes Observatory² in Wisconsin.

² (<http://astro.uchicago.edu/yerkes/>)



Figure 2: Yerkes 40-inch refractor (Yerkes Observatory Photograph).

2.2.2.1.2 Reflecting Telescopes

A coated mirror is used as the optical element in a reflecting telescope. The coating, usually aluminium, silver or gold (depending on the desired spectral response), is applied to the first surface and is often unprotected. Reflecting telescopes have the advantage over refracting telescopes in that the mirror can be supported evenly from behind enabling the largest single mirrors today up to ~8m in diameter (Subaru, Gemini, VLT). Even bigger mirror apertures can be realised by segmenting smaller mirrors into a much larger array. Examples include Keck I & II (with 36 mirrors) and the HET (with 91 mirrors). Reflecting telescopes do not suffer from chromatic aberrations.

Examples of reflecting telescopes include the Newtonian, Cassegrain and Gregorian designs. Newton placed a parabolic mirror at the bottom of the telescope tube and a secondary flat mirror in the beam at the top to fold the focus through 90 degrees. Cassegrain put a convex secondary mirror before the prime focus that directs the light to a focus back through a hole in the primary. The Gregorian telescope is similar to the Cassegrain except the convex secondary mirror is placed beyond the prime focus.

2.2.2.1.3 Catadioptric Telescopes

A good example of the catadioptric telescope is the Schmidt Telescope (or Camera) which has a spherical primary (which is free from *astigmatism*) and a thin correcting aspheric lens in the front to remove the spherical aberration. Schmidt telescopes are used in wide field survey work.

2.2.2.2 Telescope Mountings

2.2.2.2.1 Equatorial Mount

Early astronomical telescopes were mounted equatorially, because of the simplicity in tracking an object across the sky during the course of a night. An amateur telescope mounted in such a way is shown in Figure 3. This arrangement of axes align the telescope in space such that only one axis needs to be controlled to keep an object in view, accounting for the Earth's rotation. The telescope is pointed by setting it in declination (Dec) and in Right Ascension (RA). When the RA or Polar Axis points directly at the celestial pole, i.e. it is aligned with the Earth's rotation axis, the Earth's rotation is effectively removed by driving about this axis at the same rate of rotation (i.e. 1 rotation in $23^{\text{h}}56^{\text{m}}$).

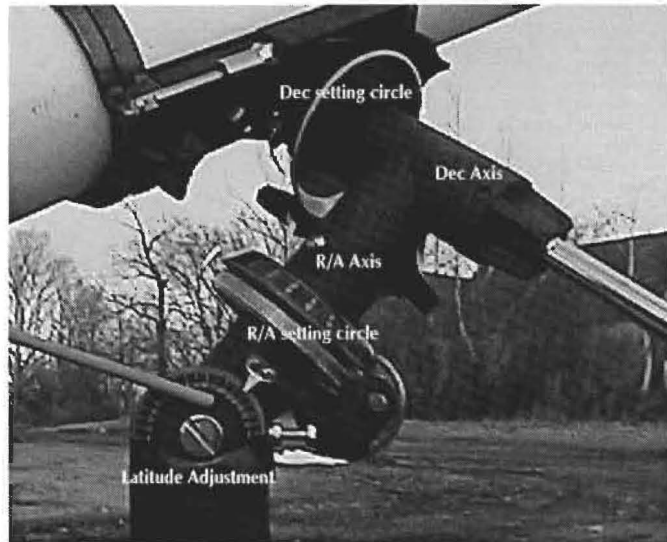


Figure 3: Equatorial Mount (used by permission of Craig Hill).

2.2.2.2.2 Altitude-Azimuth Mount

Equatorial mounts require a dome that is large enough for the telescope to point in all directions. Another mounting technique – the Altitude-Azimuth (ALT-AZ) mount – can lead to a far smaller dome (and thus decreased cost). The mount cradles the primary mirror, tipping it in altitude and rotating it about in azimuth (see the schematic of Keck I & II in Figure 4). The instrument is required to be rotated along the arc of the track to stop the images smearing (field rotation). This mount, which can enclose the telescope with minimal space wastage, requires a far more sophisticated control of these three degrees of freedom. Proliferation of the computer industry was required to realise this.

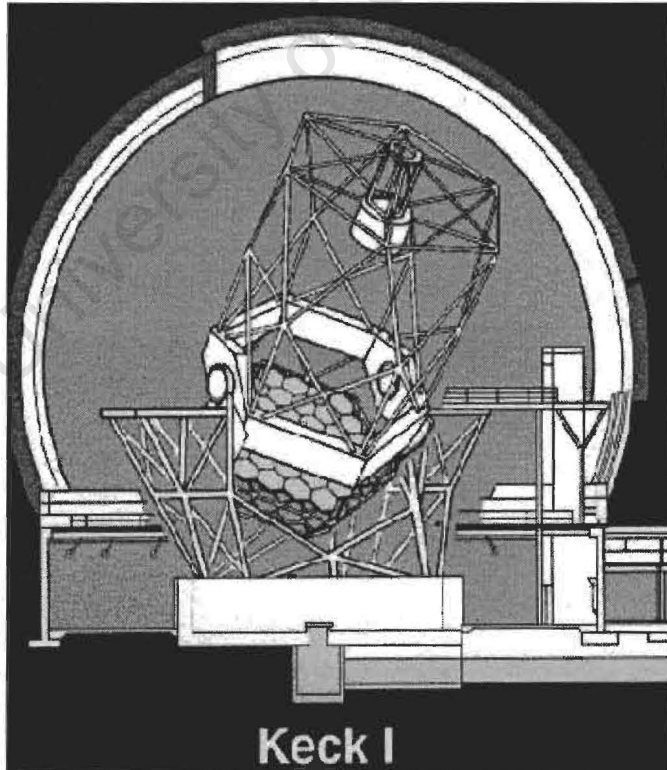


Figure 4: Schematic of Keck 1 showing the Altitude-Azimuth mount of modern telescope and the dome that encloses the telescope in an efficient manner (used by permission of WMKO).

2.2.3 Existing Large Telescopes (>5m) and their Observatories

Telescope Name	Aperture	Observatory	Location
Keck I & II	10m	W.M. Keck Observatory	Mauna Kea, Hawaii
HET	9.2m	McDonald Observatory	Mount Fowlks, Texas
Subaru	8.3m	NAOJ*	Mauna Kea, Hawaii
VLT	4x8.2m	European Southern Observatory	Cerro Paranal, Chile
Gemini North	8m	Gemini Observatory	Mauna Kea, Hawaii
Gemini South	8m	Gemini Observatory	Cerro Pachón, Chile
MMT	6.5m	MMT Observatory	Mount Hopkins, Arizona
BTA (Big Alt-azimuth Telescope)	6m	Special Astrophysical Observatory	Karachaevo-Cherkesia, Russia
Hale	5m	Palomar	Palomar Mountain, California

Table 1: Existing Large Telescopes (>5m), their Observatories and Location.

* National Astronomical Observatory of Japan

2.2.4 HET's History

In 1983, Dan Weedman, a Pennsylvanian State University (Penn State) professor, returned from a conference at Cornell thinking about an optical counterpart to their Arecibo Radio Telescope (refer §2.2.5). Although Pierre Connes built a 4.2m telescope made up of 36 spherical mirrors, 600mm square, at the Observatory of Meudon in the 1970s (Mertz, 1996), Weedman's concept was for a much larger telescope with fixed elevation. He approached Larry Ramsey (Penn State) and together they developed the concept for a cheap 8m-class telescope that would be available to the Penn State astronomical community. Initially the idea was to keep it very simple with only 10 circular mirrors, three metres in diameter. This telescope would be specially optimised for fibre-fed spectroscopic survey work and was named the Penn State Spectroscopic Survey Telescope (PSSST). Funding issues eventually led to the involvement of other universities. A consortium was formed with the University of Texas at Austin (52%), Pennsylvanian State University (31%), Stanford University (7%), Ludwig-Maximilians-Universität München (5%) and Georg-August-Universität Göttingen (5%). The involvement of these institutions and other benefactors enabled the designs to be developed into a first class telescope, the Hobby-Eberly Telescope (Barna, 1998).

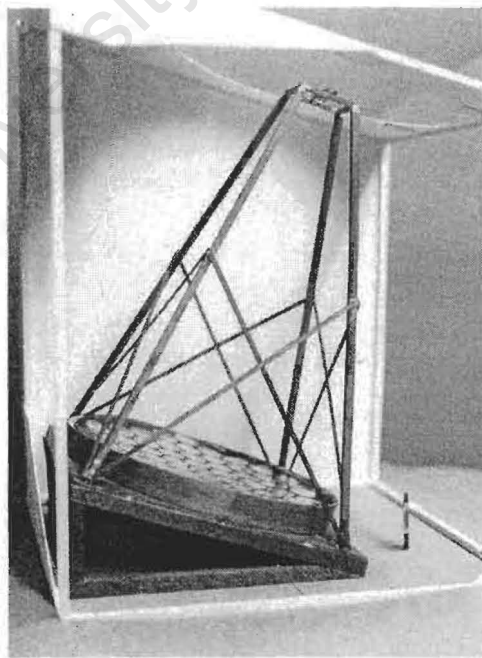


Figure 5: Dan Weedman's 1984 Model of the PSSST (courtesy McDonald Observatory, photograph by Weedman).

2.2.5 The Concept

The Weedman/Ramsey concept, now the SALT/HET telescope design, is the optical counterpart to the Arecibo Radio Telescope. This telescope has its 305m spherical dish mounted in a Puerto Rican karst sinkhole and points directly upwards, waiting for objects to transverse its line of sight (see Figure 6). Inside a suspended dome are the secondary and tertiary reflecting surfaces that focus the radio waves into feed horn detectors. The dome is mounted on an arched azimuth arm that can point the detector to within 20° of the vertical (Krisciunas, 1988). This telescope has featured in films such as *Golden Eye* (Pierce Brosnan as James Bond) and *Contact* (Jodie Foster).

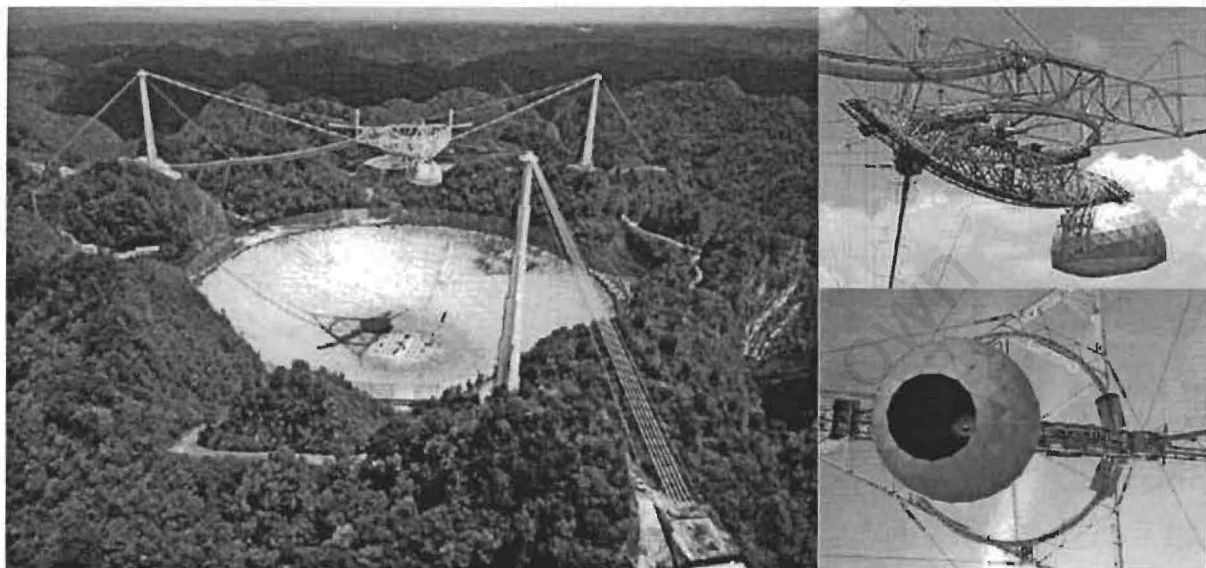


Figure 6: The 305m Arecibo Radio Telescope in Puerto Rico. Photographs: courtesy of NAIC - Arecibo Observatory, a facility of the NSF, Tony Acevedo and David Parker.

Like the radio telescope, the SALT/HET has a spherical reflecting surface and has means of tracking the focus equivalent to the suspended dome with a Tracker Beam assembly. It also has to wait for objects to transverse its line of sight. However, unlike the radio telescope, the optical counterpart has its reflecting surface, or mirror, mounted at some fixed angle from the vertical (e.g. 35°) and has the capability to rotate to any azimuthal position which considerably increases the availability of observable objects. A schematic of the telescope and facility can be seen in Figure 7.

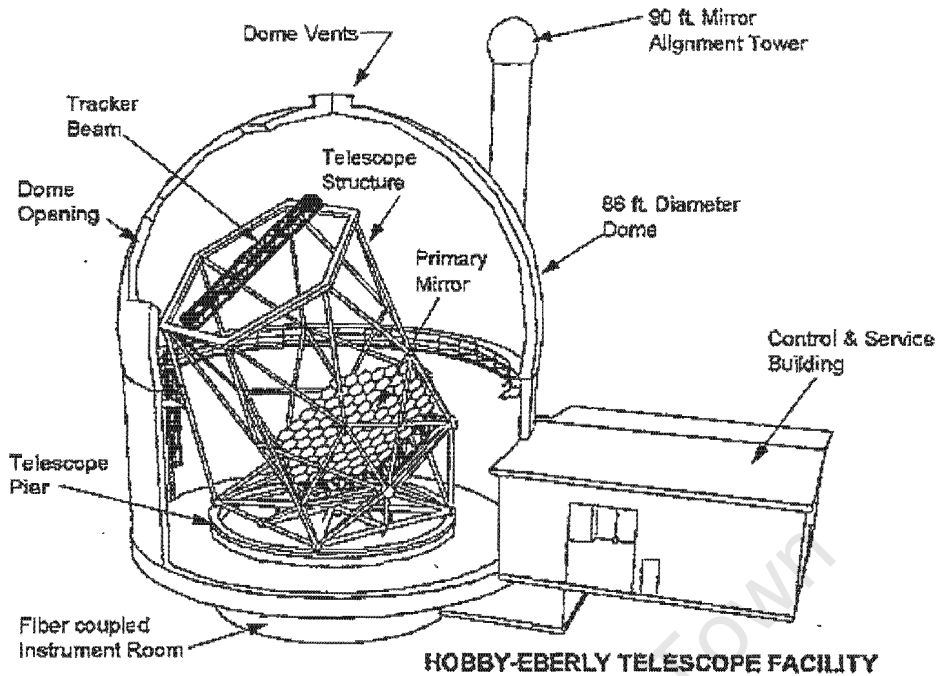


Figure 7: Schematic of the HET and facility that shows the primary mirror mounted at a fixed angle and the Tracker Beam that follows the focus as an object tracks across the sky due to the rotation of the Earth (Ramsey, 1995).

2.2.6 HET Facts and Figures

Structure	
Structure Mass	82 tons
Tilt Angle	35° from vertical
Number Air Bearings	8
Allowable Rotation	540°
Primary Mirror	
Circumscribed Mirror Diameter	11m
Reflecting Area	77.6m ²
Primary Array	91 Segments, Close Pack Configuration
Segment Mirror	1m Across Flats, t = 50mm, m = 114kg
Radius of Curvature	26.165m
Focal Length	13.083m
Number of Actuators to Control Mirror Array	273
Tracker and SAC	
Positioning Accuracy	10μm
Number of Corrector Elements	4
Entrance Pupil Diameter on Primary Mirror	9.2m
f/Ratio at image plane	f/4.7
Field of view	4 arc-minutes, 50mm
Plate Scale	204.5μm/arc-seconds

Table 2: HET Facts and Figures.

Cost ~US \$15m (Ramsey, et al, 1998)

2.2.7 Cost Savings

The SALT/HET telescope design can be built for approximately a fifth of the cost of a conventional telescope of the same size (e.g. Keck I & II, Gemini telescopes, see Figure 8), however some compromises in performance must be made. The telescope can only access ~70% of the sky, over the course of a year.

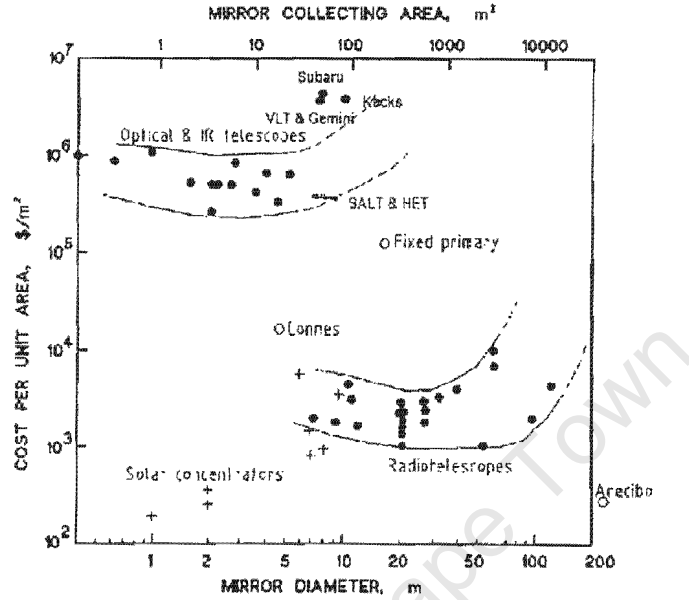


Figure 8: Telescope costs vs. mirror diameter (Buckley et al, 2000).

The consequence of this novel design is that SALT/HET can only observe objects that pass through an annular observing "window" 12° wide and offset at an angle from the zenith. The rotating fixed altitude mirror simplifies the structure, since the gravitational force vector does not alter during a track of an object. Because the sky rotates about the Earth's polar axis (whose altitude corresponds to the latitude of the site), this arrangement enables ~70% of the sky to be accessed at some time, with track times ranging from ~45 minutes to ~3 hours, depending on the object's declination. For that reason, observations are executed on a "queue schedule" calculated to view objects precisely as they pass through the window. Over the course of a year, with an even distribution of objects over the observable sky, a telescope operating in this manner will have a similar efficiency of an all-purpose Altitude-Azimuth or Equatorial Mount Telescope (see §2.2.2.2).

The telescope makes further cost savings by having a segmented primary mirror of 91 hexagonal segments in the close pack configuration with a spherical radius ~26m corresponding to a ~13m focal length. The spherical nature of the telescope means that the focus lies on a "focal sphere" and not at a point, so tracking involves the following of this focus on the sphere rather than moving the entire mirror, consequently the pupil tracks across the primary mirror changing in size and shape (Figure 9). A corrector (the SAC, Figure 10), required to mainly correct spherical aberration, is mounted together with instrumentation on a gantry-type structure called the Tracker Beam. This moves the payload (i.e. the SAC, prime focus instrument, acquisition, guiding and imaging facilities and a fibre positioner) to track celestial objects as they move across the sky.

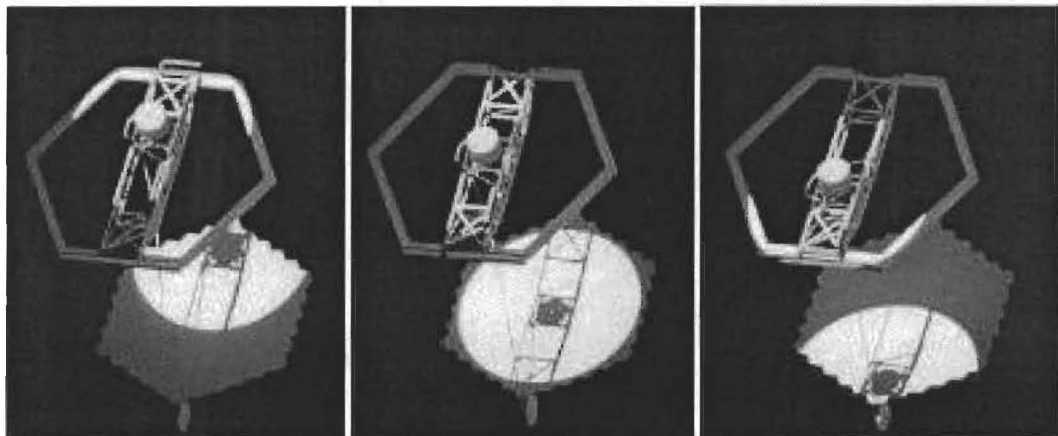


Figure 9: HET's Migrating Pupil (courtesy of McDonald Observatory, photograph by Sebring).

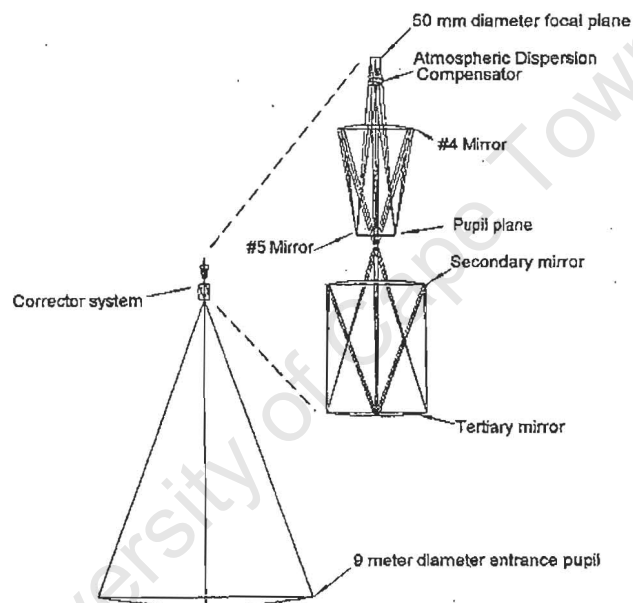


Figure 10: Schematic of the HET's Spherical Aberration Corrector (SAC) in relation to the primary mirror (Ramsey, 1995).

A redesign of the SAC for the SALT has given a field of view that is twice the size of the HET's. Where the HET has a focal plane 4 arc-minutes or 50mm in diameter, the SALT has a focal surface 8 arc-minutes and 100mm in diameter (O'Donoghue, 2000).

2.2.8 Interesting Technical Intricacies of the Telescope

There is very little new technology used in the design of this telescope. All the parts are off-the-shelf encoders, motors and bearings. It is the manner in which these parts are assembled that leads to a totally novel and interesting design that is extremely clever in its approach to breaking the cost per area curve (Figure 8).

To track an object across the sky, the Tracker has to keep the instrument package on the focal sphere, that is a fixed distance from the mirror and normal to the mirror, at all times. The problem is how to set up a mechanical assembly which can operate in a spherical coordinate system. To simplify, to a first order approximation, the image will track along a curve projected onto an X-Y plane at the top of the telescope, this is followed using a gantry structure with the bridge (called the Y-Beam) moving in

the X-direction and a Carriage that moves in Y. The instrument package also needs to have Z motion to follow the shape of the sphere and, in addition, the package needs to be rolled and pitched to keep its axis orientated normal to the primary mirror. These last two requirements are elegantly accomplished using a 6-3 Stewart-Gough Platform or hexapod that is mounted onto the Carriage.

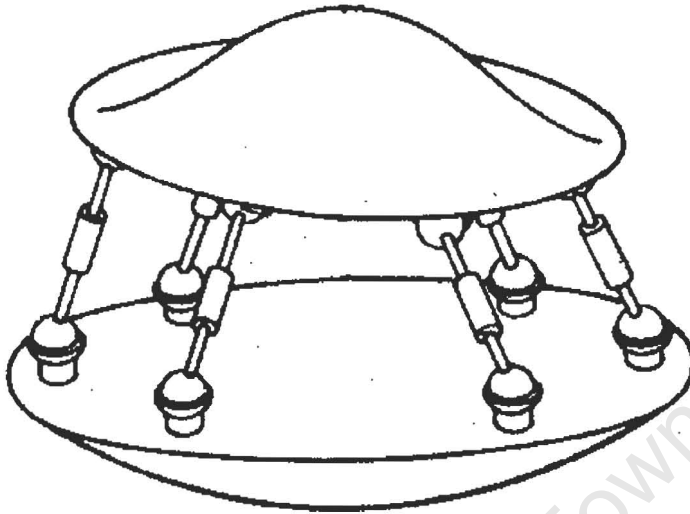


Figure 11: A general form of the Stewart-Gough Platform (Nof, 1999).

A hexapod, as its name suggests, has six “legs” mounted between two rigid bodies, e.g. a base plate and an adjustable ring (see Figure 11). The formal name: “Stewart-Gough Platform” is prefixed with a numerical designation where the first number refers to the number of contact points on the base and the second, the number of mounting points to the adjustable ring. Such a mechanism is an example of a parallel manipulator. Each “leg” is a prismatic joint (1 degree of linear freedom) connected at its ends by spherical joints (two degrees of revolute freedom) to the rigid bodies. Such a parallel manipulator can position a large payload accurately, however, its workspace is considerably smaller than a serial manipulator (e.g. multiarm robot). In other words each leg can telescope independently to orientate the adjustable ring uniquely with six degrees of freedom. A hexapod can thus position a payload in X, Y and Z, and about those axis, θ , ϕ and ρ (Nof, 1999).

It is important for the image quality of the telescope that all the mirror segments bring the light from a celestial object to the same focus position. This is not a trivial task since all the mirrors are mounted on a three level space frame, or truss, constructed with thin walled steel tubes and solid nodes (Booth, et al, 2000). The mirrors have a very small coefficient of thermal expansion compared to the truss. When there is a change in temperature the mirror array opening up like unfolding petals of a flower in the morning. Initially it was thought that it would be possible to model the thermal dynamics of the truss using finite element methods. Because this has proven to be extremely difficult, a segment alignment and management system has had to be installed to control the three actuators behind every mirror segment in tip, tilt and piston to hold the “global” radius of curvature of the primary mirror array as the truss warps with thermal effects. There are 12 inductive sensors mounted to each mirror, two on each flat of the hexagon, relative motions to the central mirror of the array are transformed into the mirror actuators motions to fix the mirror and hold the focus. At the time of writing, the HET is in the process of installing the system, SALT on the other hand will install the edge sensors at time of construction.

The azimuthal rotation of the structure is achieved with air bearings. Eight bearings, resembling hovercraft skirts, lift the four support feet of the 82 ton structure about 25mm off the pier. Two drive motors on the front two feet can rotate the entire structure with extreme ease.

2.3 FIBRE OPTICS

At a meeting of The Royal Institution in 1854, John Tyndall demonstrated the “lightpipe” where light shone into a bucket followed the stream of water issuing out of its side (Einarsson, 1996). This demonstration of Total Internal Reflection (TIR) would lead to the development of fibre optics nearly a century later. Alexander Graham Bell developed the photophone in 1880 (four years after the telephone) that used the sun’s light reflected to a receiver, demonstrating that communications with light was indeed possible (Bell, 1880).

Fibre optic technology was developed by the communications industry in the 1960s because it has the capability to convey vast amounts of data between two locations. Information transmitted is proportional to the frequency of the carrying wave. For light the frequency is in the range of $\sim 10^{14} - 10^{15}$ Hz ($3000\text{nm} > \lambda > 300\text{nm}$) compared to $\sim 10^6 - 10^{10}$ Hz ($300\text{m} > \lambda > 0.03\text{m}$) for radio and microwaves (Nagel, 1993). Fibre optics provide an excellent and efficient means to transmit light over considerable, and often indirect, distances.

Fibres are used in astronomical instrumentation because they are capable of relaying reformatted light from the focus of the telescope to another instrument that may be located off the telescope. Such an instrument would be easier to mount since flexure is not an issue, further the instrument may be kept in an environmentally controlled (temperature, humidity and vibration) room.

2.3.1 General Introduction to Fibre Optics

Fibre optics are light waveguides comprising of an inner core of fused silica, about the diameter of a human hair ($\sim 50\mu\text{m}$), that guides the light along its length by *TIR*. This core is enclosed within a cladding made of material with a smaller index of refraction (ratio of the speed of light in a vacuum to the speed in that material) that reduces the loss of light occurring, due to imperfections such as grease or scratches, at the core’s surface. The core and cladding are usually protected by buffers and jacketing (see schematic in Figure 12). Many such fibres can then be bound together to form cables that contain hundreds or thousands of fibres.

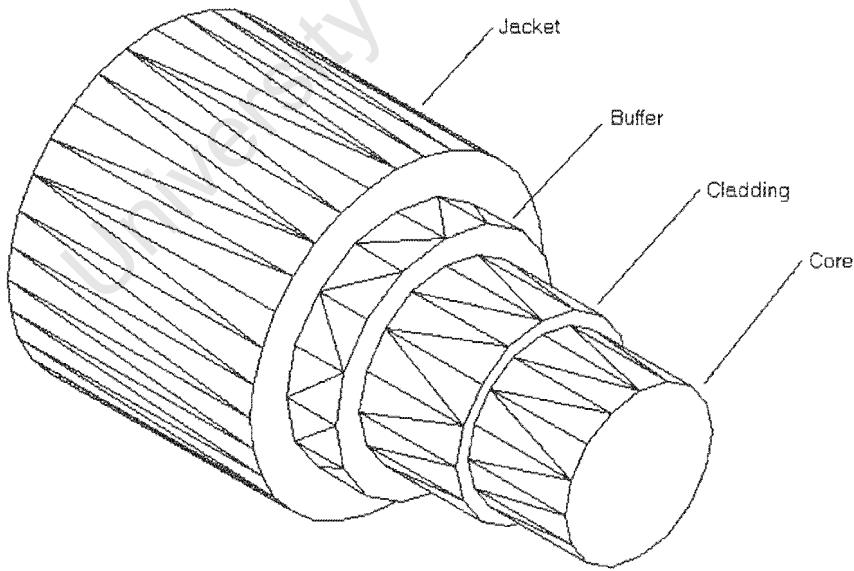


Figure 12: Internal Structure of a Fibre Optic.

A mode is the name given to a transmitted wave front or an electromagnetic field distribution that satisfies Maxwell's equations and the boundary conditions for a particular waveguide geometry (Nelson, 1988; Cherin, 1983). Low order modes are

propagated along the fibre at low angles of incidence on the fibre face and higher order modes propagate nearer the critical angle for *TIR*. The term “lossy” refers to those modes that exceed the critical angle of the fibre and thus loose energy into the cladding. It has been found that when the cladding thickness is ~10 times the longest wavelength of light desired to be transmitted, the amount of lossy modes can be reduced (Lu, et al, 1998; Ramsey, 1998). Modes may also be “bumped” into different orders by the geometry of a bent fibre, imperfections at the core/cladding interface or by defects in the fibre material, this is technically referred to as mode coupling (Keck, 1976).

2.3.2 Fibre Materials

There are three main types of fibres: “wet”, “dry” and “hydrogen-doped dry” fibres. Wet fibres are fused silica with high quantities of hydroxyl (OH^-) impurities. The silicon oxides provide good transmission in the blue, but the OH^- has absorption bands in the red - often referred to as the “water peak”. Unfortunately, when the OH^- is removed from the material (dry fibres) to gain good transmission in the red, the heat of the drawing process breaks the silicon oxide (SiO) bonds. It is the presence of OH^- ions that enable the SiO bonds to anneal while the fibre cools. Dry fibres are thus poor blue transmitters (Figure 13). The dry fibre can be doped with hydrogen to give better transmission at both ends of the spectrum (Barden, 1995). Fibres filled with tetrachloroethylene and carbon tetrachloride have been considered to achieve better transmission (Stone, 1971).

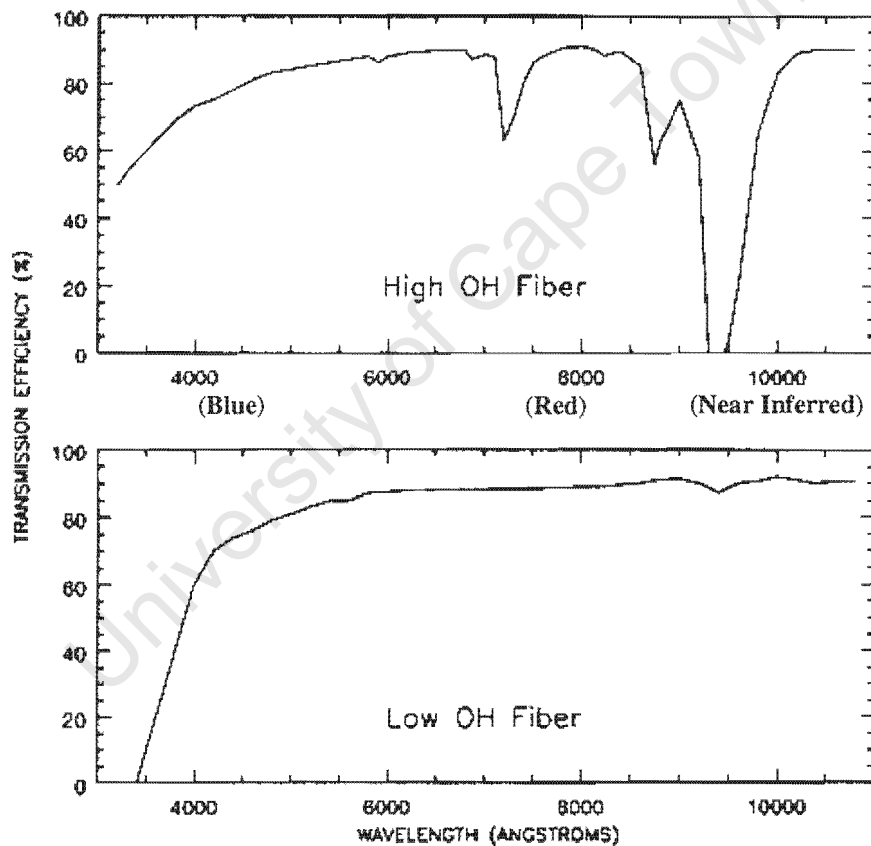


Figure 13: Fibre Materials (Barden, 1998).

-Monday

Accession details

July 9,2001

Order type D Order no. 31147 Fund code 7
Account code 4508 Cont code Location UT Subject mrc
Author SESSIONS, NICHOLAS JAMES ADAM UT 60 SESS
Title INVESTIGATION INTO THE FIBRE INSTRUMENT FEED FOR THE SOUTHERN AFRICAN LARGE TELESCOPE (SALT)
Publisher M.Sc. (MECHANICAL ENGINEERING) Publ. date FEB 2001
ISBN number Format Edition
Quantity ordered 1 Qty invoiced to date 1
Vendor code 7 Qty acc. to date 1
Vendor instr1
Vendor Instr2
Accession number 7729 Accession date 09/07/2001
Order number 31147
Donation/Exchg no. Donor ENGINEERING AND THE BUILT

Receive Back Delete Edit Forward Quit

2.3.3 Fibre Classes

Fibre cores are available in step- and graded-index multi-mode and single-mode fibres (see Figure 14). Here index refers to the refractive index of the material. Step-index multi-mode fibres result in the dispersion of an input signal because the information transmitted at the higher order modes travels further and thus takes longer than the lower order modes. This can be solved by varying, or grading, the index of refraction of the core in a parabolic profile. Practically this is achieved with a number of layers of gradually decreasing refractive index material, thus resulting in a near parabolic function in a stepwise manner. The light travelling furthest travels in a medium of decreasing refractive index and thus speeds up and reduces the dispersion effect. The third class of fibre is the single mode; it allows one mode to be transmitted down its axis and is often used for interferometry purposes because pathlength can be controlled by the length of the fibre (Parry, 1998).

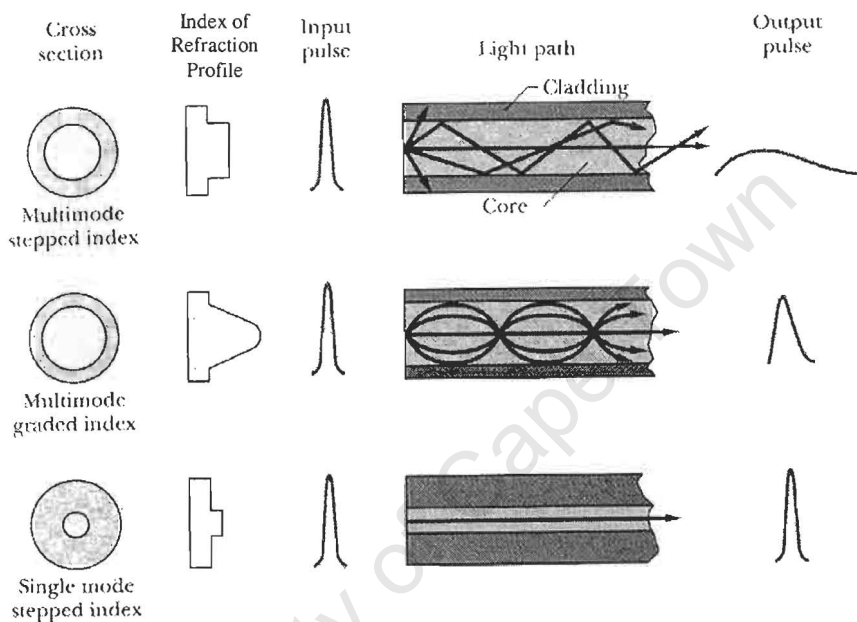


Figure 14: Fibre Modes and Types (Nagel, 1993).

Multi-mode, graded-index, and single mode fibres are used in communications where signal dispersion is kept to a minimum.

Multi-mode, step-index fibres are the most commonly used fibres in astronomical applications because they tend to have greater spectral coverage and are made in a larger range of core diameters (Nelson, 1988).

2.3.4 Fibre Properties of Astronomical Consideration

The idea that modes can be “bumped” results in a number of properties that are important to consider in the design of astronomical instruments. The three main properties are:

1. Azimuthal scrambling.
2. Radial scrambling.
3. Focal Radio Degradation (FRD).

(1) Azimuthal scrambling can be displayed by injecting a laser (essentially a single mode) at an angle into the fibre (Figure 15). The emerging beam, if projected onto a screen, would appear to be ring shaped with axial symmetry. It is noted that azimuthal scrambling is always complete, even for short lengths of fibre (Heacox, 1986; Heacox, 1988; Barden, 1995). This makes geometric sense if light is simplified to a number of single “rays”. Rays that are not on axis will enter the fibre and be

propagated as skew rays in a helical manner down the length of the fibre, when slightly different pathlengths are followed due to imperfections it will result in this projected ring.

(2) Radial scrambling – the ring displayed in the description given above will have a certain width. This represents the radial scrambling in the fibre. Due to radial scrambling the output has little “memory” of the input beam – information is smeared radially. It is this property that enables high precision radial velocity measurements to be made of stars and other celestial objects because undesirable movements in the telescope (i.e. due to tracking) are smoothed out on the output face of the fibre (Hill, 1980). It is obvious that radial scrambling is enhanced by an increase in fibre length because of the greater number of bumps that a mode encounters.

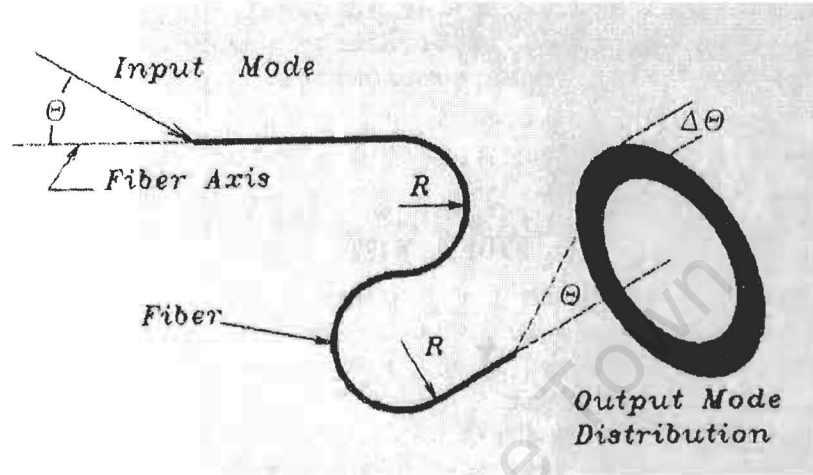


Figure 15: Radial and Azimuthal Scrambling (Ramsey, 1988).

(3) If a square profile beam were injected into a fibre then, due to mode bumping, the emerging beam would become more gaussian and faster. This property, where the *f*/ratio of the output beam is faster than the input beam, is called Focal Ratio Degradation (FRD). It is pronounced at slower *f*/ratios and is clearly seen in Figure 16. Due to FRD the spectrograph optics must be made larger in order to retain the same resolution were fibre optics not involved, this implies a greater cost for the instrument.

Both Radial Scrambling and FRD are pronounced at slower *f*/ratios where there is a large fraction of modes that are propagated at very shallow angles. It is in this case that there is a greater chance for mode coupling to occur. As stated before, radial scrambling is desirable, whereas FRD is not, and since both are consequences of the same phenomenon, a compromise in the input *f*/ratio must be made. Ramsey (1988) suggests that the best input *f*/ratio is approximately *f*/4.

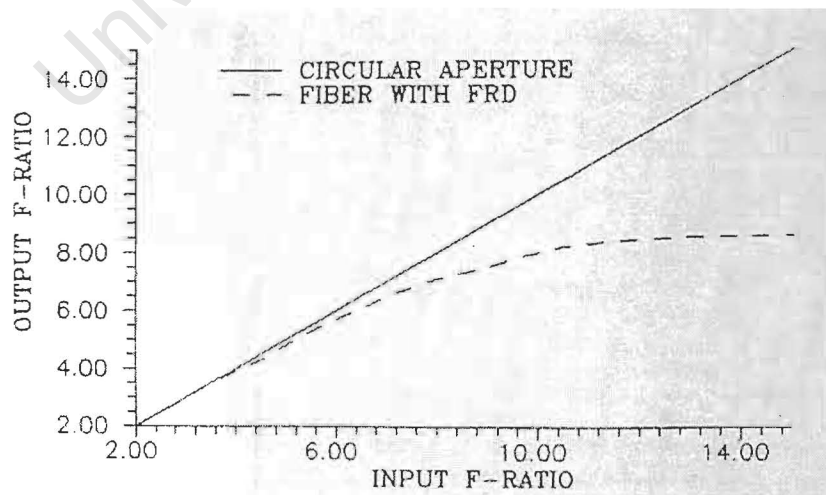


Figure 16: Effect of Focal Ratio Degradation. Curves reveal that the fibre causes the speed of the output beam to increase, becoming more prominent at slower input beams (Ramsey, 1988).

2.3.5 Output Beam Pattern

The output beam can be characterised in two ways by taking a plane at two points perpendicular to the fibre axis, one at the fibre exit face and the other at some arbitrary distance. The nomenclature is taken from the communications industry:

2.3.5.1 Near Field Pattern:

The near field pattern is a plane cut perpendicular to the optical axis at the point of the fibre exit and represents the angular distribution of the light exiting the fibre. It may also be described as the “exitance with respect to position in the plane of the fibre end face” (Weik, 1989). Because the fibre fed spectrograph images the fibre optic face directly onto the detector, any variation in this pattern results in changes in pixel illumination and contributes to radial-velocity errors (Hunter & Ramsey, 1992).

2.3.5.2 Far Field Pattern:

The far field pattern is described as the radiation pattern in the region where the optical power per unit area is largely independent of the distance from the source. The pattern is a “function of the angle of radiation from the end face of the fibre” (Weik, 1989). Variations in the far field are collimated and projected onto the dispersing element and because these elements are not perfect, different aberration effects will occur with the varying illumination.

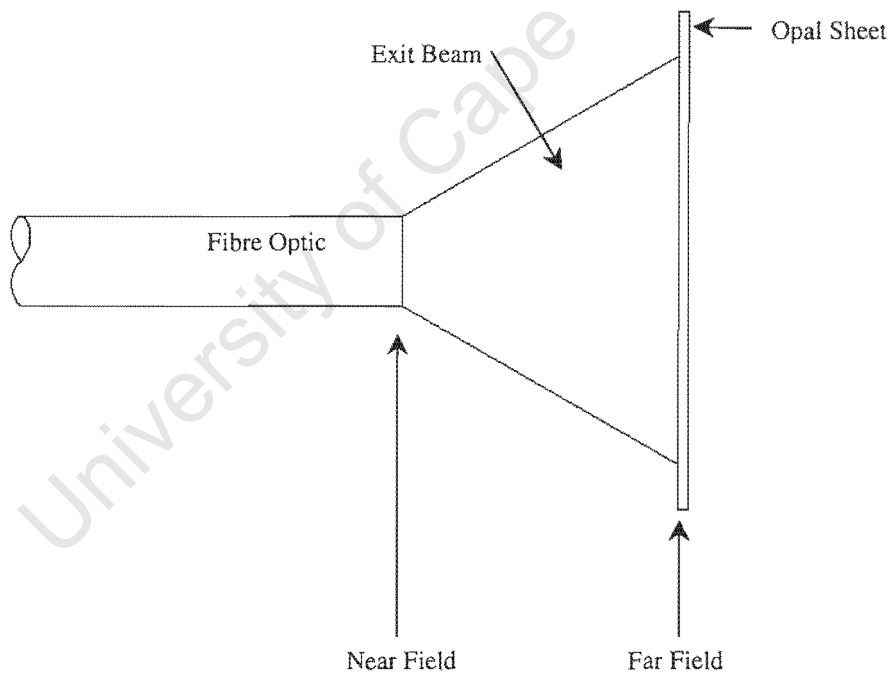


Figure 17: Location of near and far field patterns.

2.4 REVIEW OF FIBRE-FED MULTIPLE OBJECT SPECTROSCOPY

The design of instruments for multi-object spectroscopy arose from the need to efficiently analyse large numbers of stars or galaxies in a given field of view. Low resolution spectra could be obtained using objective prisms placed over the aperture of the telescope or by slitless spectroscopy. However, problems are introduced by the overlapping spectra in a dense field and when the object is faint compared to the background sky (Hoag, 1976). Fibre optics, when they became commercially available, offered a solution since they could easily pipe the randomised pattern of light and reformat it into the slit of a spectrograph.

Fibre-fed multiple-object spectroscopy originated in the late 1970s, first appearing in the form of “aperture plates” with fixed geometry. Examples are given in §2.4.1.1. It soon became clear that robotic control for fibre positioning was a better solution, given the labour required constructing the aperture plates for a once-off observation. The next generation of multiple-object fibre-positioners was of robotic design (see §2.4.2). Two main types evolved. On the one hand, there are MX-type positioners and the other are the AUTOFIB-type (Gray, 1988; Barden, 1993; Buruch, et al, 1988).

2.4.1 Once-Off or Fixed Positioners

The history of multiple object spectroscopy begins with fixed geometry aperture plates to position the fibres that feed the light from the telescope to the spectrometer. The disadvantage is that these can only be used for once-off observations, unless the same field is observed later.

2.4.1.1 Aperture Plates

Aperture plates are typically metal or glass and are placed at the focal surface of a telescope. Fibre optics are then attached in some way to the plate so that light from a desired object is injected into the fibre and emerges in an organised way at the spectrograph.

Examples of instruments using aperture plates include:

2.4.1.1.1 MEDUSA

MEDUSA was built at the University of Arizona’s Steward Observatory because they were interested in the dynamical properties of galaxies, in x-ray sources, clusters and the “missing mass” problem (where unobservable mass is required to hold galaxies and clusters together given the measured rotation speeds) (Hill, 1982). They adapted an existing Boller and Chivens spectrograph for the 2.3m (90-inch) Cassegrain telescope by removing the slit assembly and replacing it with a 220mm spacer that increased the distance between the focal plane and the entrance slit. A box could then be inserted into the space, that has the aperture plate on the top and the slit on the bottom connected by short fibres (see Figure 18). The boxes could be pre-made and slid into the spectrograph throughout the night, reducing the reconfiguration time between exposures.

The aperture plate was made of aluminium, 210mm x 210mm x 3mm and drilled with 711 μm diameter holes, positioned to $\pm 20\mu\text{m}$ accuracy. Inserted through these holes were step-indexed fibres of 300 μm core diameter, that were epoxied in place. The slit of the spectrograph accommodated 44 fibres, allowing 37 objects to be observed with seven fibres connected to a helium-argon comparison lamp (to calibrate the science spectra). Guiding was accomplished using four single fibres that direct light from reference stars in the field to photomultiplier tubes mounted on the side.

In December 1979, the first spectra were obtained (Hill, 1988), two years later the instrument was achieving ~ 100 spectra of magnitude V~17.5³ on a clear night (Hill, 1982).

³ The filter used to measure the magnitude of a star in yellow-green light (the centre of the wavelength spectrum that the eye is sensitive to).

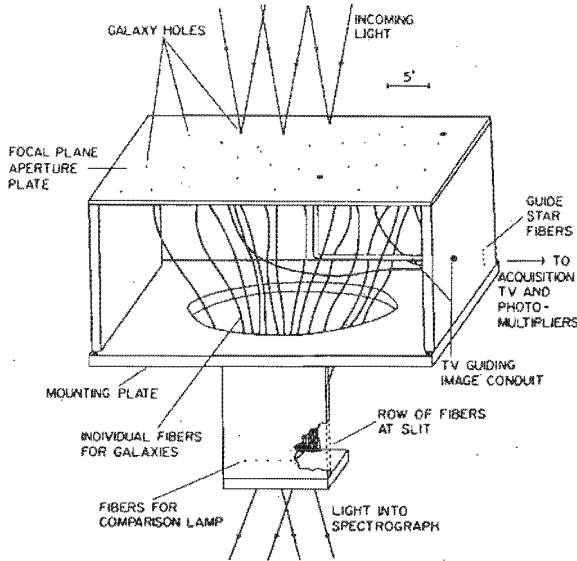


Figure 18: MEDUSA, showing the box with the aperture plate at the top and the slit at the bottom.

2.4.1.1.2 FOCAP

Fibre Optic Coupled Aperture Plate (*FOCAP*), an instrument at the Anglo-Australian Observatory (AAO) which had an approximate 50 object capability, was used on the 3.9m Anglo-Australian Telescope (AAT) in the early 1980s. It used brass aperture plates 380mm in diameter and 1.6mm thick that were drilled with holes corresponding to galaxy positions. Fibres mounted in ferrules (hollow metal protective cylinders), protecting the fibre ends and ensuring accurate alignment, were then plugged into the holes in the aperture plates. These were then mounted in photographic plate holders and deformed to the approximate focal surface by a central tensioning screw. The degree of deformation of the plate was a compromise between the focal surface and alignment of the fibres with the telescope pupil. These fibres were then bundled and led to either the RGO (Royal Greenwich Observatory) or FORS (Faint Object Red Spectrograph) spectrographs where they were lined up to form the entrance slit (Gray, 1986).

2.4.1.1.3 FLAIR I, PANACHE, FLAIR II & AUTOFRED

Multi-Object Spectroscopy began on the UK Schmidt Telescope (UKST), which has a fast focal ratio of $f/2.48$ and thus a large field of view: $6.6^\circ \times 6.6^\circ$ or over 40 degrees square, in 1985 with an instrument called the Fibre-Linked Array-Image Reformatter (*FLAIR*). It was in regular operation by 1987 and in 1988 it was upgraded to *PANACHE* (PANoramic Area Coverage with High Efficiency). In 1989, work began on a semi-automated *FLAIR II* and *AUTOFRED* that was finished in January 1992 (Watson, et al, 1993).

The first multiobject fibre spectrometer was built with 40 channels (40 fibres of core diameter $40\mu\text{m}$, 10m long). In 1986, it was reported that there were only 39 fibres – one “fell victim to ... inexperience ...” (Watson, 1986). The instrument was designed to have low impact on normal operation of the telescope, meaning that it could be used interchangeably with photographic plates. The method used aperture plates: a positive copy of UKST photographic plate, which held the fibres. A skeletal mandrel behind the aperture plate deformed the 1mm thick glass to the spherical focal surface and enabled the fibres, which were cemented to the glass, to extrude from the rear through the ribs.

Set up of the aperture plate began by first balancing the positive photographic plate, unstressed, on the mandrel. The fibres were placed in stainless-steel tubes, forming a ferrule, which enabled better bonding to the glass by increasing the effective diameter of the fibre to $\sim 5\text{mm}$. The ferrules, with the fibres backlit, were manipulated in X,Y,Z with a fibre chuck underneath the plate. A microscope was used to examine the alignment of the backlit fibre and the position indicated by the photographic plate from the top. UV light, used to cure the epoxy on the rear surface of the glass where the ferrule was attached to the plate, was shone from the front of the glass inline with the microscope using a beam splitter.

The telescope has a fast focal ratio, which means the plate scale is large (see §2.2.1.4.2): 67.14 arc-seconds/mm. Since the conditions of the site result in seeing from 1 to 2.5 arc-seconds, a small core diameter fibre optic had to be used – 50 μ m, corresponding to 3.35 arc-seconds on the sky.

FLAIR was built as a pilot system with cheap components, to prove a concept. It was built for under £10,000. Cost savings were realised in mounting the optics (including photographic lenses) on an optical bench on the dome floor. It is noted that transmission optics are preferred in fibre fed spectrographs since the central obstruction of the telescope is not perfectly preserved in the output of the fibre (Watson, 1986).

In 1998 improvements were made to the system, called *PANACHE*. A new feed bundle with 35 fibres of ϕ 100 μ m core with 90° microprisms, enabled placement (also cemented) on the front of the apertures plate (with the fibres parallel to the plate). It was found that the glass plate had up to 30% light loss (called “*FLAIR* loss”) due to the transmission through the emulsion layer and cement. In the new arrangement the positions of the fibres were not as restricted as in *FLAIR* where the skeleton of a mandrel was found to obstruct ~50% of the potential fibre positions. The new minimum separation between objects was also reduced to ~2mm. The fibres were also changed to PolyMicro-FH which display better blue transmission (Watson, 1988).

The next upgrade, called *FLAIR II*, used robotic positioning, new plateholders with retracting fibres and a new spectrograph. Plateholders had to be identical in size to the photographic plateholders so that it could be accepted by the telescope as if it were a photographic plate, thus not interfering with the normal operation of the telescope.

The robotic positioning was in the form of *AUTOFRED* (Bedding, et al, 1993). Fibres had to be manually placed in the jaws of AutoFred, which under computer control (and the identification of the target on a monitor) would position it on the backing plate. This semi-automation nearly doubled the rate of setting up the fibres, but was still a time consuming process.

In *PANACHE* all the fibres entered the plateholder in one position and after the ferrules had been cemented in position, the excess lengths were taped up, increased the chance of breakage. *FLAIR II* had retractable fibres that would reduce the amount of fibre lying on the front of the plate. Fibres would loop in their own storage chamber so that only what was required for placement would be extracted. The fibres were not self-retracting but had to be pushed back after use (Watson, et al, 1993).

FLAIR II used a new spectrograph, designed by Peter Gray and dubbed *FISCH* (Fibre-SCHmidt). It has a *f*/2 collimator to accept the degraded beam from the *f*/2.48 injected into the fibres (Parker & Watson, 1995).

2.4.1.1.4 OPTOPUS

OPTOPUS was a multi-object spectrograph mounted to the European Southern Observatory (ESO) 3.6m Cassegrain focus in 1985. It used 54 fibres terminated in ferrules with microlenses (to convert the Cassegrain *f*/8 to *f*/3, a focal ratio more suitable to inject into fibres) that plugged into drilled holes in a plugboard. The fibres fed a Boller and Chivens spectrograph with a modified collimator. After tests in the laboratory, it was decided that the focal ratio changing microlenses could be removed from the ferrules for OPTOPUS2 (improvements for OPTOPUS2 mainly concerned the spectrograph; Avila & D’Odorico, 1993).

2.4.2 Reusable Positioners

2.4.2.1 Multi-Fibre / Multi-Positioner (MX-Type)

The MX-Spectrograph is an instrument built at the University of Arizona’s Steward Observatory in 1985 and is the archetype of the first type of robotic positioning of fibres. The MX has 32 fibres in a “Fisherman-around-the-Pond” configuration, meaning the fibres are mounted to probes that protrude into the field and whose positioning mechanisms are spaced equiangularly about the focal surface. Each probe is controlled individually giving the advantage of performing real time manipulation of its individual fibres during operation and minimising the time for fibre reconfiguration.

2.4.2.1.1 MX-Spectrometer

This instrument was designed at the Steward Observatory to improve the efficiency of the MEDUSA (§2.4.1.1.1) multi-object spectrograph. It was clear that the fibres needed to be mechanised in order to increase the efficiency, aperture plates were extremely labour intensive. The MX-Spectrometer was mounted on the 2.3m (90-inch) Cassegrain telescope and coupled to an adapted Boller and Chivens spectrometer, built for long slit spectroscopy. This meant that fibres with an average length of 30cm coupled the focal plane to the spectrograph. The slit allowed 66 fibres to be lined up, 60 fibres led to focused objects, and six to a helium-argon comparison lamp. The instrument consisted of 32 modules each having two or more fibres mounted on the end of a probe that protruded (~100mm) into the focal plane. These modules were mounted in a “Fisherman-around-the-Pond” arrangement, allowing the mechanical and electrical components to remain unobtrusive outside the field (see Figure 19).

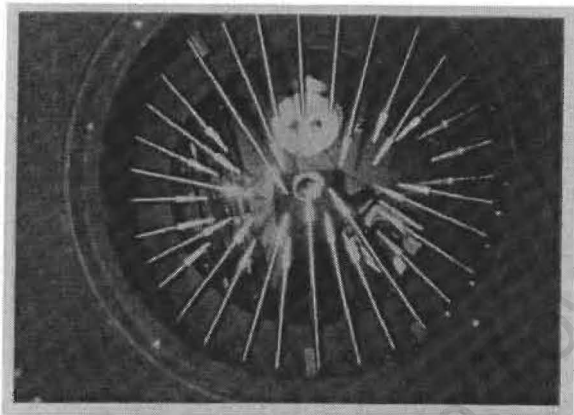


Figure 19: MX Spectrometer field configuration showing the “Fisherman-around-the-Pond” arrangement.

The telescope optics has a field curvature of 1.6m, which means that the focus on the edge of the FoV is 6mm higher than the centre. The MX-Spectrograph countered this by using a zoning method of alternative probes mounted tangent to the inner and outer regions of the focal surface. Each module allowed the probe to describe radial and angular motions, accomplished using stepper motors and gear chains (radial motion: rack and pinion; angular: spur). Each probe mapped a 24° sector of an annulus centred at the pivot point located beyond the edge of the field of view, just enough so that its 50mm head could work the edge of the field and not retract into the linear bearing constraining its radial motion. Each was free to see ~20% of the area of the field, a compromise between increased angular range and a decrease in the mechanical deflection of the probe at high radial extension. The closest approach of fibres was limited by fibre tip size. When very tightly packed fields were observed, an f/45 secondary mirror could be used to magnify the field of view and was called the “dense pack mode of operation”. The stepper motors were used in open loop control. Optical limit switches were used as fiducials for indexing the home position. The decision to use stepper motors (and spur gears) was made because they are ~3 – 4 times cheaper than the equivalent DC servo control. They used motors with a low holding torque, allowing it to be back driven through a gear train. In the case of a collision, a safety clutch had been built in, so that if a probe was obstructed in any way the motor would stall.

Motor specifications were chosen by considering the acceleration required. It was noted that the acceleration response is governed by inertial load placed on the motor, and that load is the inertia of the probe divided by the square of gear ratio (Hill & Lesser, 1986). However, for small masses driven through a reduction gear train, the system is dominated by the inertia of the rotor. The motor must therefore have enough torque to overcome friction in the gear train and its own inertia for a given acceleration rate. The precision accomplished by the modules was measured using a laser interferometer system. By mounting a corner cube retro-reflector attached to a probe tip, the probe response could be known to high accuracy and serve for anti-collision strategies requiring the probes position to be known with respect to adjacent positioners.

Anti-collision was ensured by software algorithms and two methods were discussed by the authors. One drew bitmaps of all the probes and checked that each element was not occupied by more than one probe. This procedure is expensive in memory. A second method mapped the outlines of the probes and knowing that only the probe tips and the inner radial bearing collide, intersections could then be searched for in order to prevent a collision. After each fibre arrangement the probes retracted, to reconfigure for the next field, angular adjustments were first made and then the radial extension was executed. Finally, there was a hardware override guaranteeing it to be failsafe. Each probe was mounted on an insulating fibreglass block with a shut down on electrical conduct between any two probes. (Hill, et al, 1982; Hill & Lesser, 1986; Hill, 1988).

2.4.2.2 Multi-Fibre / Single Positioner (AUTOFIB-Type)

The advantage of AUTOFIB-type devices, is the ability to deal with several hundred fibres. They have their fibres mounted, usually with a prism and sometimes corrective “microlenses”, onto magnetic “buttons”. These buttons are positioned on a backing plate, behind the focal surface, by a single robotic gripper on an X, Y, Z motion gantry. The first example (called AUTOFIB) was developed at the Anglo-Australian Observatory (AAO) in 1987 for use on a wide field Schmidt Telescope and used 64 fibres. The AAO has since commissioned an instrument called “2dF”, in 1997, with 400 fibres.

2.4.2.2.1 AUTOFIB

Durham University (England) and the AAO developed a 64-fibre instrument, called AUTOFIB, for multiple-object spectroscopy at the Cassegrain focus of the AAT. It represents an alternative model of automated fibre positioning to Hill's MX-Spectrometer (refer §2.4.2.1.1) by using a single robotic positioner that manipulates the fibres on a backing plate behind the focal surface. The fibres were arranged equiangularly about the field plate (see Figure 20) and were protected within hypodermic needles that would slide through pivot blocks. The fibres terminated in cylindrical stainless steel buttons orientated perpendicularly to fibre. A 90° prism was used to fold the light from the telescope into the fibre and a SmCo (samarium-cobalt) magnet in its base fixed the button to the backing plate. The field plate and fibres formed a fibre-box module that allowed for varying fibre options (different core diameters and even FOCAP's [see §2.4.1.1.2] plugboard) to be placed at the focal surface. The positioner consisted of a high-speed X-Y carriage and electromagnet that picked up the buttons. The carriage, which covered an area 380mm square, was constructed from recirculating linear bearings driven by zero-backlash ballscrews and DC motors encoded with linear transducers. The fibre manipulator mounted to the carriage required 30mm travel in the Z-axis that was achieved using a small lead screw and DC motor with a potentiometer. An electromagnet that exerted a force 80% greater than the magnet holding the housing to the backing plate picked it up for relocation. A pick up sequence of lowering the gripper, turning the electromagnet on and raising the gripper took 2 seconds, while the release operation (involving degaussing) took 3 seconds. Because the fibres were not handled in the same way that the FOCAP fibres were (that is manipulated by hand), longer fibre life and quality were expected (Parry & Gray, 1986; Parry, 1988).

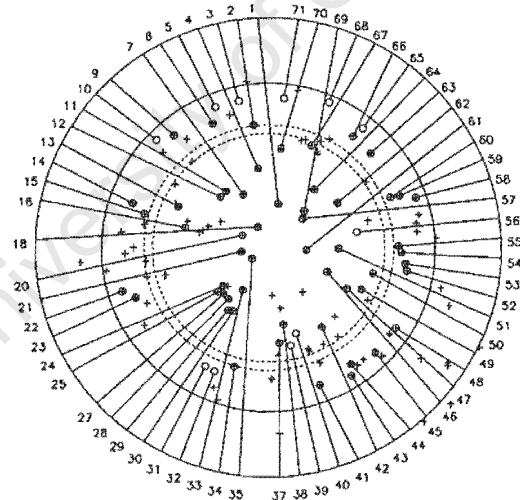


Figure 20: AUTOFIB field configuration showing the fibres mounted equiangularly about the field.

2.4.2.2.2 HYDRA

The multiple object spectrometer for the 4m Mayall Telescope at Kitt Peak National Observatory, Tucson, Arizona, could observe ~100 objects. An “AutoFib type” positioner, with an X, Y gantry and Z gripper mechanism, positioned fibres on a 460mm diameter backing plate. The fibres were mounted, with prisms, in cylindrical buttons (held to the backing plate by NdFe [neodymium-iron] magnets) that were protected in the positioning space by 410mm stainless-steel protection sleeves (hypodermic needles). The sleeves slid through pivot-blocks that were equally spaced about the backing plate. To account for

field curvature the plate had two 2mm steps at approximate radii of 125mm and 175mm, which resulted in the fibre never being out of focus by more than a millimeter. The gripper used three sprung-loaded "iris-type" jaws to pick up the fibre buttons and had a pellicle to enable video inspection down the axis of the gripper mechanism. Offsets in the concentricity between the button diameter and the mounted core diameter were measured for each individual fibre and placed in a software look-up table. Fibres were then positioned according to the tabled offsets (Barden, et al, 1993).

2.4.2.2.3 2dF

The 2dF is one of the most ambitious of all fibre positioners in its successful attempt to position 400 fibres to 10 μm accuracy in the two-degree field (560mm in diameter) of the 3.9m Anglo-Australian Telescope. It can reconfigure a field in half an hour, which means that each fibre must be positioned in 4 – 5 seconds. This prime focus instrument has two backing plates on either side of a tumbler (refer Figure 21), so when 400 fibres are "observing" another 400 are being set up on the reverse-side. Two identical spectrographs are mounted up at the top end of the telescope in order to reduce the light loss by having longer fibres. Each accommodates 200 fibres from the observing field and uses a slit switchover mechanism to see the 200 fibres from the other side of the tumbler. The tumbler rolls over for the next exposure and the slit mechanism on each spectrograph toggles. The 400 fibres (7.5m long and $\phi 140\mu\text{m}$ core), mounted on buttons, are ordered in 40 cassettes of 10 fibres around the edge of the field. Four cassettes incorporate guide fibres that comprise of 7 smaller (95mm) fibres in a close pack hexagonal bundle. Fibres are held taut by retractor units that use springs and pulleys instead of the hypodermic needles used by AUTOFIB.

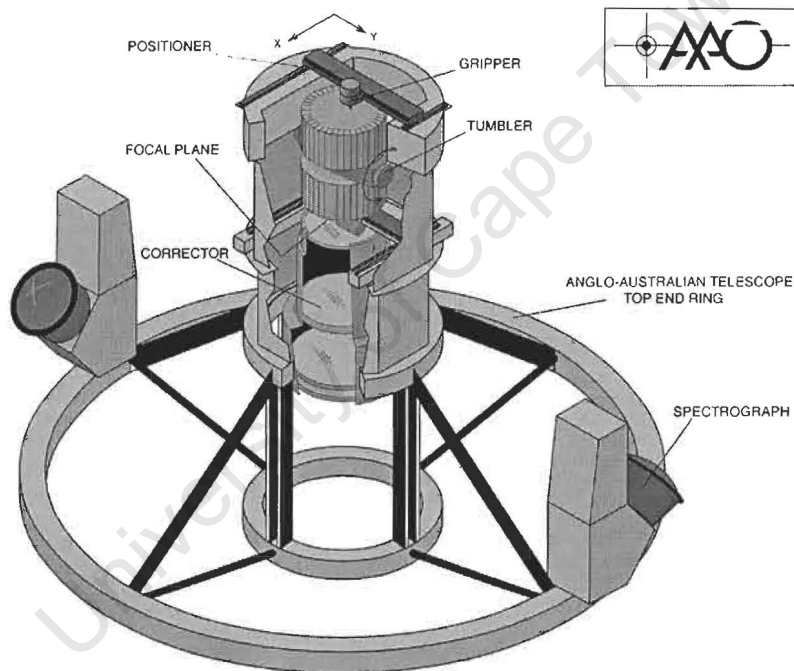


Figure 21: AAO, 2dF schematic (Lewis, 1998)

A gripper constructed in 4 modules maneuvers the buttons:

1. The jaw module - one of the jaws is fixed while the other is free to clasp against it. This gives slightly better control over the positioning because there is one less degree of freedom to add uncertainty to the system. The moving jaw is mounted on a crossed roller bearing, actuated by a miniature ball screw and driven via a gear pair by a permanent magnet motor. The assembly is encoded and has an inductive limit switch that indexes in the fully open position.
2. The θ drive module - this rotates the jaw module and uses slip rings for electrical contacts and a single bearing to support it.
3. The camera optics module - includes a small CCD camera with a dual focal length allowing it to focus on fiducial fibres (see below) in both the retracted and engaged positions. It protrudes through the centre of the theta motor module.

- The Z-drive module - the assembly of modules (1-3) is mounted on a rack and pinion system to gain this motion. It is guided by encoded roller slides. It is not counterbalanced.

The gripper assembly is mounted to a counterbalanced X-Y gantry that uses brushless DC linear motors to drive it. The gantry has fail-action brakes in the case of power failure. The magnetic stainless steel backing plates, Ø540mm and 1.2mm thick, has 21 backlit fiducial fibres, flush to the backing surface, that are illuminated when required by LEDs. The camera module on the gripper uses these as reference points to ensure accurate positioning of the fibre buttons (Lewis, et al, 1998).

2.4.2.3 Hybrid Designs

2.4.2.3.1 SPALTSPINNE & FELDSPINNE

Fibre positioner hybrids include the SPALTSPINNE and FELDSPINNE (both 36 fibres) instruments, developed at the Max Planck Institute for Astronomy in Germany, for the 3.5m Calar Alta Telescope and 2m Schmidt Telescope at the Karl Schwarzschild Observatory, respectively. These have their fibres mounted on probes protruding into the image plane in the MX-type "Fisherman-around-the-Pond" arrangement (Label G in Figure 22) where the probes maneuver in θ and R through pivot blocks (Label B). Magnetic buttons, in the same style as the AUTOFIB-type system, are connected to the rear of the probes (Label F) and positioned on a ferromagnetic stainless-steel backing annulus outside the field (Label A). There is a single gripping robot for fibre positioning that rotates about the field (Labels C, D, E). Advantages of this system include the closest approach of the fibres not being limited by the size of the buttons, but by the slenderness of the probes, and the positioning mechanism is simplified (Pitz, et al, 1993; Pitz, 1993; Pitz, 1988).

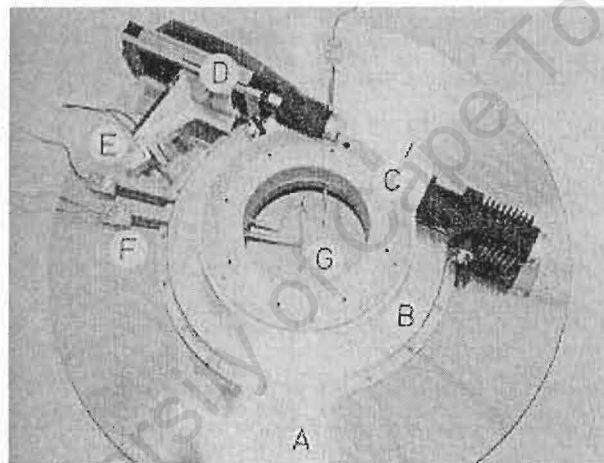


Figure 22: Prototype of SPALTSPINNE: A = Base plate, B = Ring with 36 pivot point assemblies, C = Rotary table, D = Linear table, E = Interlock tool, F = Two magnet-rod assemblies, G = Three fibre support rods protruding in the field of view of the telescope (Pitz, 1988).

2.4.2.4 Novel Designs

2.4.2.4.1 DECASPEC

This is similar in approach to the multiple object capabilities in Tubbs, Goss & Cohen (1982) multi-fibre instrument for the Hale Telescope (5m at Palomar Observatory) and Geary, Huchra & Latham (1986) multiple slits for a faint object grism spectrograph at the Multiple-Mirror Telescope (joint facility of the Smithsonian Institution and the University of Arizona). It was retrofitted to the Cassegrain focus of 2.4m McGraw-Hill Telescope using the existing long-slit spectrograph with the "DECASPEC" insert. It can observe 10 objects in the 20 arc-minute (100mm) field. Fibres are arranged in groups of five on ten fingers that protrude into the image plane, each finger can move linearly in and out (125mm) and has small lateral motion (2mm). The instrument is thus an X-Y type positioner that can be rotated about the optical axis to align with objects on the sky. The five fibres with core diameter 200 μ m are mounted at intervals of ~2mm, one is used for the object spectrum and the remainder used for sky subtraction (Fabricant, 1988).

2.4.2.4.2 MEKASPEK

MEKASPEK, a multi channel spectrophotometer, was developed at the Universitäts-Sternwarte München to study rapid variable phenomena in stars – dwarf nova eruptions, flare stars and eclipsing binaries (Mantel, 1999). It uses fibre bundles on each of four channels – one for the object, two for comparison objects and one for the background sky. The 800 μm diameter bundles are made of 130 fibres that are 70 μm in diameter. The fibre bundles have three purposes in this design: firstly to transfer the light from the focal plane to the spectrograph; secondly they scramble the light and thus remove the image motion due to seeing; and thirdly they allows for accurate photometric measuring of stars using the fibres simultaneously to monitor the sky and comparison objects (Mantel, 1999).

The four fibre bundles are positioned in a novel, non-trivial manner to $\pm 10\mu\text{m}$ accuracy and 2 μm repeatability. Each is positioned over a rectangular area in the image plane using two steel bands wrapped around rotating drums that are driven by stepper motors. By winding the bands individually, the probe can be positioned in space (see Figure 23; Mantel, 1993; Barwig, et al, 1998).

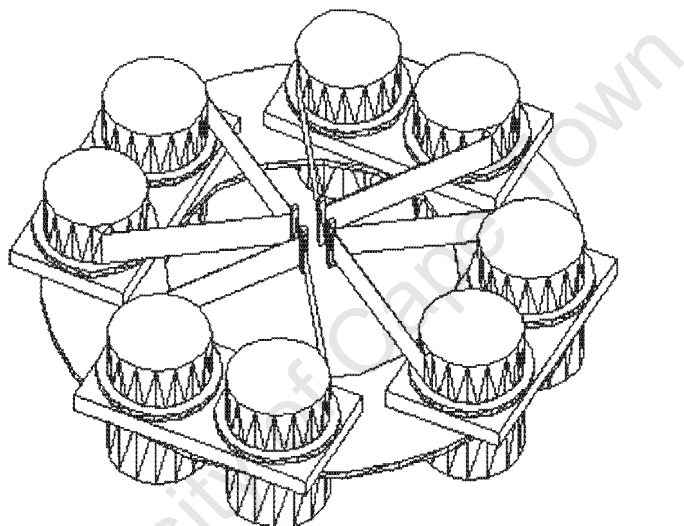


Figure 23: Solid Model of MEKASPEK showing the steel bands wrapped around rotating drums that position the fibre bundles in the field of view by winding and unwinding each of the drums individually.

2.4.2.4.3 ECHIDNA

This concept by the AAO is one that positions 400 fibre optics in the field of view (30 arc-minute or 143mm field) of the Subaru telescope in Hawaii. It uses a tripod constructed from silica tubing (~OD 0.46mm x ID 0.35mm x 140mm) mounted on a triangular (side: 4.5mm) aluminium base. One of the legs, or spines, carries a fibre optic inside it. The base is then mounted on three tiny linear actuators at its corners that enable tip and tilt; the tips of the spines (and the fibre optic) thus cover an area about 7mm in radius by tilting through an angle of $\sim 3^\circ$. Seven tri-motor assemblies are mounted in modules, which then arrange into a 61-piece array to cover the image plane. For dense clustering of celestial objects, seven adjacent fibres are able to come together to position onto the objects. Each spine describes a spherical surface with a difference of 0.175mm between the highest and lowest points because it was required to use motors that held their positions in the power off mode, to ease the control of the assembly, and motors with diameters less than 3.5mm, small nanomotors® were proposed (Gillingham, et al, 2000).

2.5 THE FIBRE INSTRUMENT FEED – THE HET EXAMPLE

One of the instruments mounted on the HET Prime Focus Instrument Platform (Figure 24) and carried by the tracker (as seen in Figure 25), is designed to enable studies of multiple objects in the telescope's field of view. The Fibre Instrument Feed (FIF) directs light from the focal plane down fibre optic waveguides to spectrographs in the basement. This chapter describes that instrument in detail.

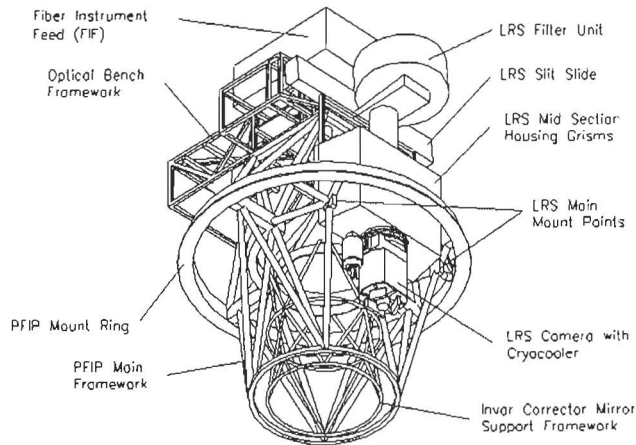


Figure 24: Schematic of the Prime Focus Instrument Platform showing the FIF situated on the top (Buckley & Sessions, 2000).

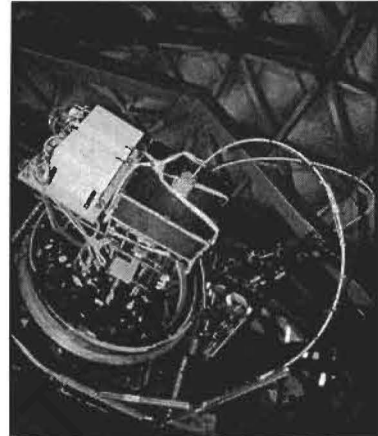


Figure 25: A picture showing the mounted FIF on the Telescope (Buckley & Sessions, 2000).

2.5.1 Overview

The HET has a focal plane 50mm or 4 arc-minutes in diameter about which 10 independently movable probes are positioned at increments of 36° (see Figure 26) in the “Fisherman-around-the-Pond” arrangement (refer §2.4.2.1).

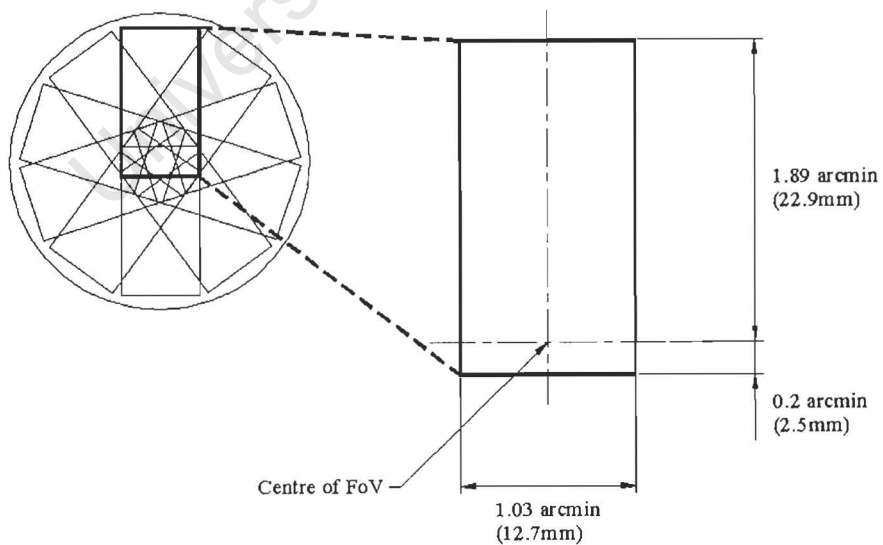


Figure 26: Field coverage of the probe (Horner, et al, 1998a,b).

Each probe maps out a rectangular area 12 x 25mm, 17% of the focal plane's area, with capability of accessing the central regions of the field. The probes are mounted, as shown in Figure 27, in three levels of actuators; there are two on the first level, and four each on the second and third levels. The illustration, for simplicity, only shows a representation of the probe protruding into the image plane. Figure 28 shows the elbow like probe carrying the fibre optic down to the focal plane.

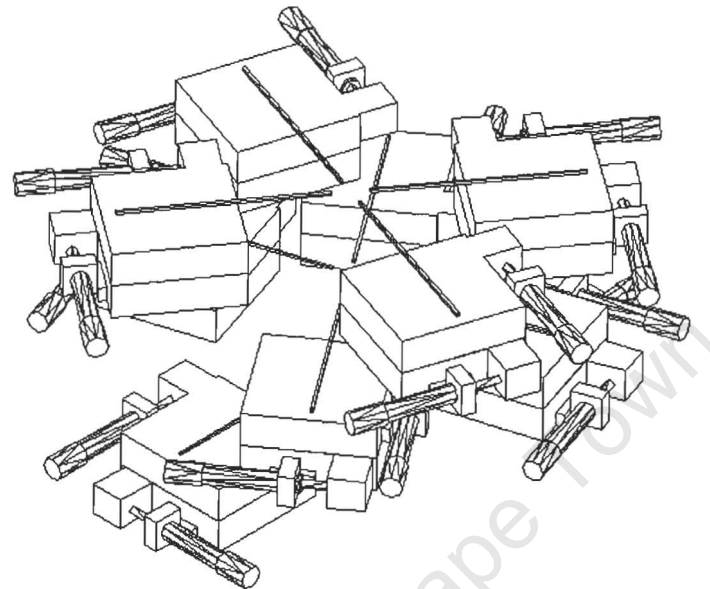


Figure 27: Solid Model of Actuator Layout showing three levels, two probes are actuated from the first level and the other eight are on two levels above that.

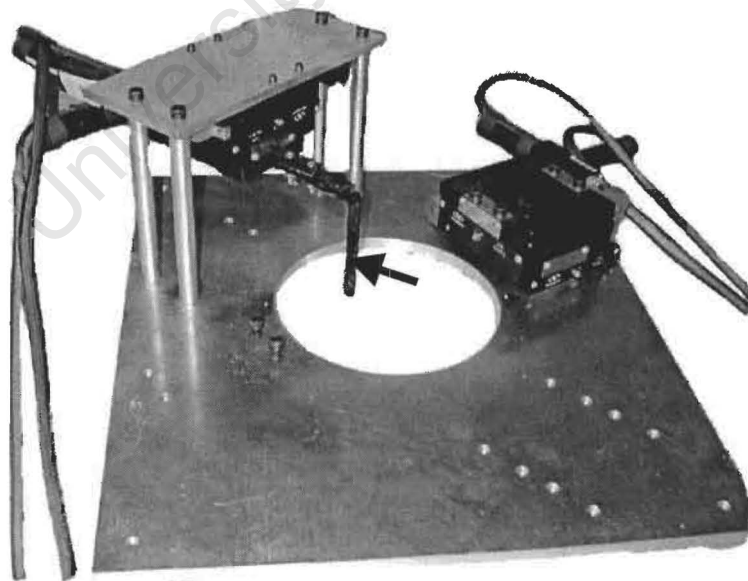


Figure 28: Prototype for the HET's FIF showing the elbow-like probe (indicated by the arrow) carrying the fibre optic to the focal plane.

Because the atmosphere tends to broaden the image of a star to form a “seeing disc” (see §2.2.1.2), three sizes of fibre optics, with core diameters of 300, 400 and 600 μm , are mounted in pairs on each probe to account for the variations. Because the *plate scale* of the telescope is 204.5 $\mu\text{m}/\text{arc-seconds}$, the fibre diameters represent $\sim 1.5, 2, 3$ arc-seconds, and are used in the appropriate seeing conditions. The second fibre of the pair allows a spectrum of a nearby region of sky to be subtracted from the object’s spectrum, thus removing the background signal.

2.5.2 Telecentric Angle Variation

Due to the optical configuration of the HET, a phenomenon called telecentric angle variation arises in the focal plane. In the simplification shown in Figure 29, it can be seen that when the telescope points at a star on-axis, the image is brought to focus on-axis. Stars off-axis are also brought to a focus in the image plane but the central ray of the bundle is inclined. This requires the fibre optics to be tilted away from the focal plane’s normal, more so as the object increases its radial distance from the centre of the field. Figure 30 shows the ZEMAX ray-trace of the telescope’s telecentricity.

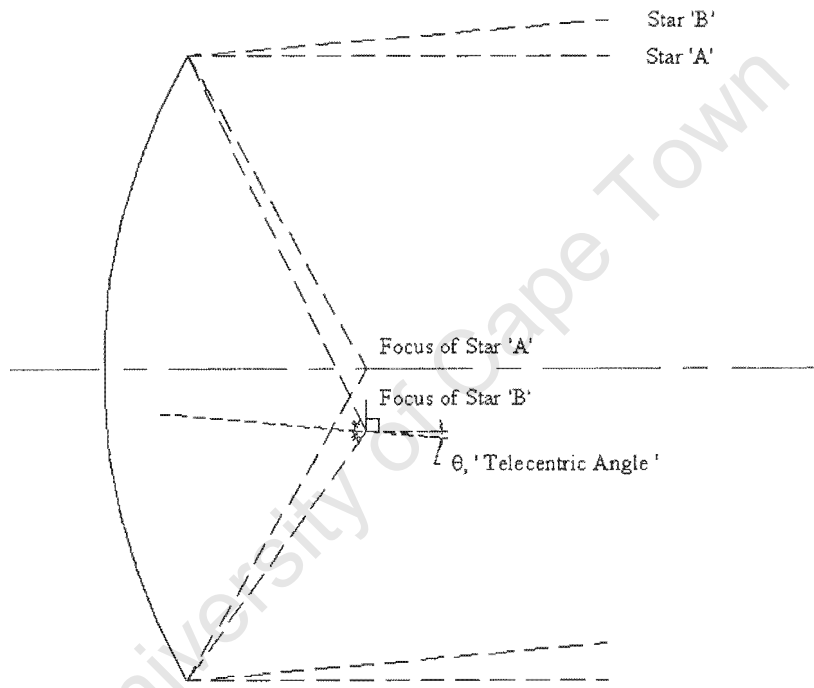


Figure 29: Telecentric variation explained. The image of star (A) on the optical axis is brought focus, the image of another star (B) is focused to the same plane but because it is off axis and the bisector of the angle is not normal to the plane, the chief ray describing the bundle of light rays from that star is inclined. This is called the telecentric angle.

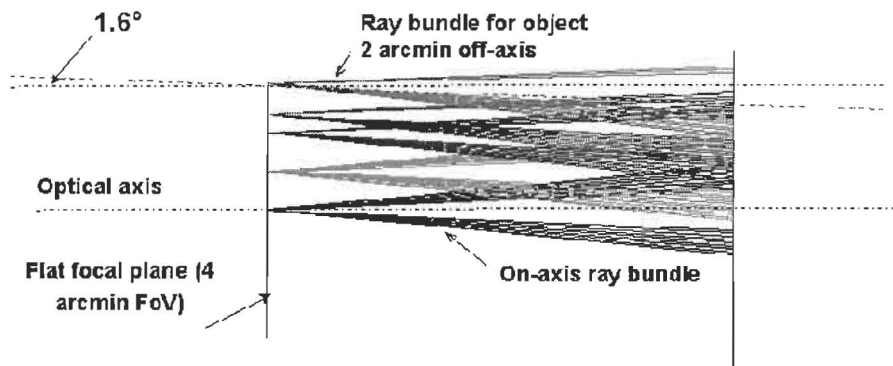


Figure 30: ZEMAX ray trace illustrating the telecentric angle problem for the HET.

The tilt angle is described as a function of radius (angle $\propto \tan(\text{radius})$), which increases to a maximum of 1.6° at the edge of the field (also see Figure 31).

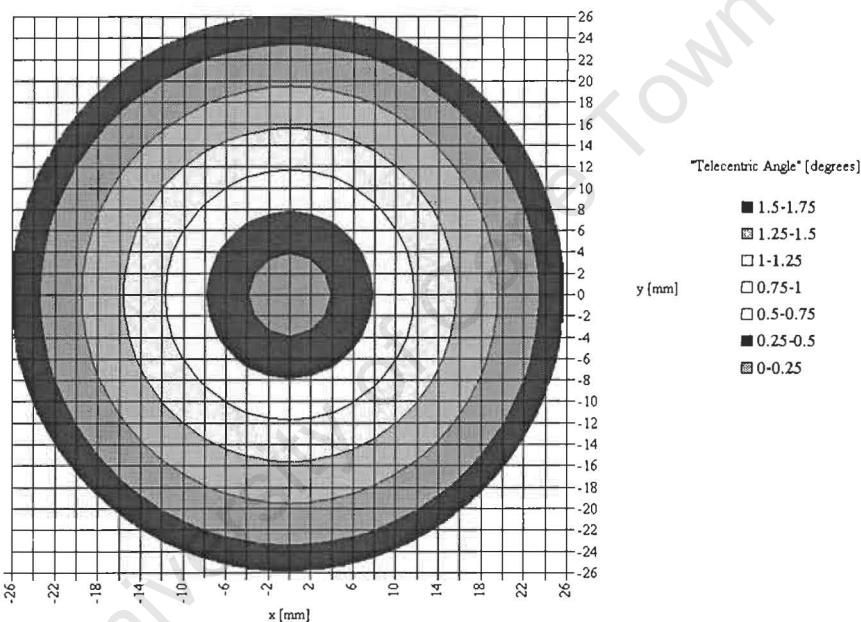


Figure 31: Telecentric angle over the field of view increasing as a function of radius from the centre ($x = 0; y = 0$).

3. THE HET PUPIL SIMULATOR

University Of Cape Town

3.1 INTRODUCTION AND OBJECTIVE

Because the HET/SALT design has a spherical primary mirror, and a tracker to follow the focus across the focal sphere as the sky rotates, the entrance pupil does not always entirely fill the mirror array. In the centre of the track, i.e. on the optical axis, the entrance pupil lies centrally on the array, but as it tracks, it “migrates” off, resulting in a smaller collecting area with the V-shape of the mirror array vertex cutting into the side of the pupil. A pupil that migrates off the mirror (refer §2.2.5, page 20; see Figure 9, page 23) decreases the effective diameter of the telescope, and hence light collecting power. This also introduces significant variations to the input to the fibre optic during an exposure (see pupil images pp.53-59), which is the subject of this section.

In terms of astronomy, the effect of varying inputs to the fibre potentially manifests itself in variations in the line-profiles or line widths obtained in the spectra of the celestial object. This is mainly because the dispersing element, collimating optics and camera optics, which are not perfect, undergo varying illumination. These variations increase the errors of high precision radial velocity measurements.

The objective of this investigation is to characterise the effects that the changing pupil shape, which is injected into the fibre optic, has on the output beam, which illuminates the spectrograph optics. A bench-mounted pupil simulator (see Appendix A; Figure 124, page 102) is used to this end (apparatus listed in Appendix B, page 104).

3.2 EXPERIMENTAL DESCRIPTION

3.2.1 Overview

A source fibre (FO#1; see Figure 32) is used to destroy the lamp's filament structure by scrambling. Additionally, it allows the fibre exit to be placed at the focus of the first mirror so that the light is easily collimated. A baffle fits over the ferrule carrying the source fibre replicating the central obstruction caused by the configuration of mirrors in the spherical aberration corrector (the hole in M2, see Figure 10, page 23). The collimated beam overfills a second mirror which then focuses the light into a second fibre optic (FO#2). The light is folded out of the transverse beam so that the positioning mechanisms do not influence the injected beam structure. A pellicle lens is used to fold the light while allowing the injection into the second fibre to be inspected along the same optical axis (as seen in Figure 32; also see Appendix A, Figure 125, page 102). This fibre guides the light to a testing rig. At the testing rig, near field images are recorded by collimating the output and imaging it on the CCD and far field images are recorded by projecting the output beam directly onto the CCD chip.

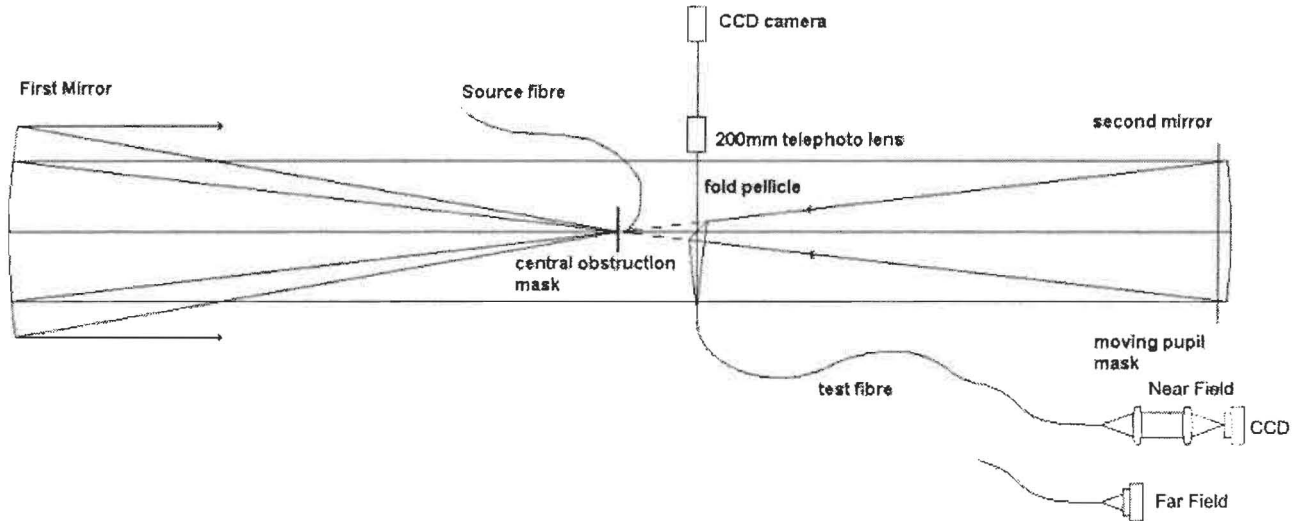


Figure 32: Schematic – Pupil Simulator. Note the central obstruction, the moving pupil mask and the test rig to record the near and far field patterns.

A sliding pupil mask at the location of the exit pupil (second mirror; see Figure 33) simulates the pupil migrating off the segmented mirror (cf. Figure 9, page 23). Far and near field data are taken for a number of equally spaced steps of the mask between the two limit positions shown in Figure 33. The convention used hereafter is m_0, m_1, \dots, m_6 , where the number corresponds to the number of degrees the tracker is off centred from the optical axis of the telescope.



Figure 33: Two limits in mask positions. The left image corresponds to on-axis (0°) and the right to the maximum off-axis position (6°).

3.2.2 Source Beam

The light from the source lamp (see Appendix C, page 105) is injected into the source fibre using a microscope objective that excites a large number of modes in the fibre because of its fast focal ratio. Filters can be placed in this beam, which are used to eliminate the colour dependency of the results (see Appendix D, page 106). The source assembly is shown in Figure 34.

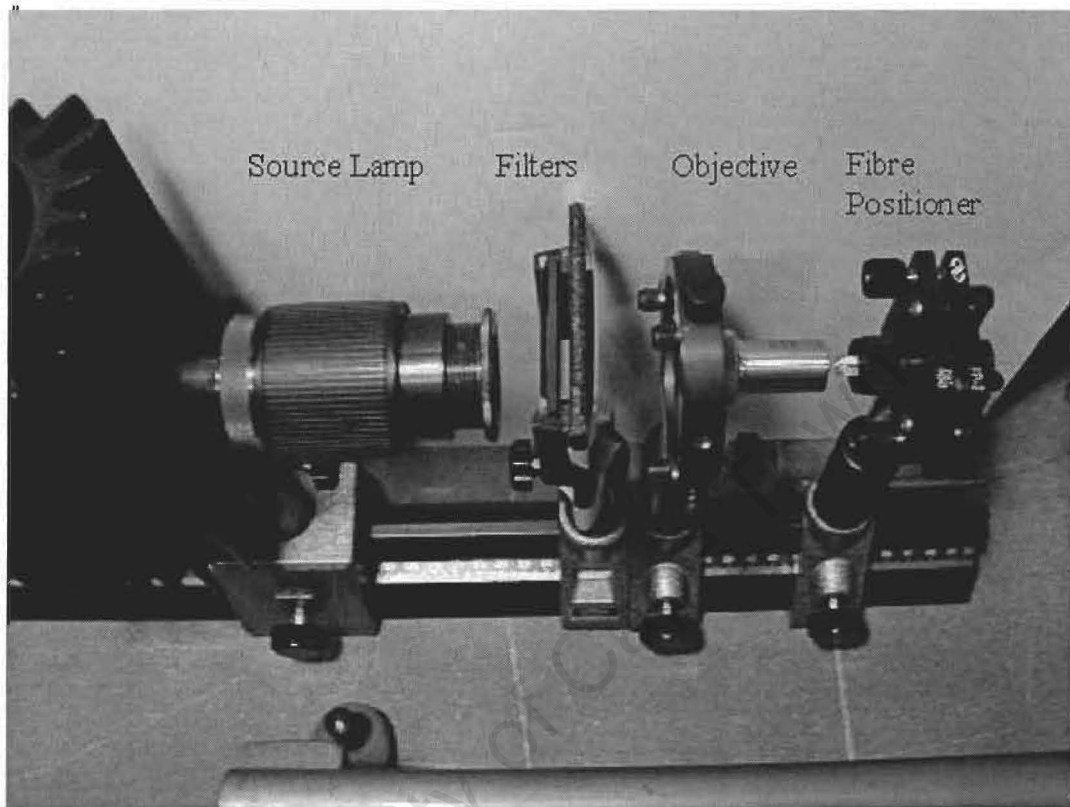


Figure 34: Source assembly.

The lamp was measured for stability and it was found that, after an initial peak in the intensity, it asymptotically approached some maximum value (see Figure 35). Data was obtained using a spectrograph to measure incident energy over time. An EXCEL VisualBASIC program was used to stitch together the data sets (see Appendix E, page 110) and plot the graph of lamp intensity with time.

The lamp is a *NEWPORT* model that happens to be in the obsolete product range. It was deemed insignificant that the lamp is not very stable over time, since the results are relative to each other and intensities may be scaled, either mathematically or by exposing for a longer period. It was always warmed up for a period of at least 30 minutes before it was used in order to overcome the initial peak.

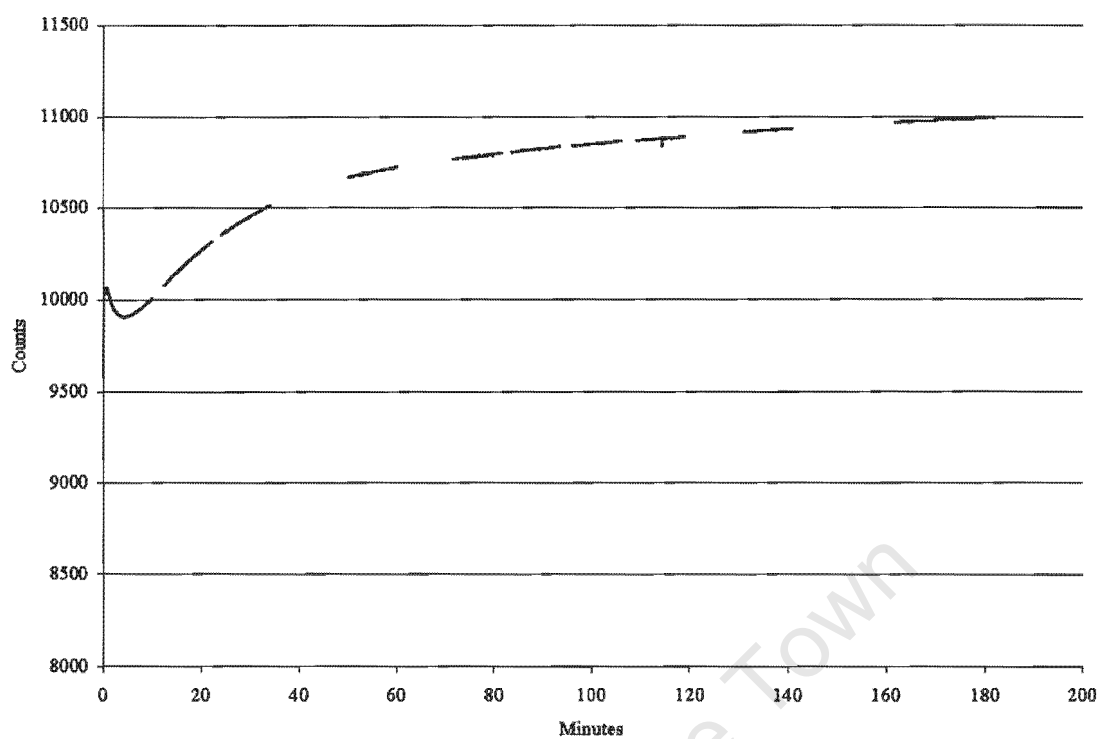


Figure 35: Lamp Intensity vs. Time. Note the initial peak.

3.2.3 Rig Alignment

It was found that the rig was sensitive to misalignment (see Appendix F, page 111) and so the following procedure was followed to guarantee optical alignment between all components:

1. Ensure that the primary mirror collimates the source beam and that the shadow of the “central obstruction” is concentric with that beam.
2. Adjust the secondary mirror so that it focuses the light onto the rear of the ferrule holding the source fibre (see Figure 36 and compare Figure 32).
3. Rotate the pellicle beamsplitter on its stage through 45°.
4. Backlight the second fibre with a laser (see Appendix A, Figure 126, page 102). By adjusting the tip/tilt of the input for the second fibre (now the exit for the laser beam) until the backlighting focuses directly onto the source ferrule, true alignment of the beam and the fibre axis can be obtained and verified because the laser can now shine into the source lamp.
5. Inspect the position of the injected beam on the fibre face with the inspection camera on the TV monitor (see Appendix A, Figure 125, page 102).

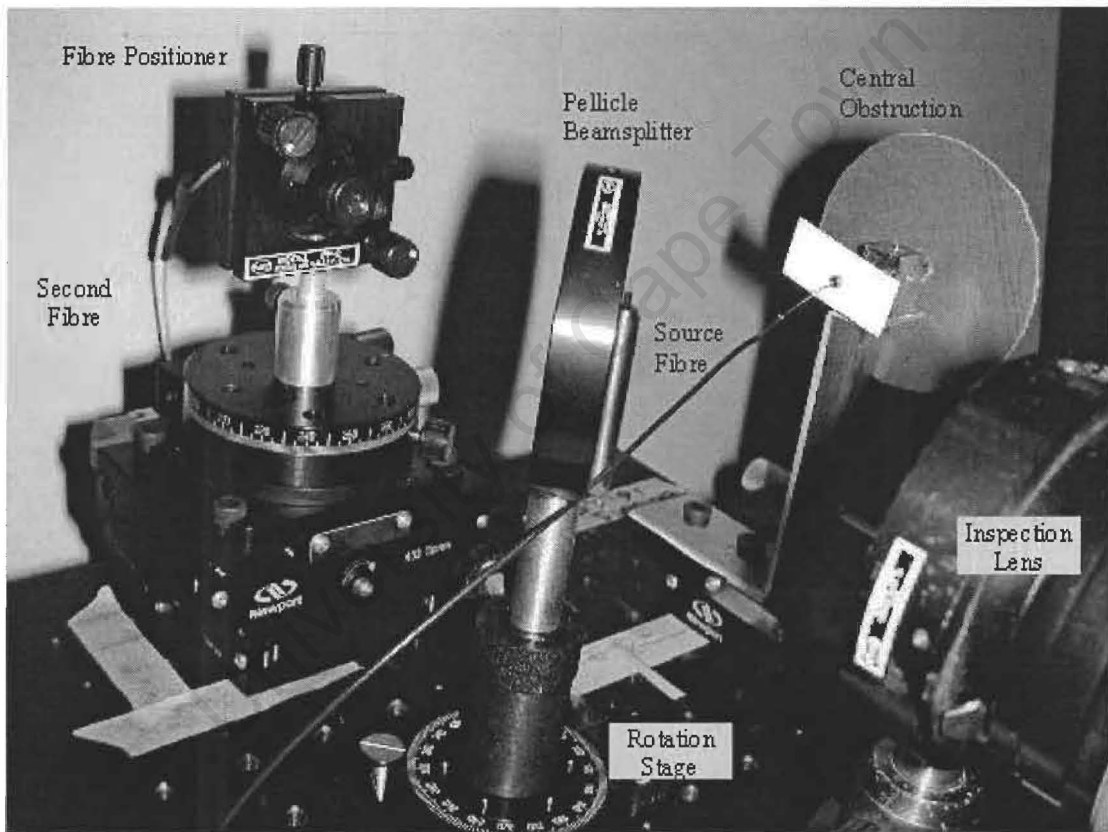


Figure 36: Central assembly.

3.2.4 Output

When imaging the far field pattern, the fibre was set up to project directly onto the CCD Chip of the ST-8 camera (see Figure 37), called bare field (code *bf* [refer §3.2.5.2]; the code *ff* applies to the far field pattern obtained from projections onto an opal screen, see Appendix A, Figure 127, page 103). To image the near field, a 50mm Photographic lens (focus set to “ ∞ ”) was placed near the output of the fibre to collimate the exiting light (see Figure 38; code *nf* [refer §3.2.5.2]). A 135mm Photographic lens (focus set to “ ∞ ”) was attached to the camera, magnifying the image of the fibre face by 2.7 ($\equiv 135/50$).

It was considered whether the beam projected directly onto the chip, called the bare field, was a good representation of the far field pattern, results were obtained for a number of positions where the distance between the fibre face and the chip were increased and the modulation and FWHM were deduced. Results are shown in Appendix G (page 114).

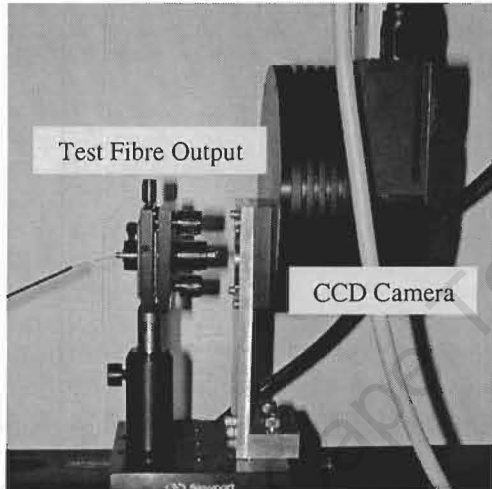


Figure 37: Setup to record far field (bare field) pattern.

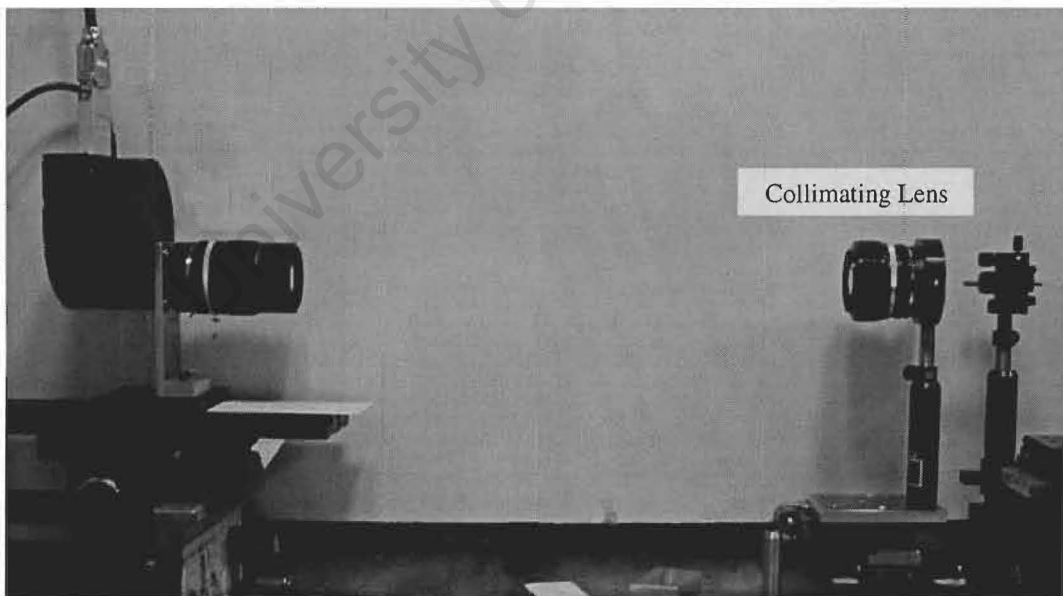


Figure 38: Setup to record near field pattern.

3.2.5 Images

Images were taken of the output beam of the second fibre optic for a number of mask positions in both the near and far field cases. It is also noted that the stray light in the lab was reduced to decrease the background noise in the images.

3.2.5.1 Image Processing

The reduction package IRAF (Image Reduction and Analysis Facility) and program *IMEXAM* were used to analyse the image data. A radial profile plot (*RIMEXAM*) was made of the image to obtain the centroid of the spot, this coordinate was then used to make a cross-sectional cut (*LIMEXAM*) through the centre. A typical cut is seen in Figure 39.

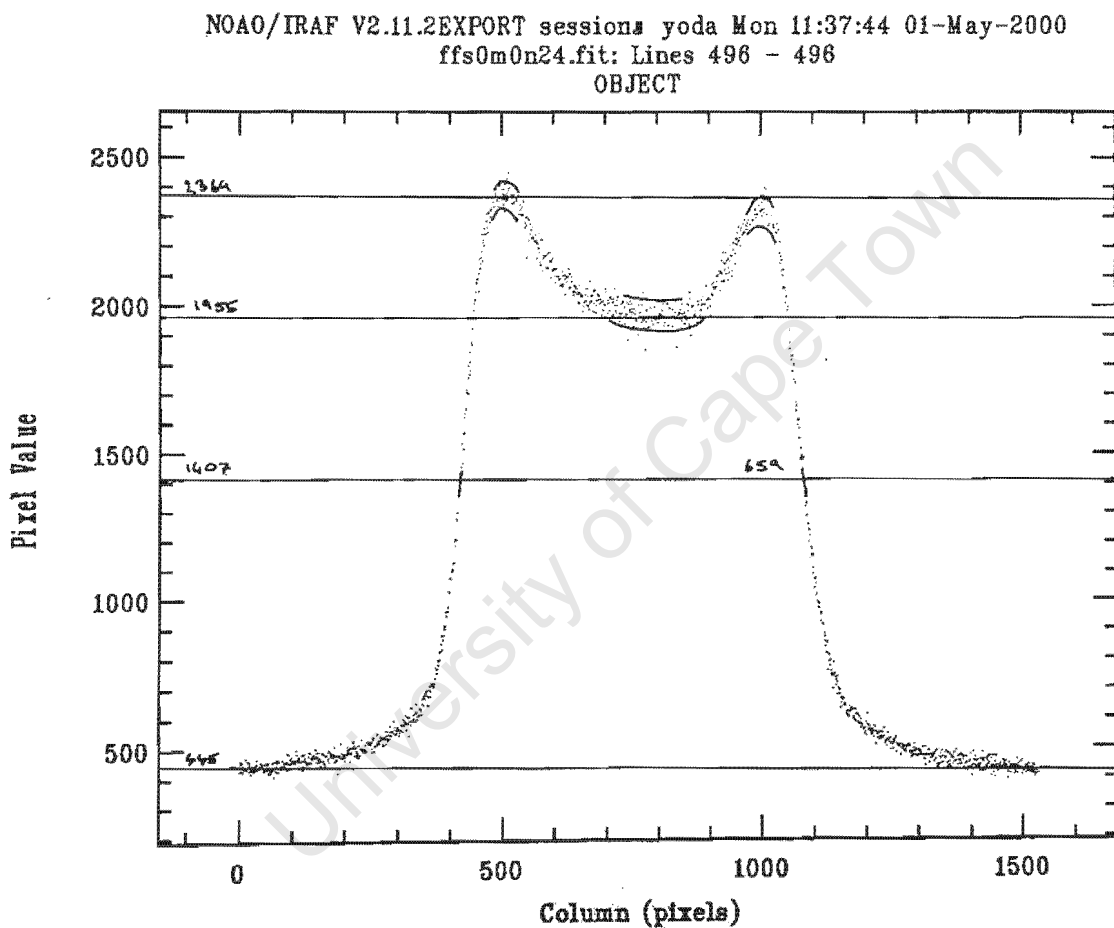


Figure 39: Using IRAF to obtain values of modulation and FWHM.

The peak, trough, background and FWHM values are obtained by roughly estimating the best fit curve though the scatter in the data points and measuring it with a vernier on the paper copy.

This was then automated by a Visual Basic Program in Excel. Example of the code reproduced in Appendix H (page 118).

The code suffered extensive justifications and verifications; see Appendix I (page 122) on the code written to find the centroid and Appendix J (page 128) for the comparison of the results to IRAF.

3.2.5.2 Naming Convention for image file results

Each image was saved with a name with the following format: AABBCCDEE.*

Where:

- AA is replaced with:
 - PS for imaging output from Pupil Simulator.
 - NF for Near Field images.
 - FF for Far Field images.
 - BF for Bare Field images
- BB is replaced with:
 - S0 when FO#1 is centred.
 - ... Sn ...
 - S5 in extreme telecentric case.
- CC is replaced with:
 - M0 when Mask is centred.
 - ... Mn ...
 - M6 in extreme position.
- D is replaced with:
 - N when not applicable.
 - R when FO#2 has been rotated through 1°
- EE is replaced with:
 - 01 with first set of data
 - ...
- * is replaced with the file extension.

The distinction between bare field (*bf*) and far field (*ff*) is only in the way it was recorded. Initially, the far field was measured by imaging an opal screen which had the fibre projected onto it (Appendix A; Figure 127, page 103). During the course of the experiments, it became apparent that it was possible to improve the results obtained by projecting the output of the fibre directly onto the CCD chip (Figure 37).

3.2.6 Fibre Preparation

The bare fibres were mounted in ferrules (see Figure 40) and attached with UV curing epoxy. The bare fibre (no buffers or jackets) was inserted through the rear of the ferrule (shown on the left in the Figure) to extend ~5mm beyond the front face (on the right). Epoxy was then placed in the middle of the front groove (indicated by the dimension of 12mm) to tack the fibre to the ferrule. By manipulating more epoxy with a needle, a cone was built up on the end that enclosed the extended fibre. This was then set under the UV lamp to cure. Once complete, the fibre face was polished in a machine where the lapping paper progressed from 60 μ m to finer 0.5 μ m grit to achieve a higher quality of polish.

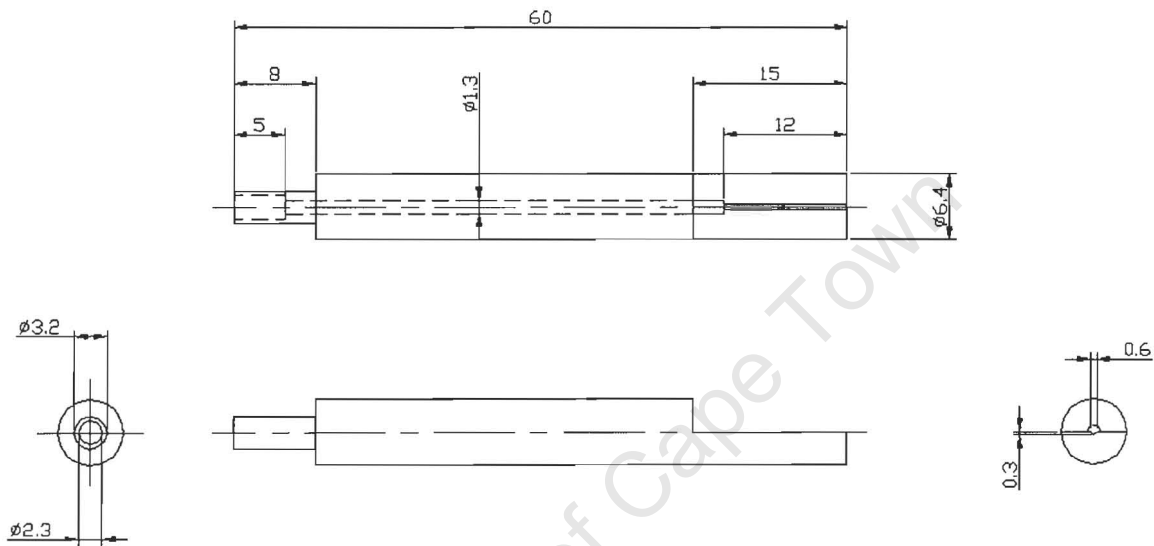


Figure 40: Machine drawing of ferrule (dimensions in mm).

3.3 GENERAL RESULTS AND ANALYSIS

3.3.1 Introduction

Five data sets are presented in this section; a summary is given in Table 3. The first set (31) was a set of data taken for varying mask positions, that is, m0 (corresponding to on-axis) to m6 (corresponding to the limit of 6° off-axis), where the rig has been realigned, and the method of acquiring data refined. The test fibre is a 9m long fibre with a core diameter of 400μm, it has ferrules mounted on both ends and polished to an acceptable standard, when observed under the microscope. The second set (32) of data are results from an existing fibre, 30m long with a 600μm core. The third set (33) of data are results from the first fibre once the epoxy had been dissolved off the exit face. The fibre in this case is held in the ferrule with masking tape. It was hoped that a measure of the effect that stress induced on the fibre by the epoxy could be obtained. The fourth set (34) was another test on the 600μm fibre once the fibre was re-mounted and re-polished. The fifth and final set (35) was the first fibre test with the entrance and exit epoxy removed. The three 400μm fibre tests thus show the result that the epoxy has on the output and the 600μm fibre tests show the results of improved polishing.

In the table below, the day of each test is shown because it was thought that there might be some time dependency in the results since once the epoxy has been dissolved, and thus the applied stress removed, there is the possibility that the fibre might relax over time (creep).

Data Set	Description	Day
31	9m 400μm fibre – after rig re-alignment.	0
32	30m 600μm fibre – with old epoxy and polishing.	1
33	9m 400μm fibre – no epoxy on exit face.	14
34	30m 600μm fibre – re-polished faces.	14
35	9m 400mm fibre – no epoxy on entrance or exit face.	16

Table 3: Table of data sets.

3.3.2 Comprehensive Data for Set 31 (9m x 400μm Fibre)

Data Set 31 are the final results following careful realignment.

3.3.2.1 Far Field Patterns

Four images, for each of seven mask positions, are presented in §3.3.2.1. The top left image (Figure 41) is the exit pupil of the simulator, the beam pattern that is injected into the second fibre optic. Beneath it (Figure 43) is shown a horizontal cross-section through the centroid of the exit pupil. Ideally a step function, its shape is due to the scrambled beam emerging from the source fibre. The image on the top right (Figure 42) is the corresponding far field pattern emerging from the test fibre optic due after injecting the pattern shown in Figure 41. Beneath (Figure 44) is a similar cross-section of the far field pattern. The intensity quantity on the vertical axis of the cross-sectional plots are of no significance since it is the relative change between images that is of consideration.

3.3.2.1.1 For Mask Positioned On-Axis ($m0$)

Note 1: Mirror mountings; **Note 2:** Defect on pellicle beamsplitter; **Note 3:** Example of dust particle on CCD window.

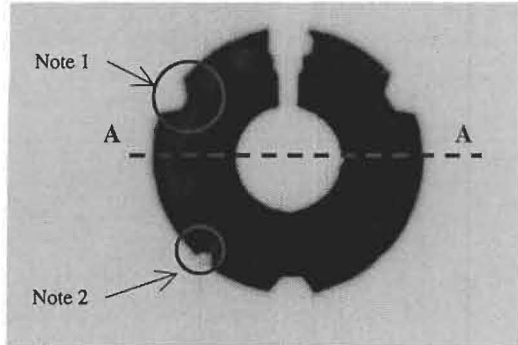


Figure 41: pss0m0n31.jpg

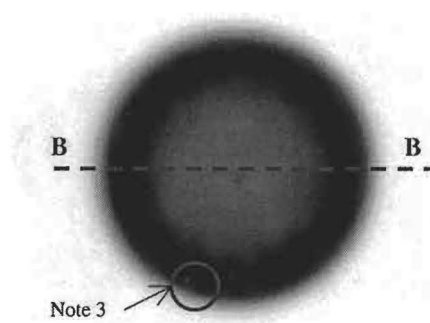


Figure 42: bfs0m0n31.jpg

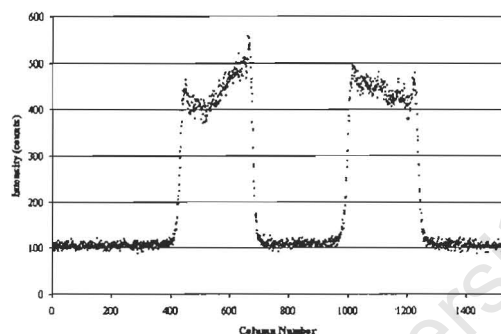


Figure 43: pss0m0n31cross-section (Section A-A).

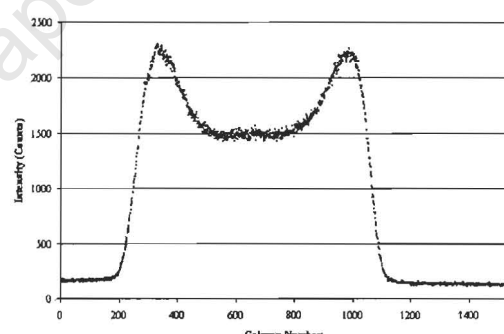


Figure 44: bfs0m0n31cross-section (Section B-B).

3.3.2.1.2 For Mask Positioned 1° Off-Axis ($m1$)

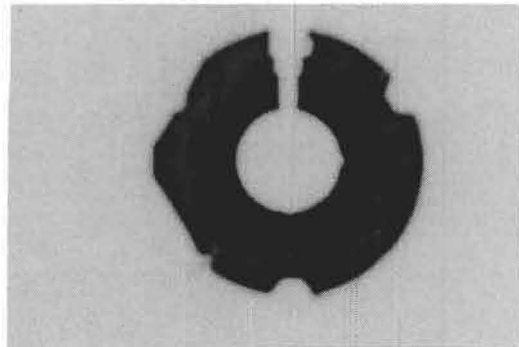


Figure 45: pss0m1n31.jpg

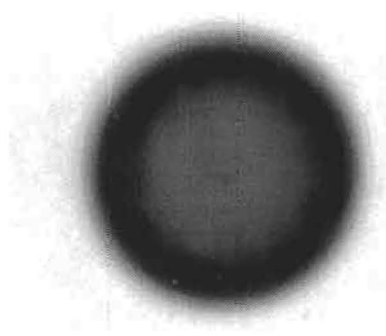


Figure 46: bfs0m1n31.jpg

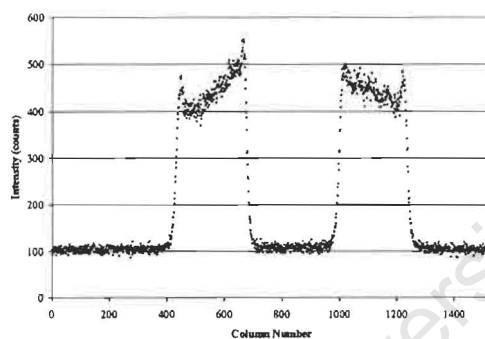


Figure 47: pss0m1n31cross-section.

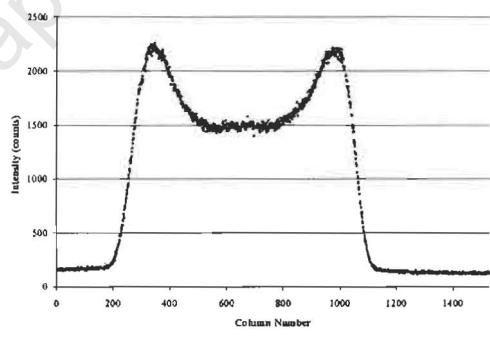


Figure 48: bfs0m1n31cross-section.

3.3.2.1.3 *For Mask Positioned 2° Off-Axis (m2)*

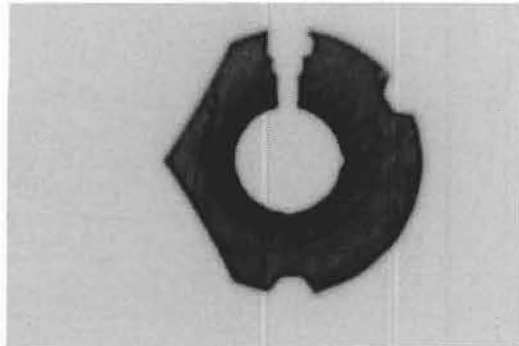


Figure 49:pss0m2n31.jpg

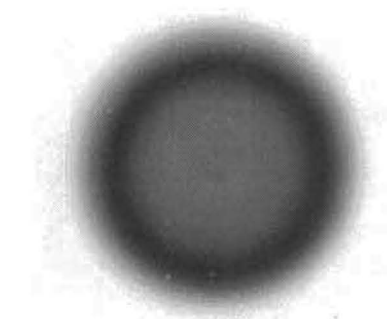


Figure 50: bfs0m2n31.jpg

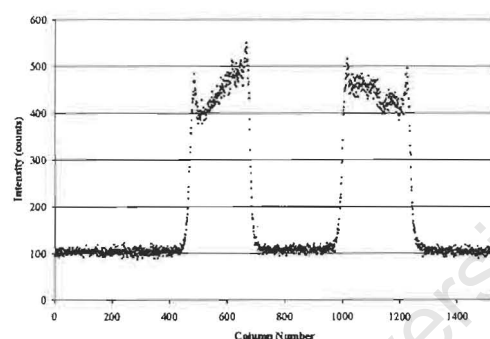


Figure 51: pss0m2n31cross-section.

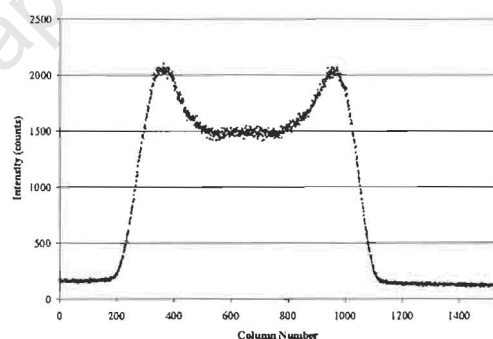


Figure 52: bfs0m2n31cross-section.

3.3.2.1.4 For Mask Positioned 3° Off-Axis (m^3)

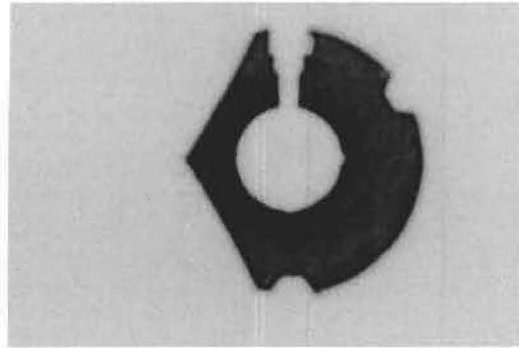


Figure 53: pss0m3n31.jpg

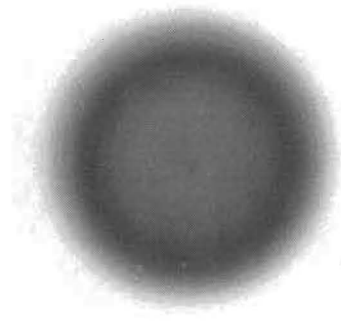


Figure 54: bfs0m3n31.jpg

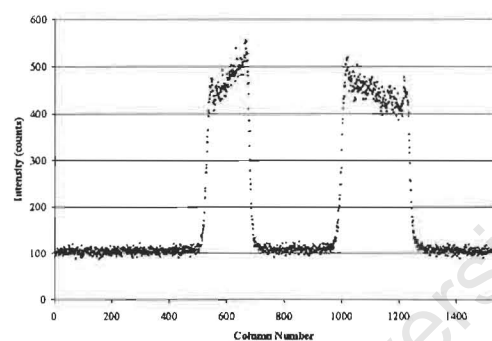


Figure 55: pss0m3n31 cross-section.

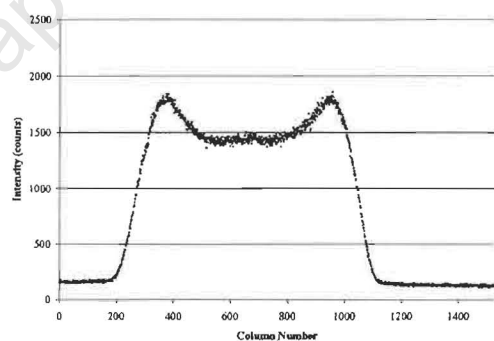


Figure 56: bfs0m3n31 cross-section.

3.3.2.1.5 For Mask Positioned 4° Off-Axis (m4)

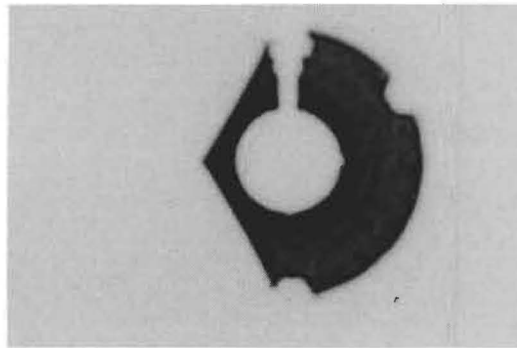


Figure 57: pss0m4n31.jpg

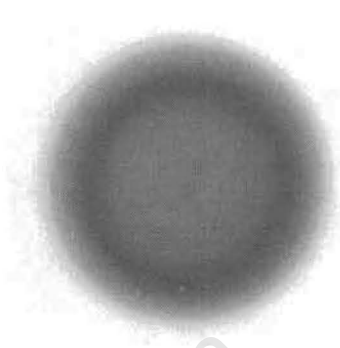


Figure 58: bfs0m4n31.jpg

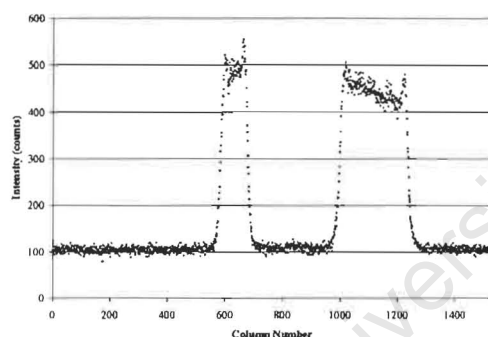


Figure 59: pss0m4n31cross-section.

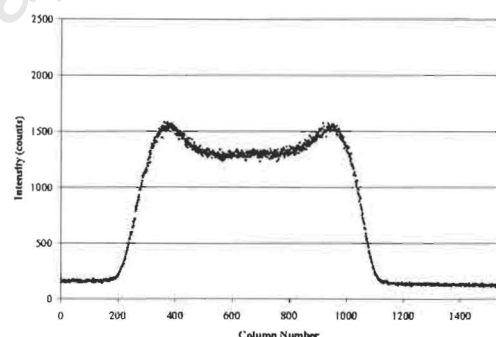


Figure 60:bfs0m4n31 cross-section.

3.3.2.1.6 For Mask Positioned 5° Off-Axis (*m5*)

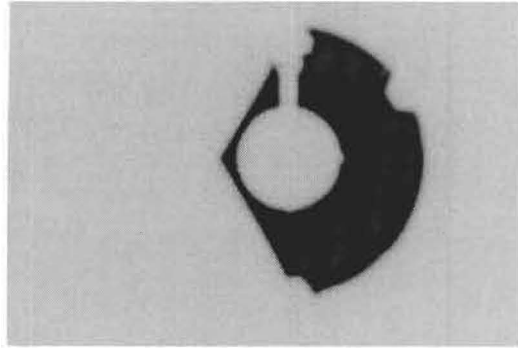


Figure 61: pss0m5n31.jpg

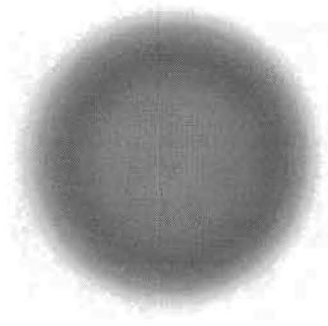


Figure 62: bfs0m5n31.jpg

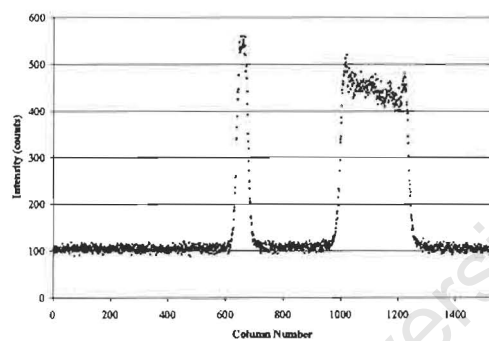


Figure 63: pss0m5n31cross-section.

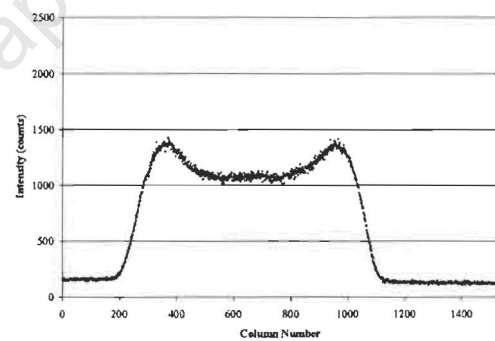


Figure 64: bfs0m5n31cross-section.

3.3.2.1.7 For Mask Positioned 6° Off-Axis (m_6)

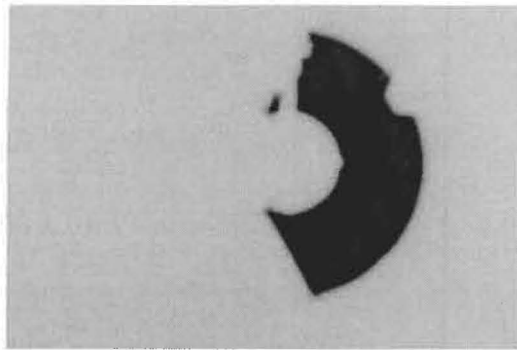


Figure 65: pss0m6n31.jpg

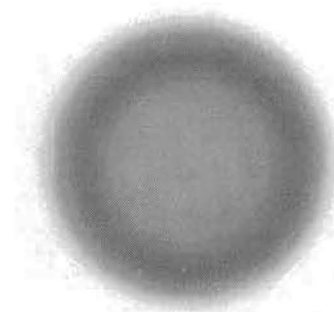


Figure 66: bfs0m6n31.jpg

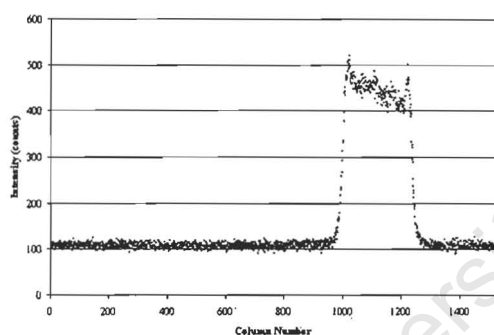


Figure 67: pss0m6n31cross-section.

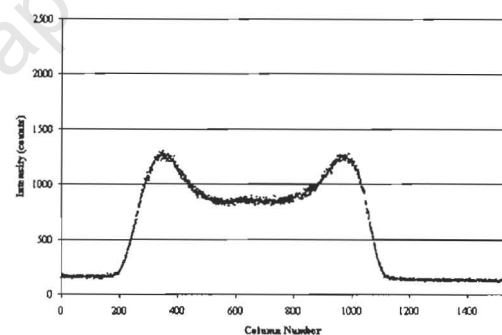


Figure 68: bfs0m6n31cross-section.

See Figure 74 (page 62) for an overplot of the bare field cross-sections.

3.3.2.2 Near Field Pattern

The near field images are presented here for three mask positions ($m0$, $m3$, $m6$); it shows that for varying mask positions the major effect is in intensity. No relative changes are seen as shown in Figure 73.

3.3.2.2.1 For Mask Positioned On-Axis ($m0$)

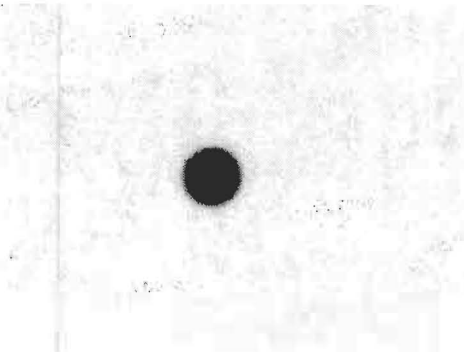


Figure 69: nfs0m0n31.jpg

3.3.2.2.2 For Mask Positioned 3° Off-Axis ($m3$)

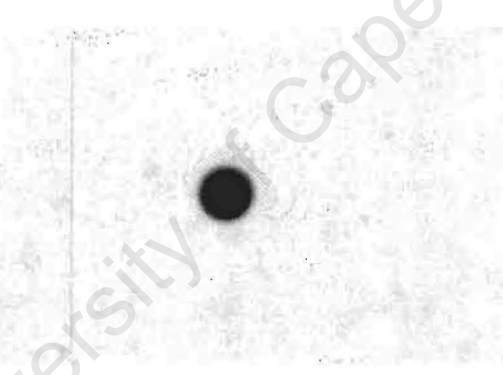


Figure 70: nfs0m3n31.jpg

3.3.2.2.3 For Mask Positioned 6° Off-Axis ($m6$)

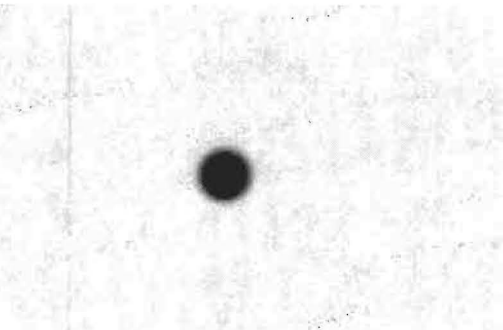


Figure 71: nfs0m6n31.jpg

3.3.2.2.4 Analysis

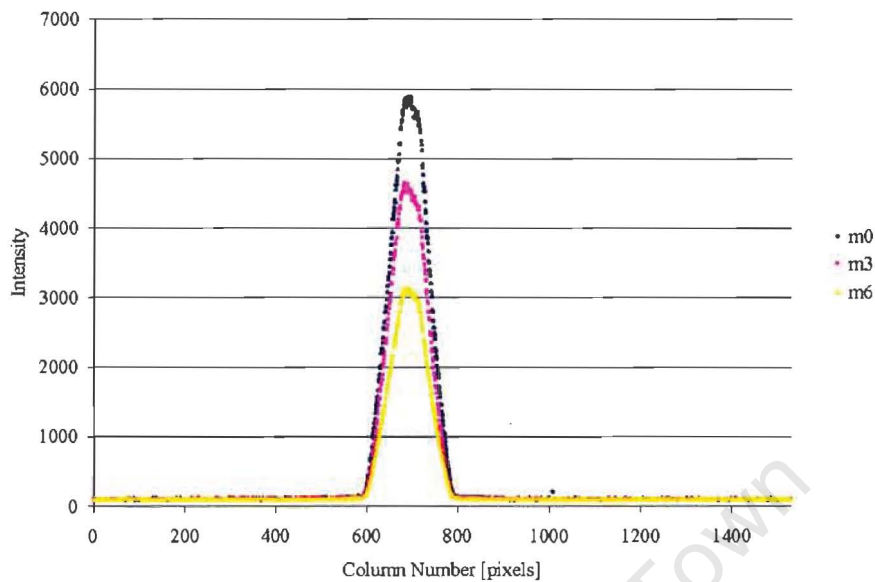


Figure 72: Set 31 Near field cross-section.

These curves were normalised to produce the following graph:

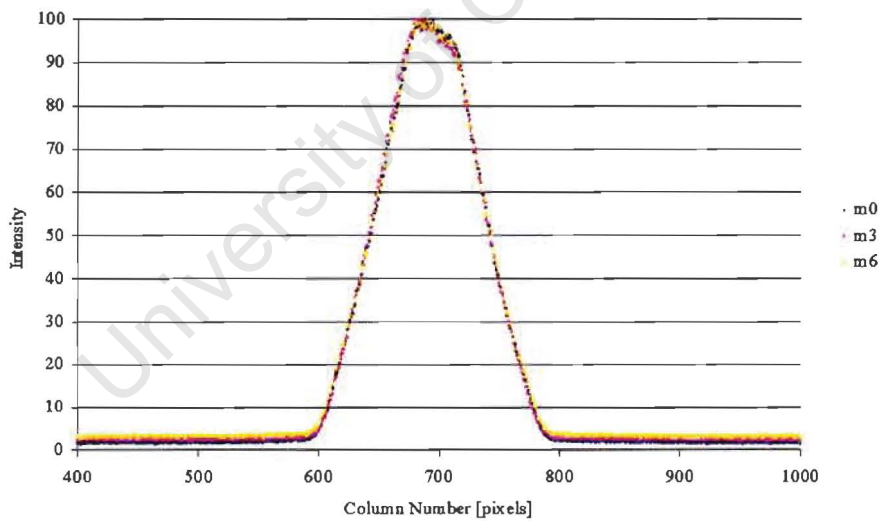


Figure 73: Set 31 Near field cross-section normalised.

It is seen that there is no significant effect in the near field pattern due to migrating pupil and it is therefore ignored in the following presentation of results.

3.3.3 Modulation and Width Results, Set 31 – 35

Without presenting each data set in the same detail as in §3.3.2, the data sets in this section are presented first with a superimposed plot of the output cross-sections (far field pattern), plots of the modulation and then plots of full width, for the mask positions m0 to m6.

The modulation is defined as the ratio of trough depth to peak intensity or exactly as:

$$M = 1 - \left(\frac{T - B}{P - B} \right) \equiv \left(\frac{P - T}{P - B} \right)$$

where T is the trough intensity, P the peak intensity and B is the average background intensity.

Following is a plot of the full width of the beam at two points: FWHM and FW13.5. FWHM is the width at half the maximum intensity and FW13.5 is the full width at $\frac{1}{e^2} \approx 0.135$.

3.3.3.1 Set 31 - 9m 400 μ m Fibre - After Rig Re-Alignment (day 0)

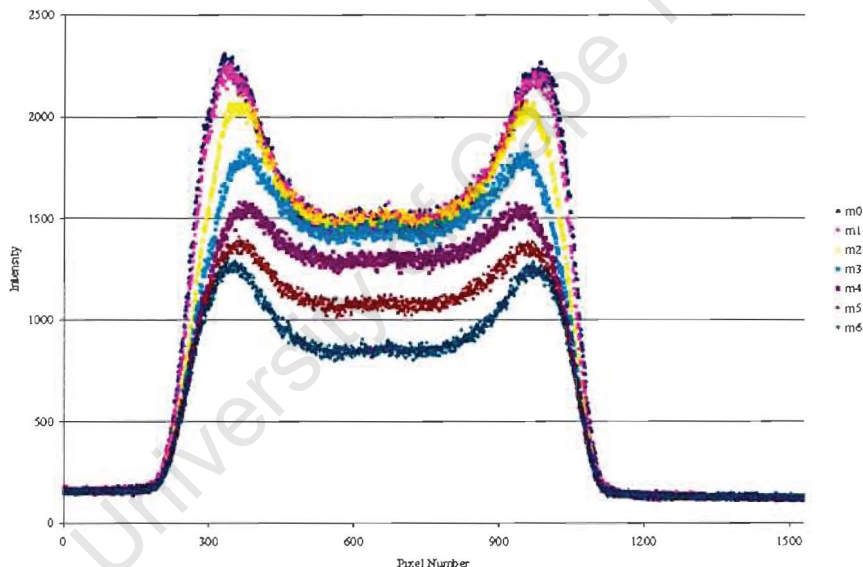


Figure 74: Set 31 overplot of cross-sections.

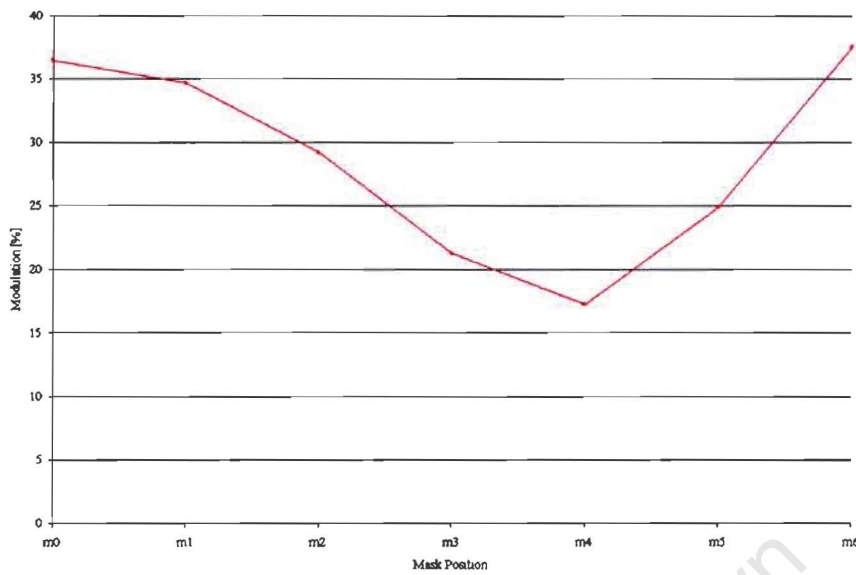


Figure 75: Set 31 modulation curve.

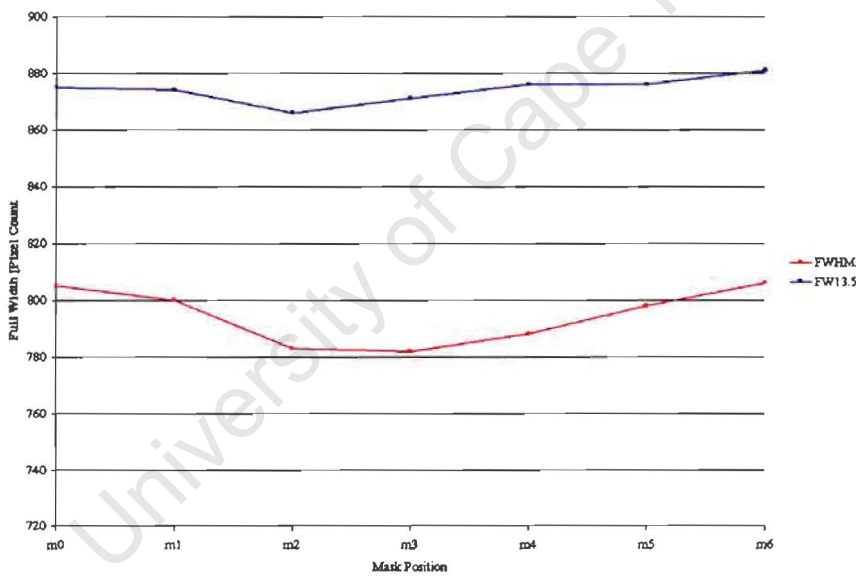


Figure 76: Set 31 full width curves.

3.3.3.2 Set 32 - 30m 600 μ m Fibre (day I)

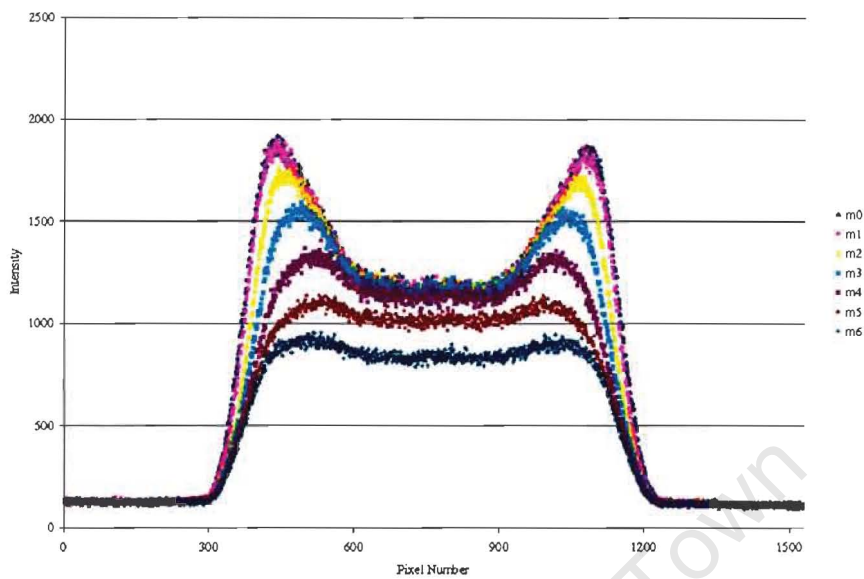


Figure 77: Set 32 overplot of cross-sections.

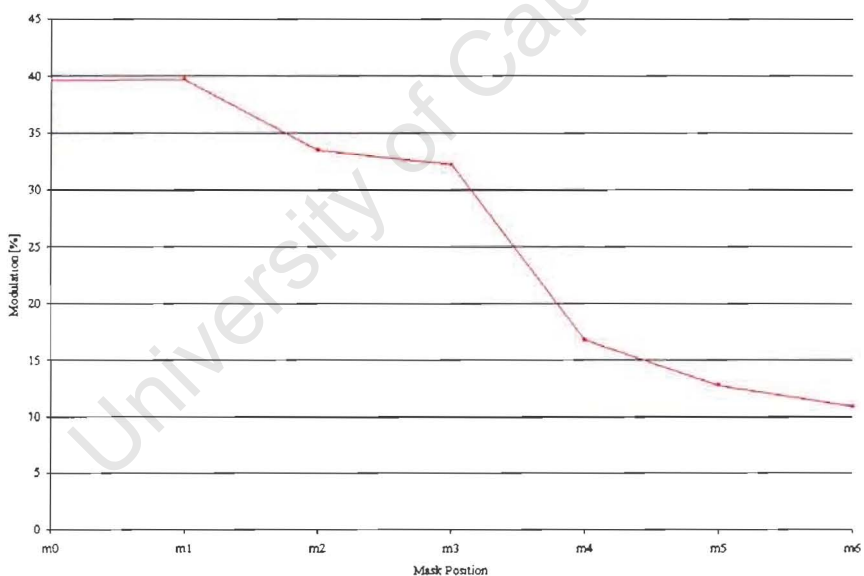


Figure 78: Set 32 modulation curve.

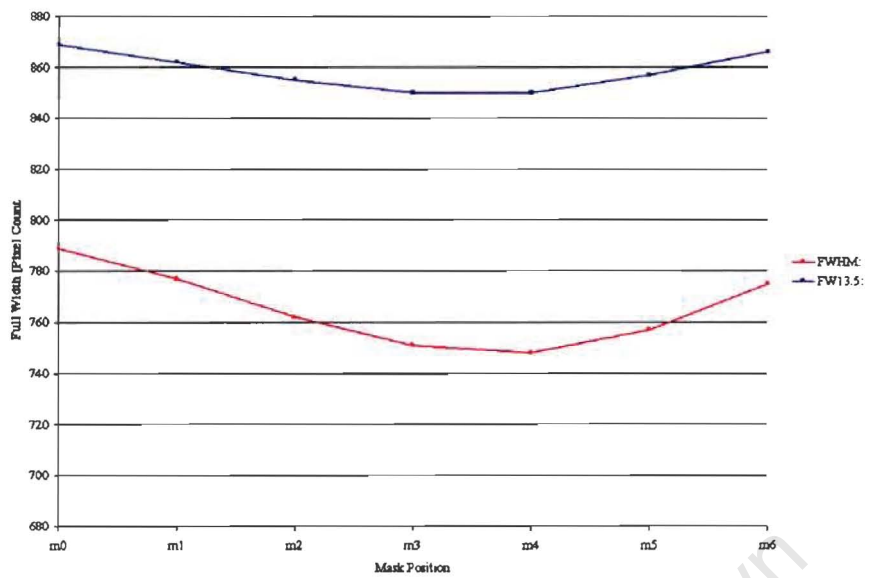


Figure 79: Set 32 full width curves.

3.3.3.3 Set 33 - 9m 400 μ m Fibre - No Epoxy on Exit Face (day 14)

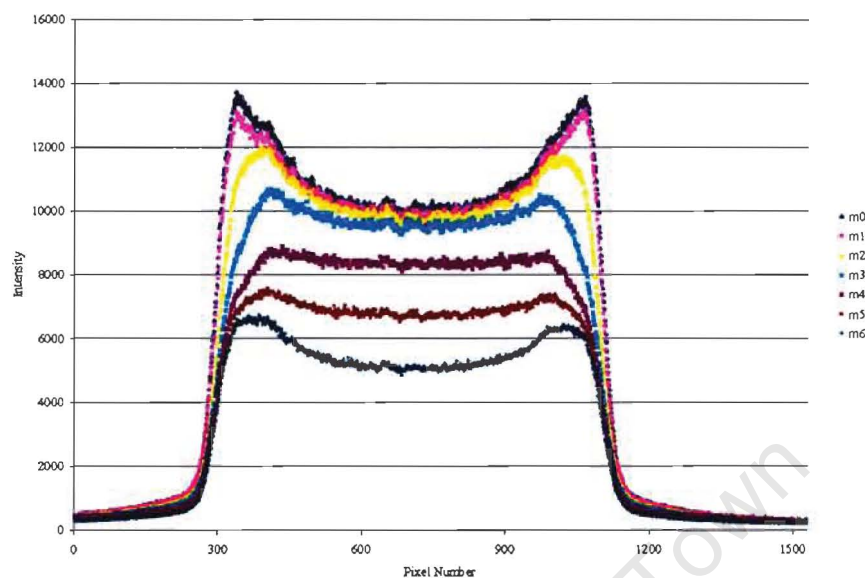


Figure 80: Set 33 overplot of cross-sections.

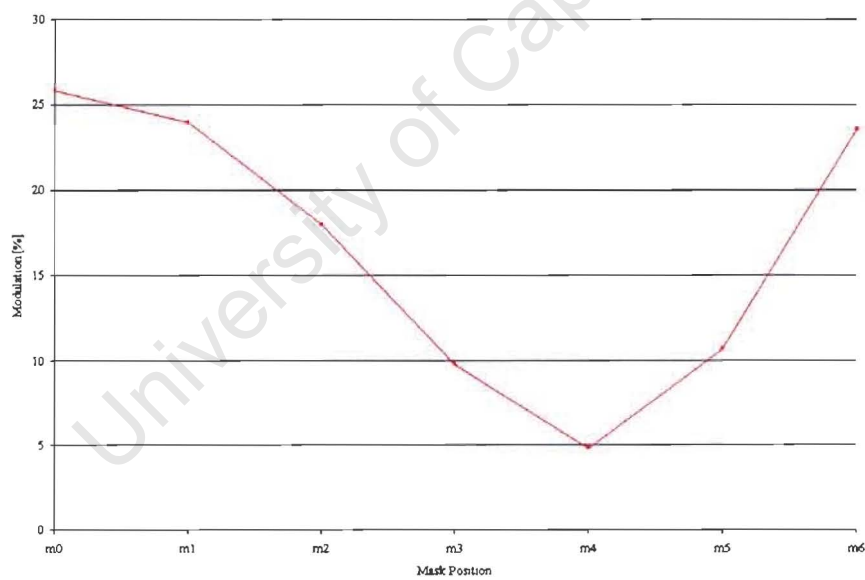


Figure 81: Set 33 modulation curve.

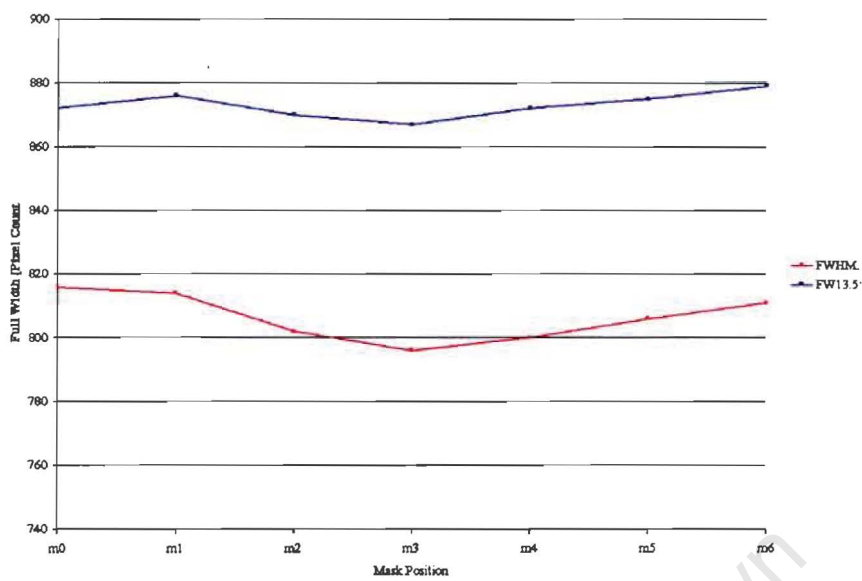


Figure 82: Set 33 full width curves.

3.3.3.4 Set 34 - 30m 600 μ m fibre - Re-Polished Faces (day 14)

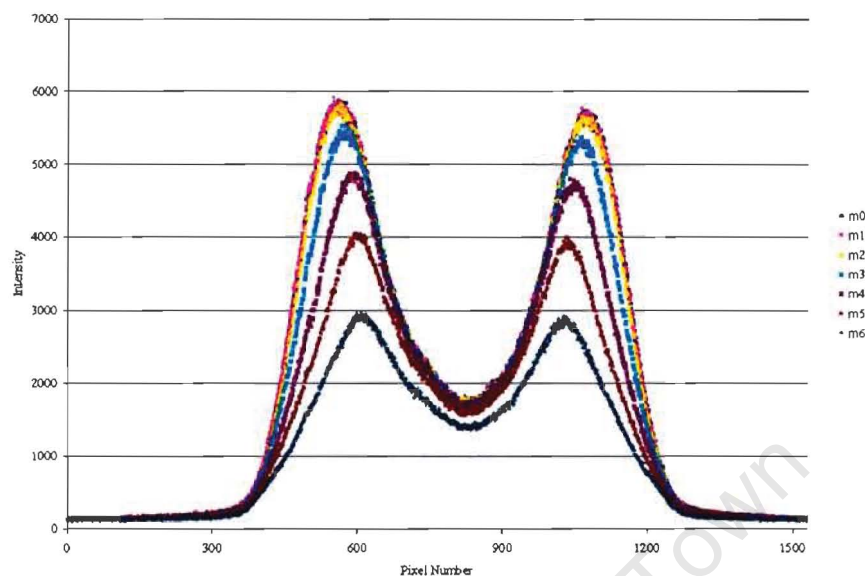


Figure 83: Set 34 overplot of cross-sections.

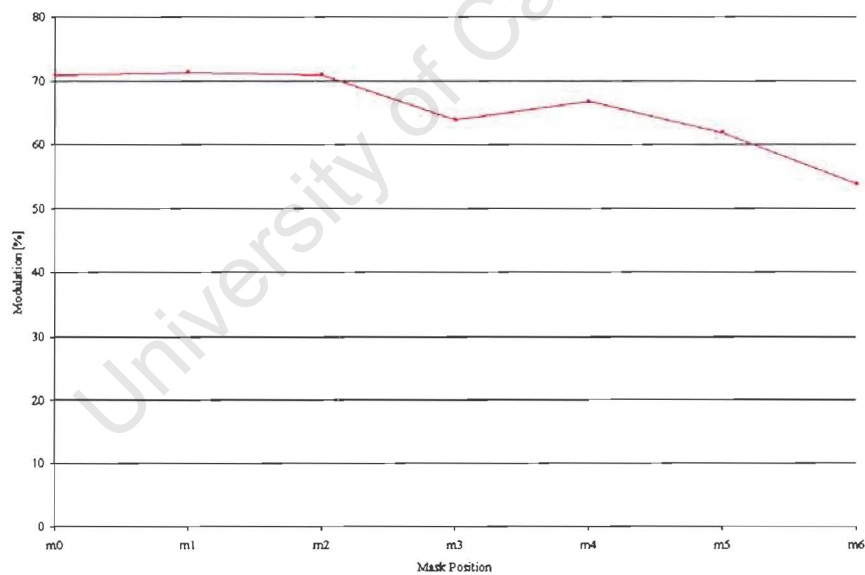


Figure 84: Set 34 modulation curve.

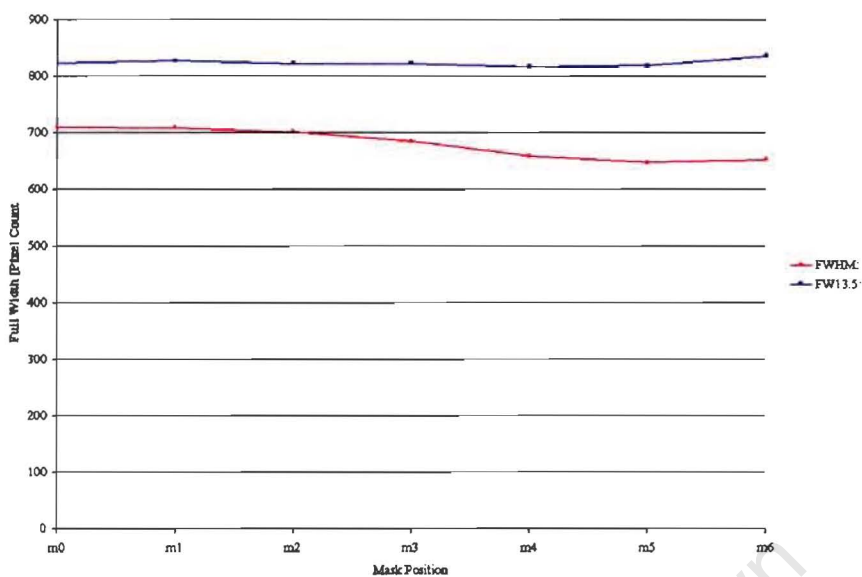


Figure 85: Set 34 full width curves.

3.3.3.5 9m 400mm fibre - no epoxy on entrance or exit face (day 16)

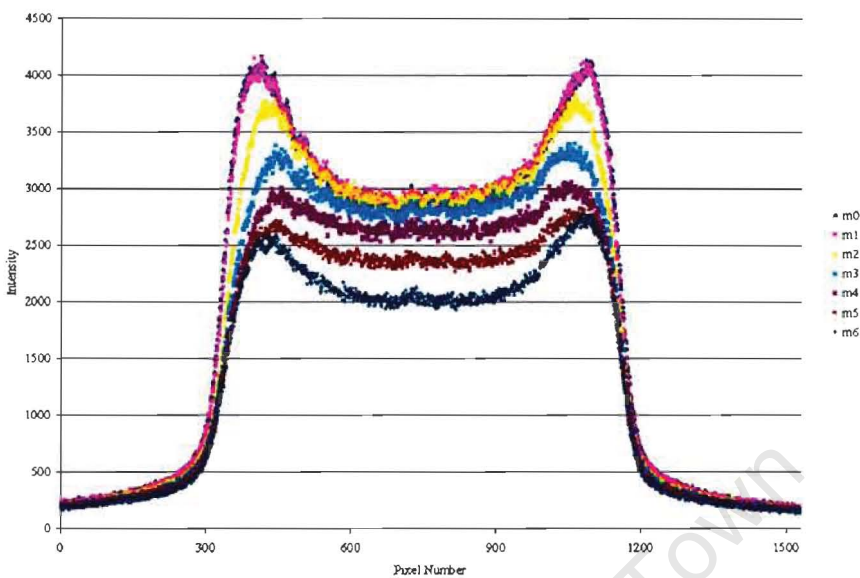


Figure 86: Set 35 overplot of cross-sections.

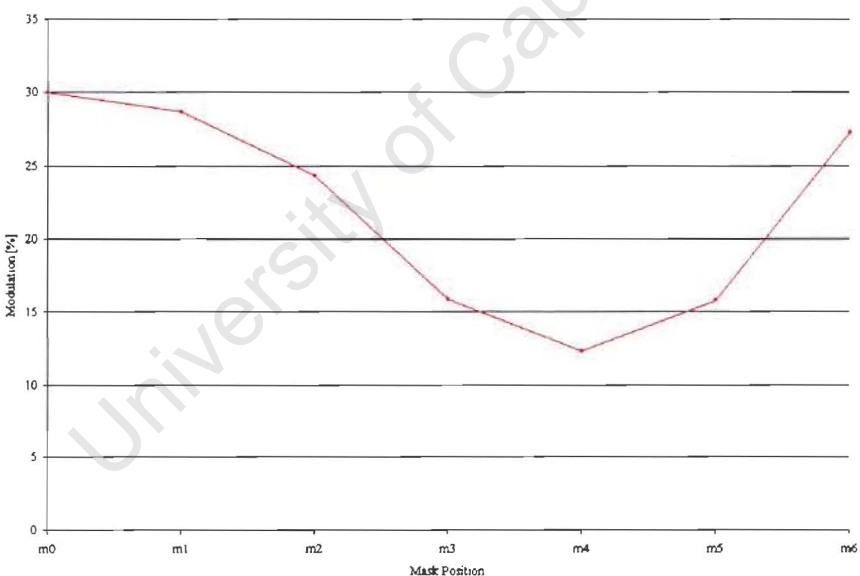


Figure 87: Set 35 modulation curve.

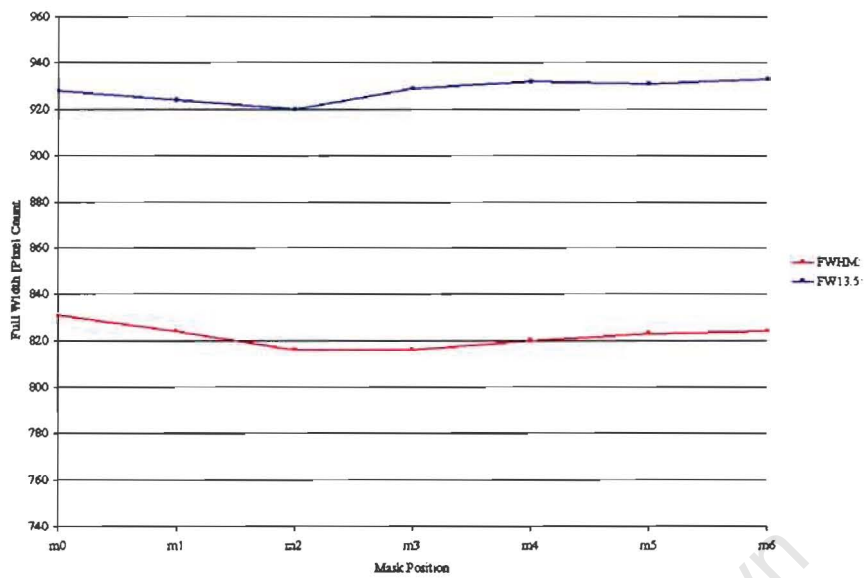


Figure 88: Set 35 full width curves.

3.3.4 Discussion

3.3.4.1 400 μ m Fibres

It appears that the modulation curve drops approximately 10% when the epoxy was dissolved off (in acetone) the exit face of the fibre optic. The bare fibre in this case was precariously held in the ferrule with masking tape. The curve then rises ~5% when the epoxy was removed from the fibre on the entrance end as well.

It is noted that there were 14 days between the first (set 31) and second (set 33) sets of data and two days between the second and third (set 35) sets. Time is mentioned since the epoxy compresses the fibre, assumingly not beyond its elastic limit, and then once it is removed there is the possibility that the fibre might creep in the absence of the applied stress (creep is a time related phenomenon) which could be reflected in the results.

If no scrambling were to occur, i.e. the input and the output profiles being constant, the modulation would be its greatest (100%) due to the central obstruction. It is strange that the results show a decreased modulation with the lack of epoxy on the exit face, as it is known that epoxy applies internal stresses to the fibre (Ramsey, 1988), increasing its ability to scramble.

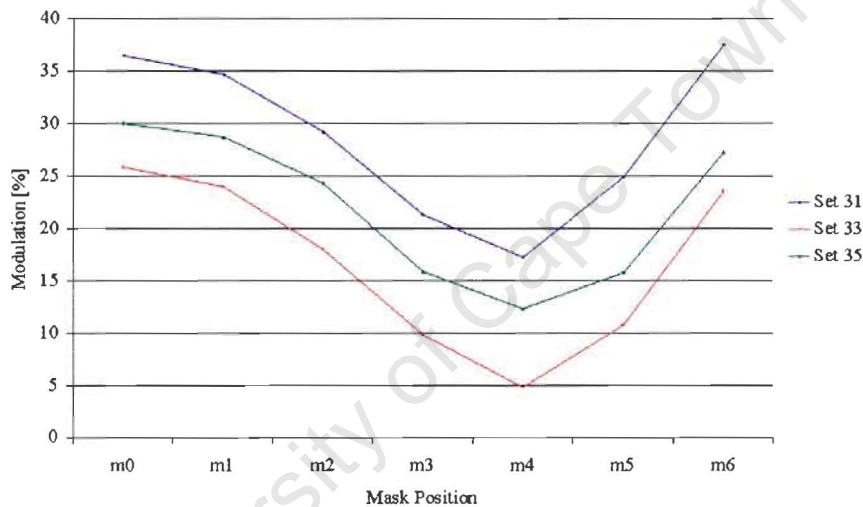


Figure 89: Modulation curves – Set 31, 33, 35.

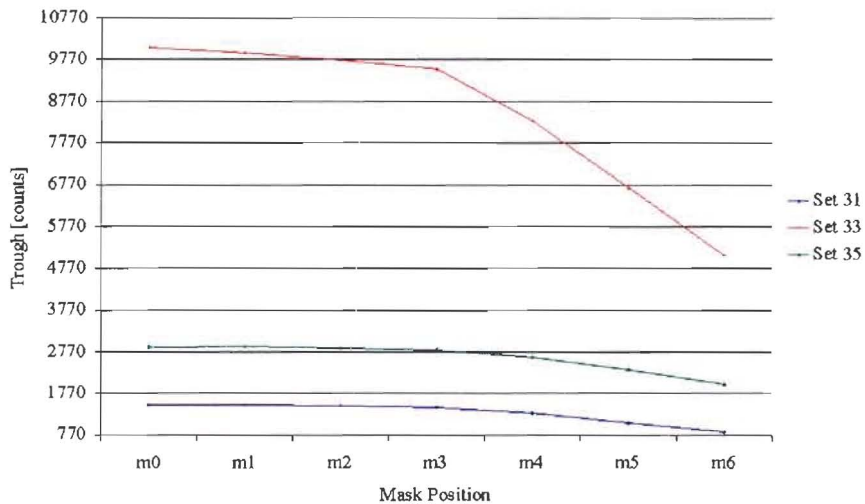


Figure 90: Trough value curves – Set 31, 33, 35.

It is seen in Figure 89, that the modulation decreases until the mask is $\sim 4^\circ$ off-axis (m4), after which it then increases. When the change in intensity at the trough position was examined, it was found to be relatively similar for the first three mask positions and then rapidly decrease to the limiting position off-axis (Figure 90). This shows that as the mask invades the beam, the amount of light in the “image wings” reduces. However, the modulation increases again in Figure 89 for mask position m5 and m6 because less light is available to be scattered into the low order modes (see Figure 61, page 58, and Figure 65, page 59).

The Full Width (FWHM & FW13.5) initially decreases with increasing displacements of the mask position and then increases for the maximum angles ($3^\circ < \theta < 6^\circ$) (Figure 91). These changes are in the order of 2 – 3% for the FWHM and 1% for FW13.5.

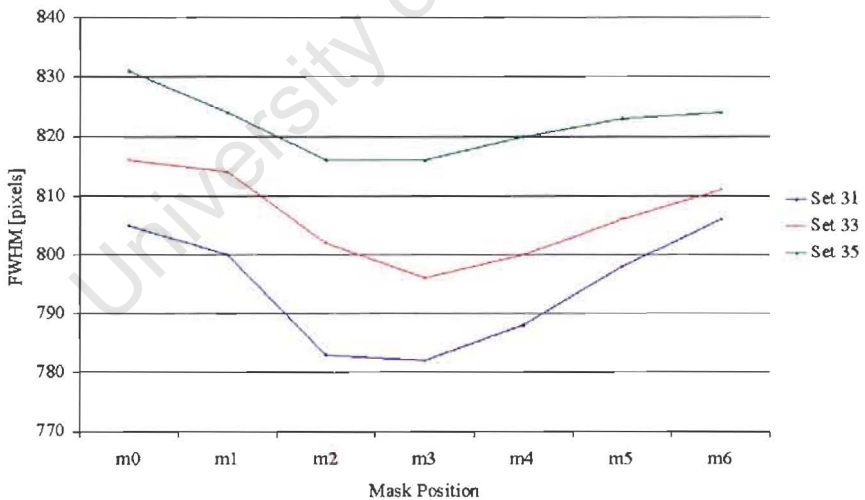


Figure 91: FWHM curves – Set 31, 33, 35.

A possible reason for the dip in the FWHM curves might be because the maximum intensity for the first few mask positions decreases with the central trough region remaining of similar intensity (i.e. the modulation reduces), the gradient decreases and this is seen in a reduced FWHM value. However, when there is not enough light to be scrambled into the central region and the modulation increases again, the profile becomes shorter and the increase in the full width is seen again.

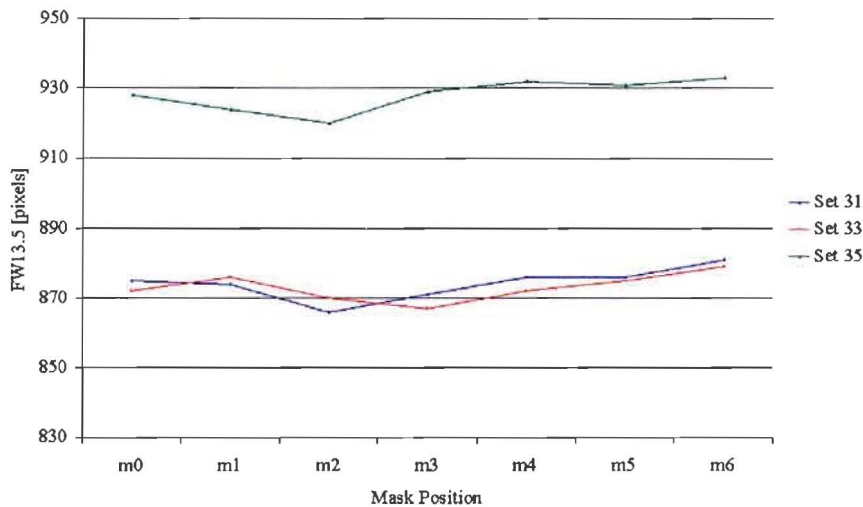


Figure 92: FW13.5 curves – Set 31, 33, 35.

The full widths at this lower intensity appear to be less sensitive than the FWHM and modulation characteristics to variations introduced by the mask.

3.3.4.2 600 μ m Fibres

For the case of the 600 μ m fibres tests, it can be seen that when the fibre end was prepared with greater precision and accuracy, less scrambling is seen (red curve in Figure 93). Therefore, it can be inferred that a more perfect fibre end face interferes less with the resulting far field pattern. This can be understood that the roughness causes more scattering of the emerging modes.

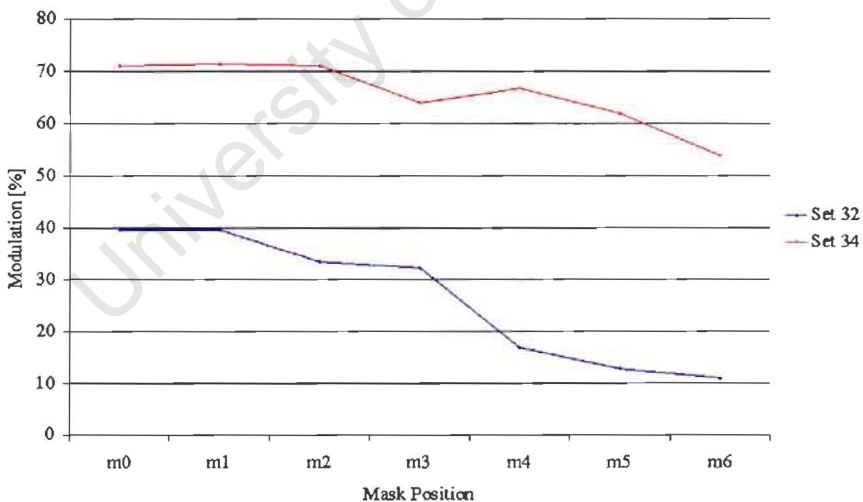


Figure 93: Modulation curves – Set 32, 34.

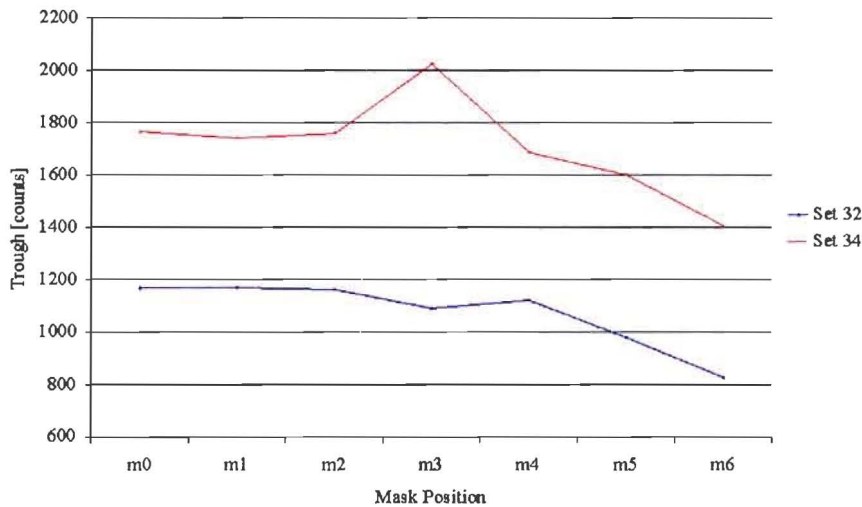


Figure 94: Trough value curves – Set 32, 34.

It is clear that the result obtained at m3 is incorrect. Otherwise, the curve follows the expected tapering off for increasing mask positions.

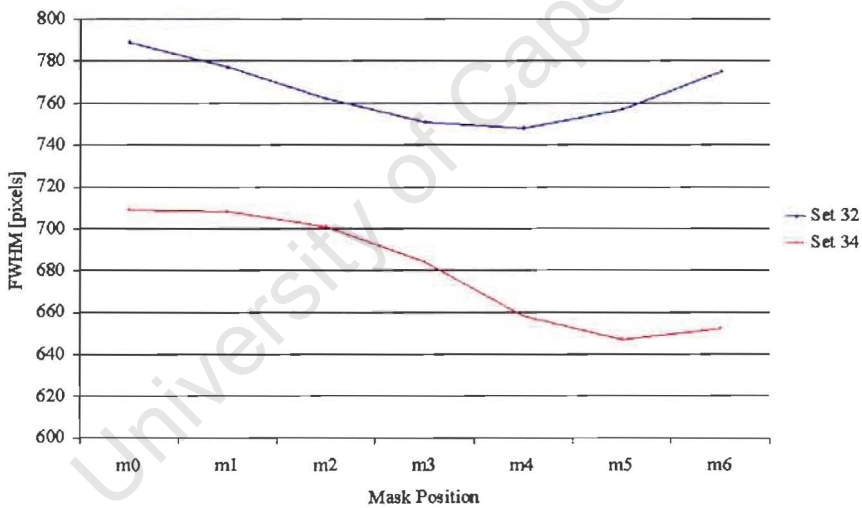


Figure 95: FWHM curves – Set 32, 34.

The dip in the pre-polished results (set 32) resembles the curves seen previously, however, the variation has increased to ~5%. The re-polished fibre seems to shift the FWHM vs. Mask Position curve to the right.

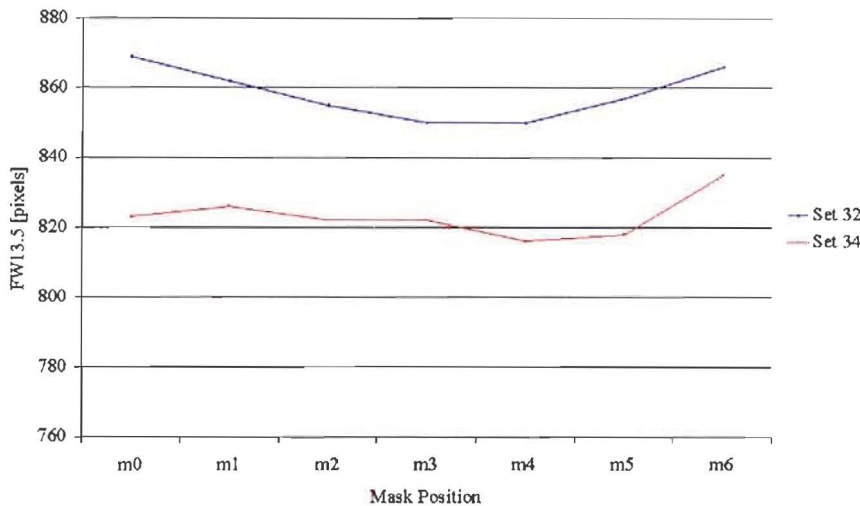


Figure 96: FW13.5 curves – Set 32, 34.

The variations in these curves are approximately 3%.

3.3.5 Conclusion and Recommendations

It can be concluded that because there appears to be variations in the output beam as the pupil migrates, a scrambler needs to be included in the optical system when high precision data is required. However, a decision needs to be made as to whether this is significant to the instrumentation suite for SALT.

It is recommended that this experiment be repeated with the specific objective to understand the processes that cause the modulation curves to shift when the epoxy is dissolved. This involves the design of a new test rig (§4: Concept Development, §4). The experiment can also be set up to study the parameters of fibre optics that are not quoted by fibre manufacturers to successfully build the SALT's Fibre Instrument Feed. These include:

- The mounting technique of the fibres on both the fibre entrance on the probe and the exit at the slit of the spectrograph.
- The two diameters of fibres to be used on the telescope (likely to be 300µm and 400µm – to be determined by the spectrograph builders) and the effect of the injected beam size on the fibre face.
- Manufacturer differences.
- Varying lengths of fibre to get a quantitative study on the effect of length on the output. The lengths of 2, 5, 30 and 40m are suggested. The distance from the HET's FIF to the spectrograph is ~33m.
- Determine the effect of temperature on the output.
- Determine the time dependence of the fibre. There are two effects: one, the curing time of the epoxy and two, the natural decay of the fibre, although this effect is hoped to be extremely small.

3.4 FOCAL RATIO DEGRADATION (FRD) ANALYSIS

Using the pupil image of the pupil simulator (pss0m0n31; Figure 41), the FWHM ($d = 808$ pixels = 7.27mm) was measured. Since the f/ratio of that beam is known ($f/4.58$), the focal distance ($f = f/\# (d) = 33.3\text{mm}$) could be calculated. The detector was then placed at that distance f (= 33.3mm) behind the output face of the fibre. This allows for radii on the image to be shown in terms of focal ratios.

A VisualBASIC program (see Appendix K, page 129 and Appendix L, page 130) was written to remove the background and sum the enclosed intensity in a given circular area, concentric with the centroid of the spot. The radius was then incrementally increased, examining larger and larger areas on the image until the radius is large enough to begin to include the background. The sum of counts in these increasing radii is plotted in Figure 97 and Figure 99. From this information, the speed of the beam and the corresponding enclosed energy, represented as a percentage, could be determined (Figure 98 and Figure 100).

For the case of the $400\mu\text{m}$ fibre in Set 31, the following enclosed energy and FRD curves are calculated.

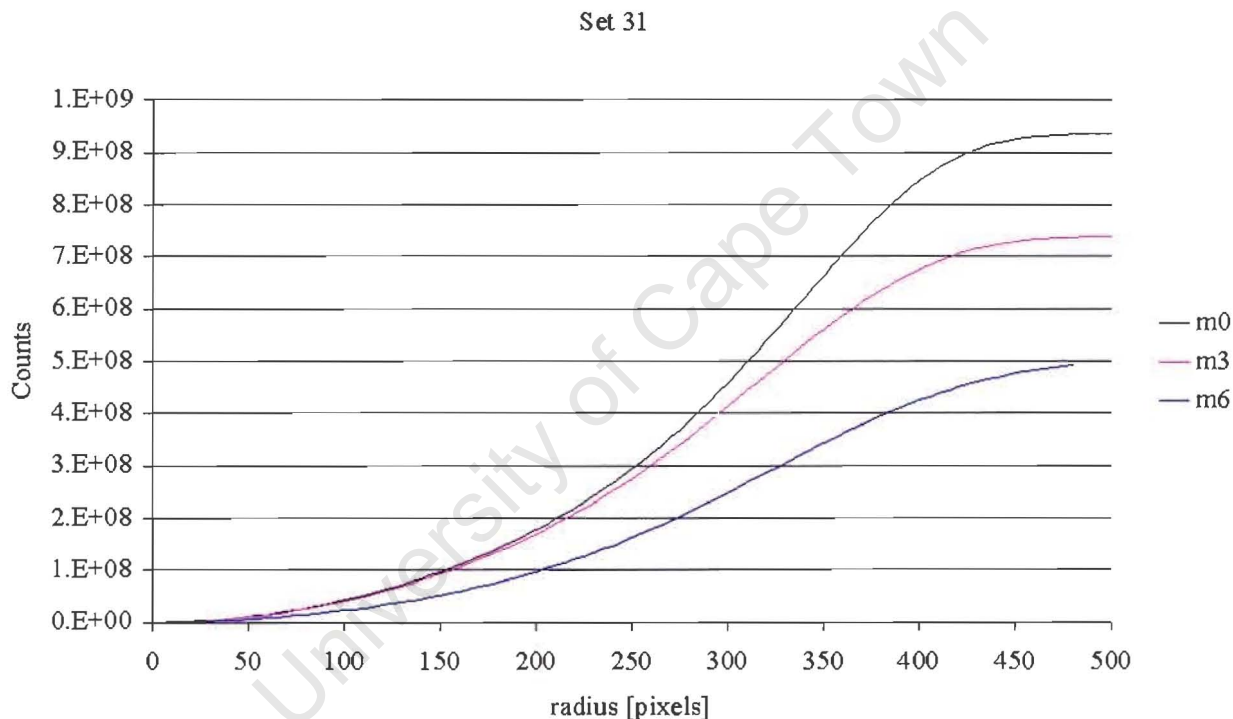


Figure 97: Set 31 ($400\mu\text{m} \times 9\text{m}$) enclosed counts vs. radius from centroid.

Set 31

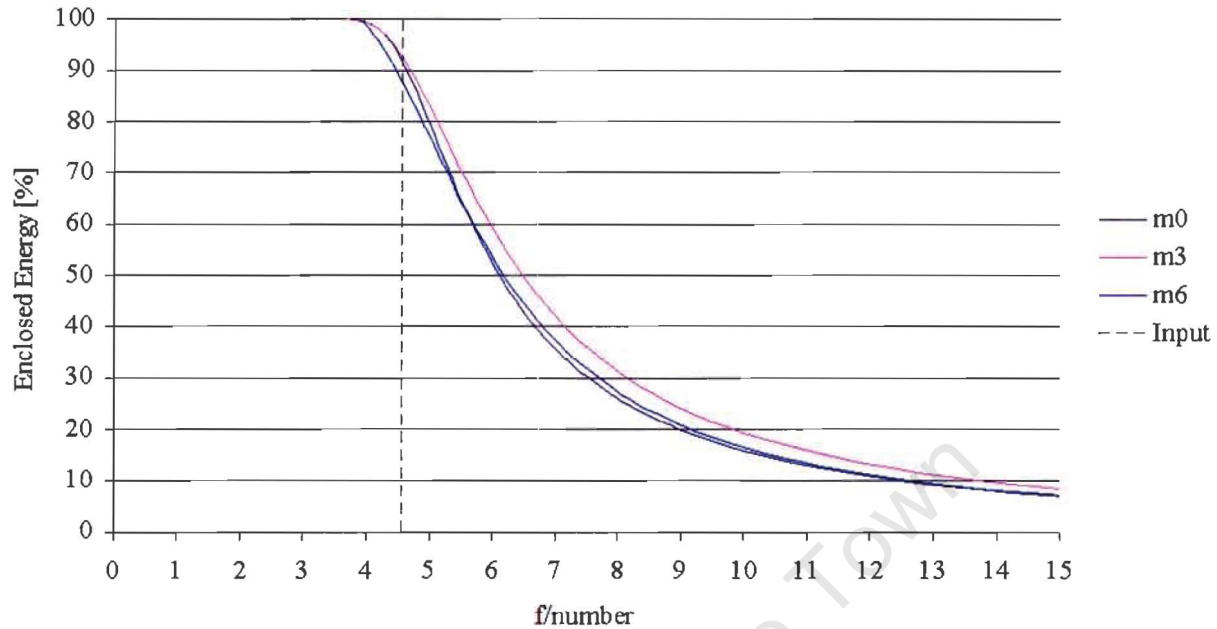


Figure 98: Set 31 (400 μm x 9m) FRD test results.

The dashed line indicates the beam speed ($f/4.58$) injected into the test fibre.

Approximately 92% of the light exiting the fibre is contained within the launched $f/\#$. Also, it may be seen that all the light is emitted slower than $\sim f/4$.

It can be seen that EE(80) varies from $f/4.8$ to $f/5.1$ and EE(50) varies from $f/6.1$ to $f/6.4$ across all mask positions.

The effects of FRD are reduced for mask position m3, this is expected since the Full Widths are reduced (see Figure 76) for this mask position.

The following enclosed energy and FRD curves are calculated for Set 34, the re-polished 600 μm fibre.

The curves show that approximately 94% of the energy is contained within the input $f/\#$, and that the deviation in output $f/\#$ at EE80 is from 5.3 to 5.4 while at EE50 it varies from 6.6 to 6.9 for the different mask positions.

Set 34

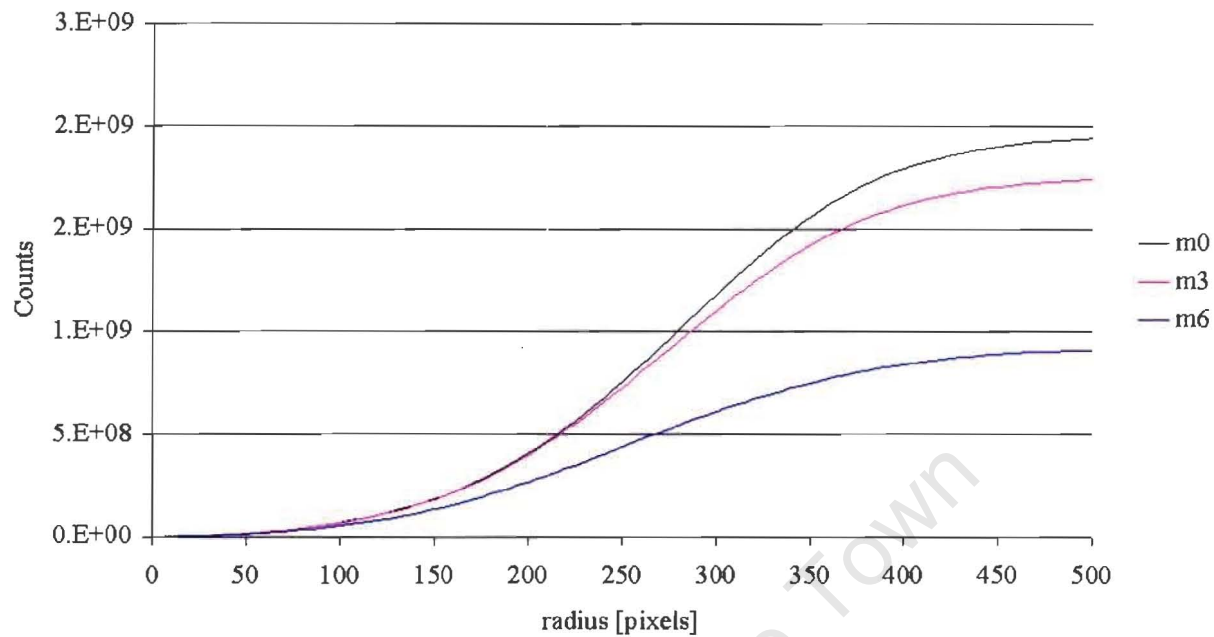


Figure 99: Set 34 ($600\mu\text{m} \times 30\text{m}$) enclosed counts vs. radius from centroid.

Set 34

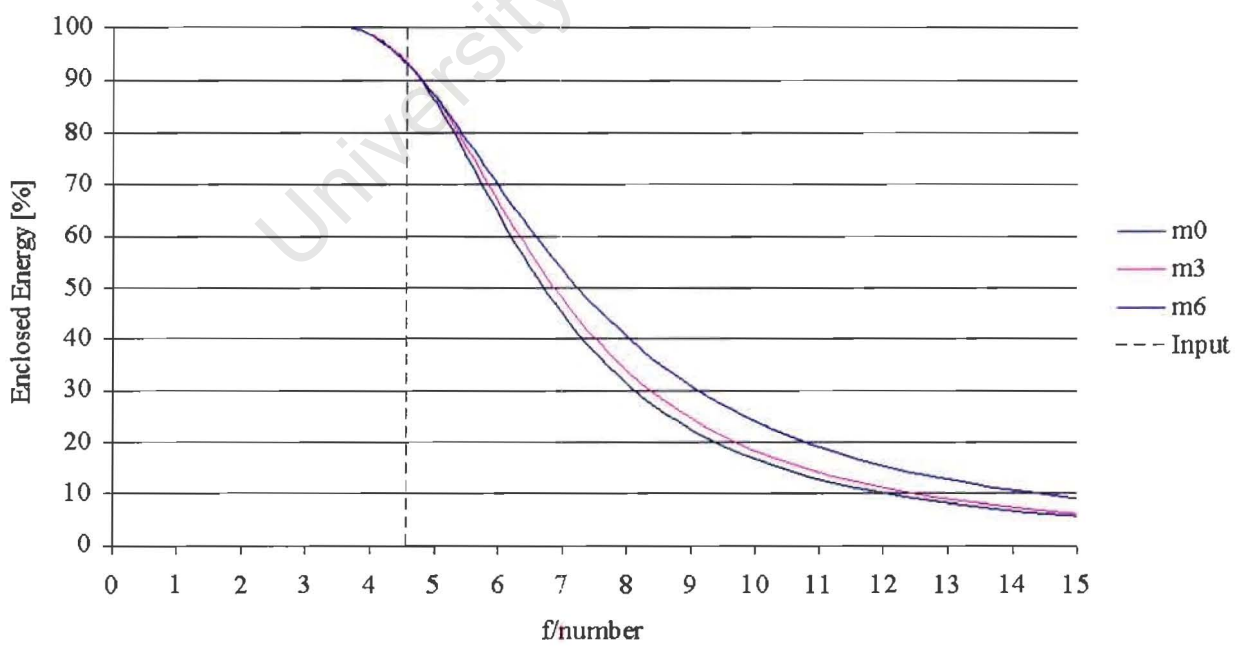


Figure 100: Set 34 ($600\mu\text{m} \times 30\text{m}$) FRD Results.

3.5 CONCLUSION

It can be seen that the migrating pupil of the HET, simulated in a test rig by moving a mask across the second mirror from 0° to 6° (see Figure 32 and Figure 33 [page 44]), causes substantial changes in the far field pattern of the output beam (Figure 89 [page 72] and Figure 91 [page 73] for the case of the 400μm fibre) and negligible changes in the near field pattern (Figure 73 [page 61]).

It is clear that the central obstruction is not completely scrambled away by the fibre, clearly seen in the doughnut structure of the output images: Figure 42, Figure 46, Figure 50, Figure 54, Figure 58, Figure 62 and Figure 66 (pp.53-59).

The first characteristic examined was the varying of the modulation. Seen together with the plot of the trough intensity vs. mask position it can be understood that the mask simply obstructs the outer beam and causes the “wings” (seen in the cross-section plots) to reduce in intensity. The modulation increases again when the mask intrudes so much of the beam that there is reduced light to be “bumped” into the centre regions.

The second characteristic examined was the full widths at two points. A suggested reason for the dip in the FWHM curves might be because the maximum intensity for the first few mask positions decreases, while the central trough region decreases less in intensity (i.e. the modulation reduces), the gradient decreases and this is seen in a reduced FWHM value. However, when there is not enough light to be scrambled into the central region and the modulation increases again, the profile becomes shorter and the increase in the full width is seen again. The FW13.5 appears to be reasonable insensitive to variations in mask positions.

The final characteristic of the fibre examined was the focal ratio degradation. The fibres exhibited good results for FRD that logically are in keeping with the poor scrambling of the central obstruction.

The removal of the epoxy on the output face shows that it influences the output results.

It is seen that the mounting technique of the fibres is important although it not fully understood.

It is clear that a greater understanding of the fibres to be used for SALT’s Fibre Instrument Feed be achieved through designed experiments that quantify the following effects for fibres from different manufacturers:

- Mounting technique.
- Effect of fibre diameter.
- Spot size on input face.
- Length.
- Temperature.
- Time dependence.

It is recognised that many researchers have undertaken similar tests in their own labs (Ramsey, Watson, Parry, Hill), which will be of relevance.

In the final analysis, the pupil simulator indicates that because of the variations in the output, effort should be undertaken to further scramble the image. Hunter & Ramsey (1992) propose a double scrambler which increases the amount of radial scrambling.

4. CONCEPT DEVELOPMENT

University of Cape Town

4.1 INTRODUCTION

This is an investigation into the Fibre Instrument Feed for the SALT – it lays the groundwork for the instrument to be built, and integrated onto the telescope. In this section, a fibre optics test rig is proposed that may be used for two purposes: one, to undertake tests on different fibre optics to obtain the most suitable supplier; and two, because of the individual nature of fibres, test each fibre to be used with the instrument. In addition, various possible positioning mechanisms are discussed that could be implemented in the design of the SALT's FIF.

4.2 PROPOSED INVESTIGATION INTO FIBRE OPTICS

Manufacturers of fibre optics will produce fibres and guarantee their attenuation properties and spectral response, but due to a fibre's individual characteristics, such as scrambling and Focal Ratio Degradation, each fibre needs to be tested individually.

From the results in the previous section (§3), it is clear that before a Fibre Instrument Feed can be built for SALT, the losses due to fibre end preparation, mounting technique and length need to be characterised. These effects should also be characterised for fibre diameter and fibre manufacturer, and attention should be paid to the time and the temperature of the results.

One objective is to build a rig (Figure 101) to test for FRD and scrambling effects, first for the most suitable manufacturer of fibre optics for the SALT and then to test the individual fibres to be used on the instrument.

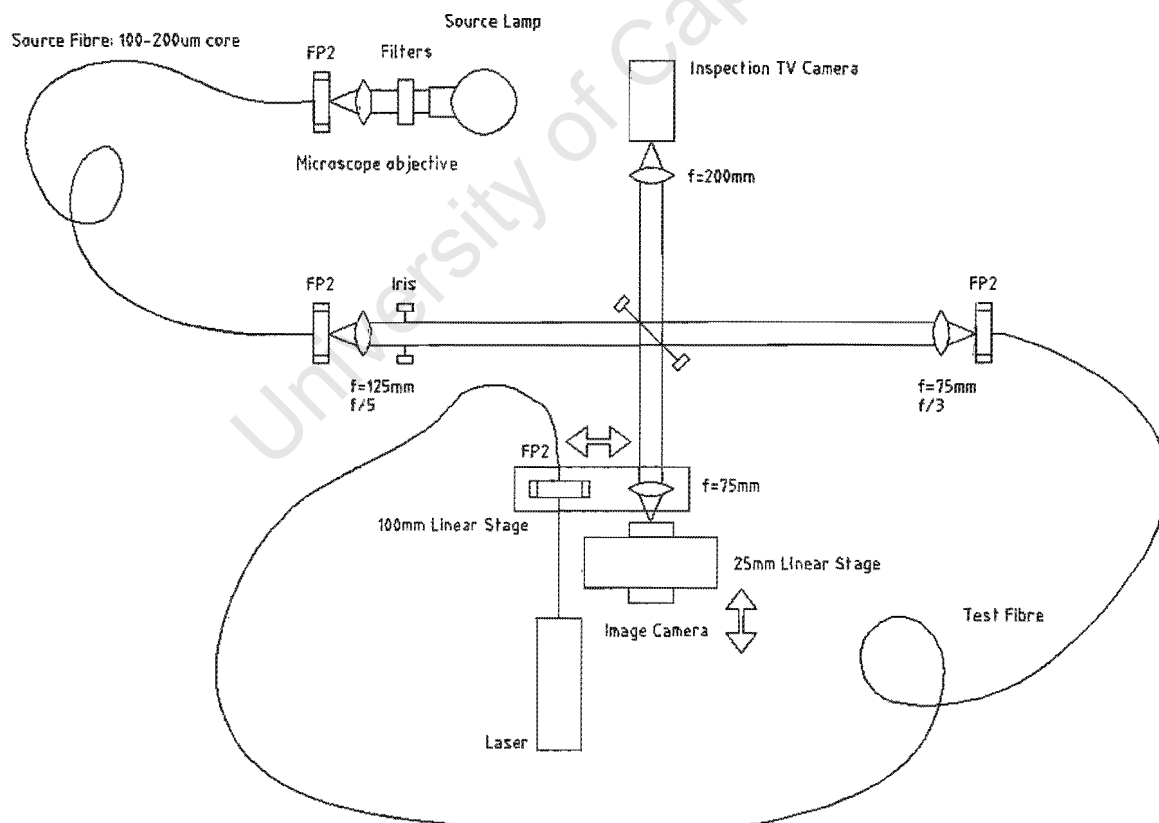


Figure 101: Proposed FRD test rig.

A small diameter (100-200 μm) source fibre is used to destroy the lamp structure by scrambling. An alternative would be to place the lamp behind a diffuser, microscope objective and a pinhole. The light is collimated by a lens with a focal length of 125mm. The iris placed after the lens has a diameter of 25mm, this leads to the test rig accepting light slower than $f/5$ from the source fibre. Because the source fibre emits a beam with a profile that is not a step function, the slower f/ratios corresponding to the top of the profile will be injected into the test fibre. The collimated beam diameter can be controlled by the iris diameter which in turn controls the f/ratio to be injected into the test fibre by the second lens. This lens is reasonably fast to test over the range of input f/ratios slower than $f/3$. Between the iris and the second lens is a pellicle beamsplitter, which serves several functions.

- Firstly, it provides a means to measure the iris diameter accurately by allowing an image of the pupil to be taken (by defocusing the image camera).
- This same image can be used to record the injected beam intensity profile to be compared with the exit beam from the test fibre to obtain the optical transfer function of the fibre.
- Thirdly, an image of the input beam can be used to measure the throughput of the fibre (knowing the transmitted-reflective fraction of the beamsplitter).
- Fourthly, it allows the inspection of the concentricity of injected beam on the input face of the test fibre. The lens used to image the test fibre input face has a focal length of 200mm, which magnifies the image 2.67 times so that a 600 μm fibre forms an image 1.6mm in diameter. This easily fits on the CCD chip of a small high resolution TV camera.

The setup also conveniently allows the use of a backlighting laser, so that alignment of the two fibres can be easily completed. Finally, the far field image is obtained by moving the translation stage so that the test fibre illuminates the CCD chip on the image camera. This setup allows for varying lengths of fibres and mounting techniques by changing the test fibre.

4.3 THE SALT'S TELECENTRIC ANGLE PROBLEM

The SAC design for the SALT has a field of view twice that of the HET, yielding a field 8 arc-minutes and ~100mm in diameter, the corresponding telecentric angle variation in this case is $\sim 4.6^\circ$, as shown in Figure 102.

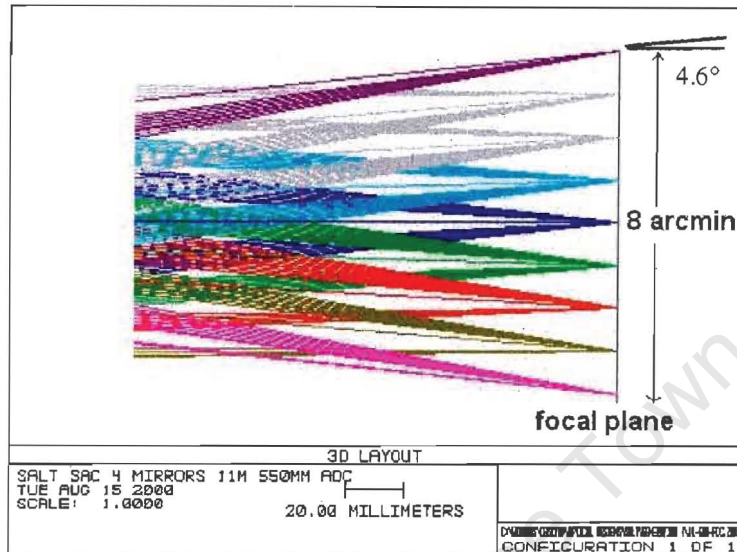


Figure 102: ZEMAX ray-trace (courtesy of D. O'Donoghue) showing the telecentric angle variation in the SALT's uncorrected field of view (Buckley & Sessions, 2000).

However, it is possible to place a doublet before the image plane in order to correct for the telecentric angle variation. This removes the telecentricity, but adds field curvature, as shown in Figure 103. The deviation, in this case, of the focal surface from a plane amounts to $\sim 3\text{mm}$ (called sagitta or sag).

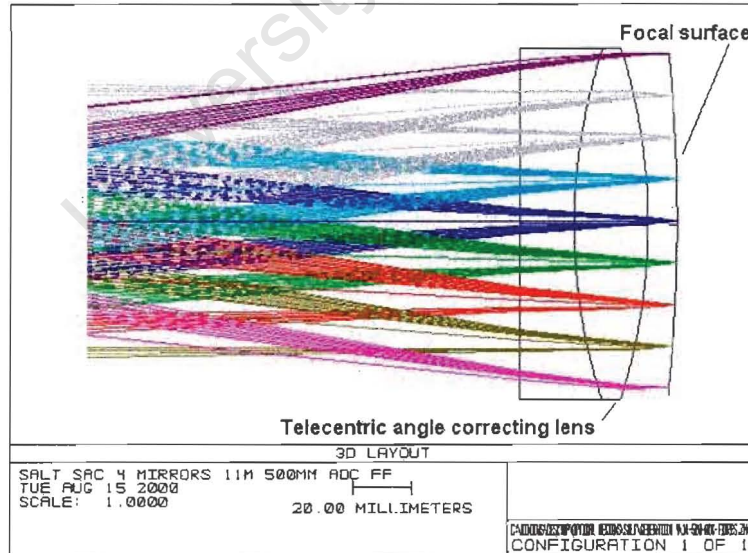


Figure 103: ZEMAX ray-trace (courtesy of D. O'Donoghue) showing the telecentric angle variation removed in the SALT's corrected field of view with a doublet (Buckley & Sessions, 2000).

The first option would require a positioner to align the fibres with the increased telecentric angle variation (i.e. in X,Y, θ and ϕ) and the second, although the telecentric angle is removed, requires a positioner to move in X,Y and Z. Following is an examination of both field configurations with possible mechanisms and schemes to position the fibres proposed.

4.4 CONCEPTS FOR THE UNCORRECTED FOCAL PLANE

4.4.1 Analysis of the HET's Field

The telecentric angle uncorrected field configuration for SALT, is an enlarged version of the HET's field. The following is an analysis of the HET's field; although the numbers are different, the concept (and conclusions) can be applied to SALT.

The HET's telecentric angle variation has been called the "Telecentric Angle Problem". To guarantee maximum light admittance to the fibre optic, the probes must be positioned to within $10\mu\text{m}$ in the focal plane. Ideally, the probes should be tilted to within 0.15° (corresponding to $\leq 5\%$ loss in light) of the principle ray to ensure minimal disturbance in the speed of the exit beam (Buckley, 2000; Sessions, 2000). Without a mechanism to tilt the fibre to match the principle ray of the admitted light bundle, the telescope's effective f -ratio of $f/4.6$ will increase to $f/3.7$ because of the azimuthal scrambling (refer §2.3.4) combining the nominal beam angle and the telecentric angle. The increase means that the objects in the outer regions of the field will overfill the collimator if it is matched to the exit speed for those in the central regions. The HET's solution to this problem is to use a method of "zoning" whereby two of the ten probes are mounted exactly perpendicularly to the focal plane (Type 0 Probes), and used only in the inner regions. The remaining eight probes (Type 1 Probes) are set at an angle of 1° and are deployed in the outer regions. The spectrograph is then designed to a compromise f -ratio of $f/4.2$. The losses associated with each probe are shown in graphical form in Figure 104 and Figure 105 (Horner, 1998).

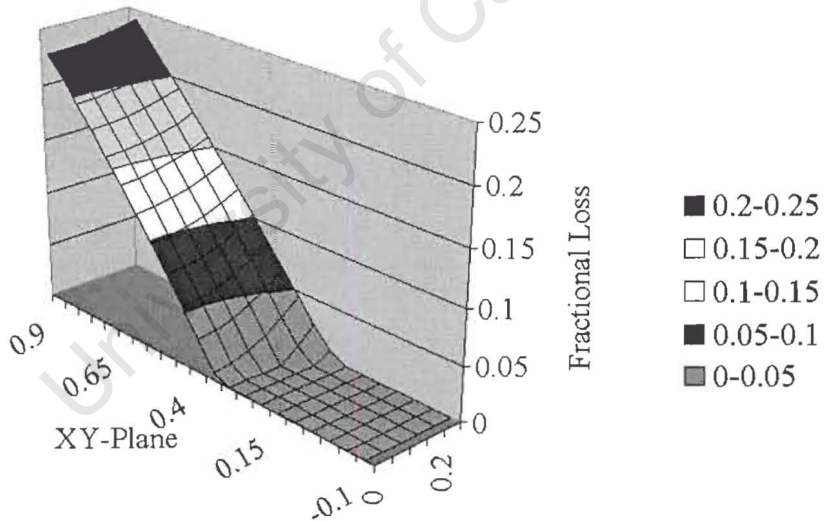


Figure 104: Type 0 MOS probes. The XY plane (units in inches) represents the area that the probe covers in the focal plane (Figure 26),. X is the longer axis, which extends beyond the centre of the field. The Y axis only represents half the mapped out area (because of symmetry). The vertical axis represents the fractional loss of light, which increases as the probe moves outside its zoned limit.

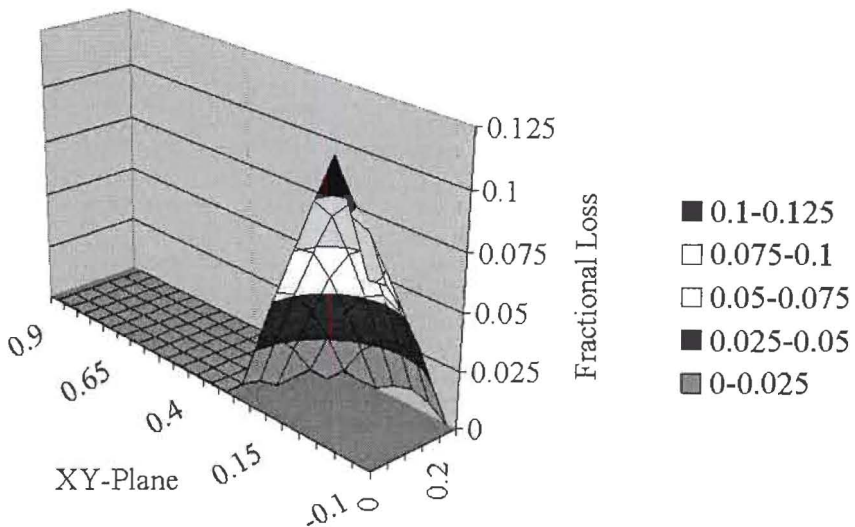


Figure 105: Similar to Figure 104, for Type 1 MOS probes. Showing light loss in the central regions by the probes.

To verify the angle that the HET used on the Type 1 probes, the following coordinate system was defined (Figure 106).

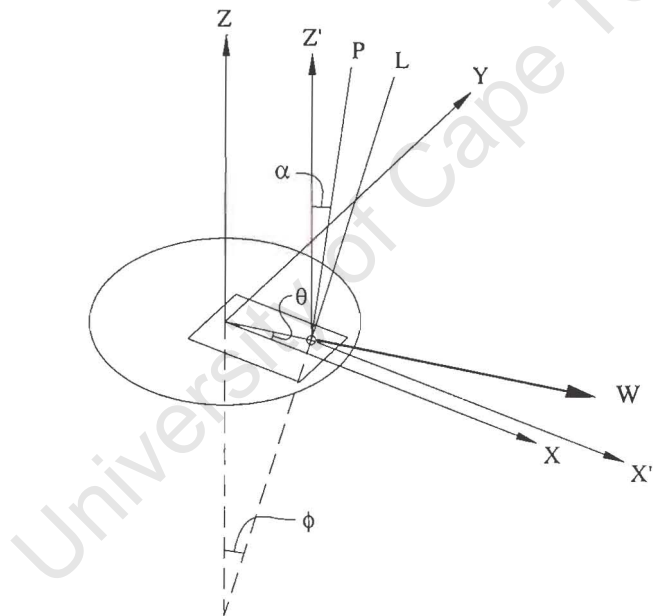


Figure 106: Coordinate system defined to verify angle on Type 1 probes.

The origin of the XY plane coincides with the centre of the focal plane. The origin of the X'Z' plane is the location of the probe end in the focal plane. The vector **P** represents the probe, to which the fibre is attached, and **L** the principal ray of the light beam. Alpha (α) is defined as the probe's tilt in the X'Z' plane, measured from the vertical.

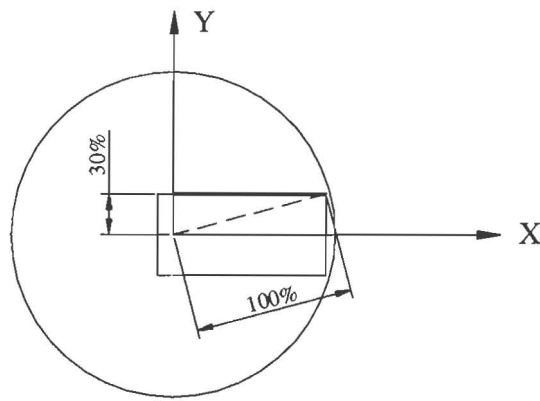


Figure 107: Line of analysis shown by bold line starting at a radius of 30% on the Y Axis to the full radius of 100% along the hypotenuse of the area mapped out by the linear translation stages.

The angle between the probe (**P**) and the chief ray (**L**) is calculated for the positions along the limit of the probe's allowable area, as shown in Figure 107 by the darkened line, where the angles are the greatest. The probe in this case, is constrained to lie in the $X'Y'$ plane; the following graph is then obtained for five cases of α :

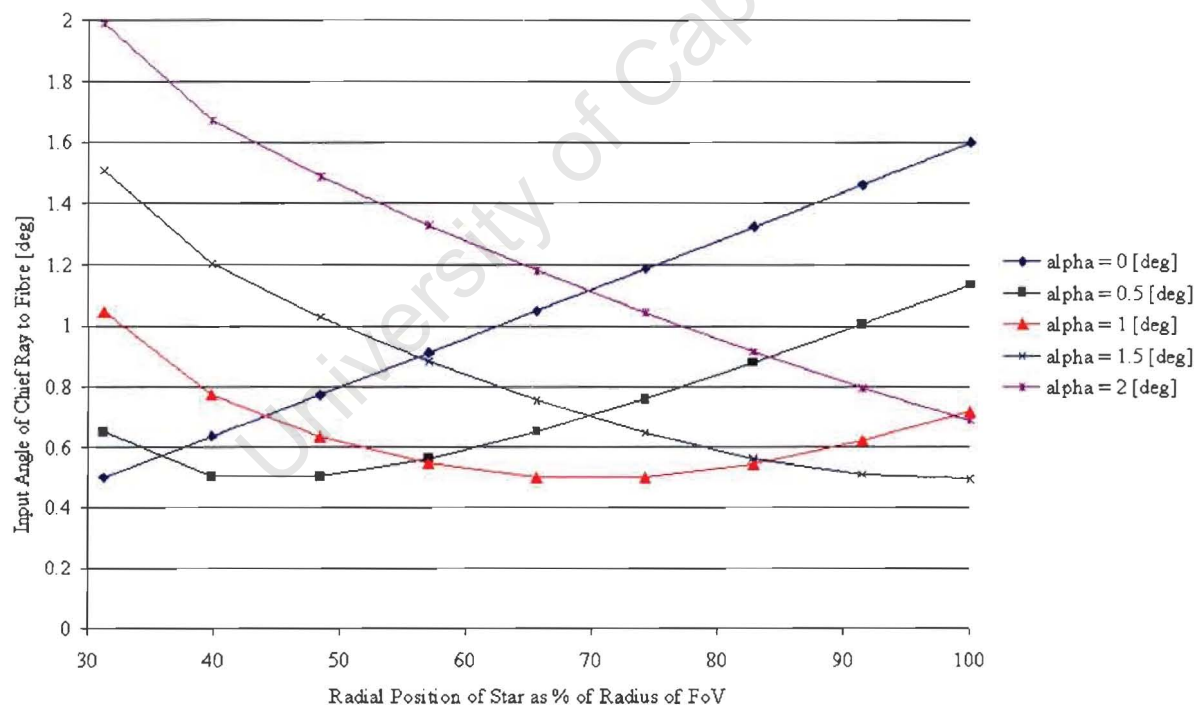


Figure 108: Probe optimised to 1 degree.

It can be seen that the tilt angle $\alpha = 1^\circ$ (shown in the red curve in Figure 108), forms the smallest angle between the probe and the light, across the field. The results are thus in agreement with the decision to mount the probes at 1° for use in the outer regions of the field (Horner, et al, 1997).

A double integral can be set up using a similar analysis to cover the area that the probe maps out in the focal plane. This can be used to quantify the angle between the probe and the principal ray for different orientations of the probe. Two degrees of freedom are required to perfectly align the probe with the principal ray for all (allowable) X and Y. As expected, this adds complexity to the mechanism and the control system (the exact reason for which the HET used the method of zoning). If only one degree of freedom is added (to simplify), the analysis points to, quantitatively, which degree of freedom should be added. Four cases are therefore set up:

- Case 1. Probe tilted (1°) and in a plane collinear with the axis in Figure 107.
- Case 2. Probe tilted (1°) with a variable angle allowing it to point along a radial vector.
- Case 3. Probe with variable tilt & in line with X-Y stage.
- Case 4. Probe with variable tilt and angle, allowing alignment with the chief ray.

Case 1 corresponds to the solution adopted by the HET, its number is used as the reference value. Case 4, by definition, the integral should equal zero.

Using the integral:

$$\xi = \int_{y_1}^{y_2} \int_{x_1}^{x_2} \arccos \left(\bar{L} \cdot \bar{P} \right) dx dy$$

where,

$$\bar{L} = \begin{pmatrix} \rho \cos \theta \sin \phi \\ \rho \sin \theta \sin \phi \\ \rho \cos \phi \end{pmatrix}, \text{ and } \bar{P} = \begin{pmatrix} \rho \cos \beta \sin \alpha \\ \rho \sin \beta \sin \alpha \\ \rho \cos \alpha \end{pmatrix}$$

β is not shown in Figure 106 but is angle between the X axis and the projection of \mathbf{P} onto the XY plane.

$$\theta = \arctan \left(\frac{\sqrt{x^2 + y^2}}{H} \right), \quad \theta = \arctan \left(\frac{y}{x} \right)$$

$$x_1 = 0; x_2 = \frac{1}{2}(12.7) = 6.35; y_1 = 0; y_2 = 22.9; \rho = 1; H = 872.27 \text{ mm}$$

where ξ is the integral of the angles between the chief ray and the probe (also the axis of the fibre optic) over the area mapped out by the probe. It should be noted that due to the way the integral has been set up, the upper and lower limits of the integral are defined by the limits of the X-Y translation stage. H is the exit pupil distance, it is from this value that the telecentric variation value of $\sim 1.6^\circ$ is calculated.

Now the cases reduce to:

- Case 1. $\alpha = 1^\circ; \beta = 0^\circ$
- Case 2. $\alpha = 1^\circ; \beta = \theta$
- Case 3. $\alpha = \arctan(\cos \theta \tan \phi); \beta = 0^\circ$
- Case 4. $\alpha = \phi; \beta = \theta$

The plots of the functions being integrated over are shown in Figure 109 (case 1), Figure 110 (case 2), and Figure 111 (case 3).

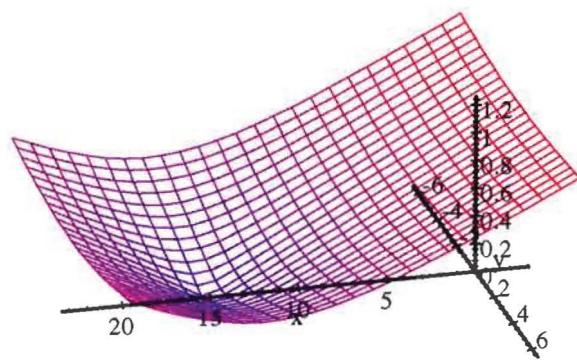


Figure 109: Plot of $\arccos(\bar{L} \cdot \bar{P})$ – Case 1

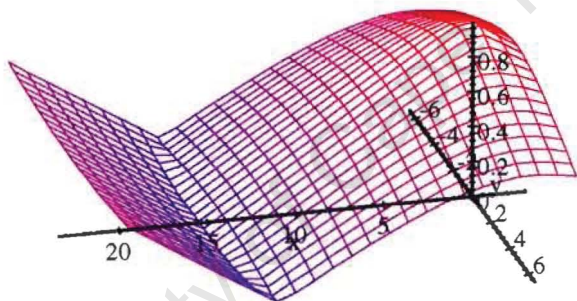


Figure 110: Plot of $\arccos(\bar{L} \cdot \bar{P})$ – Case 2

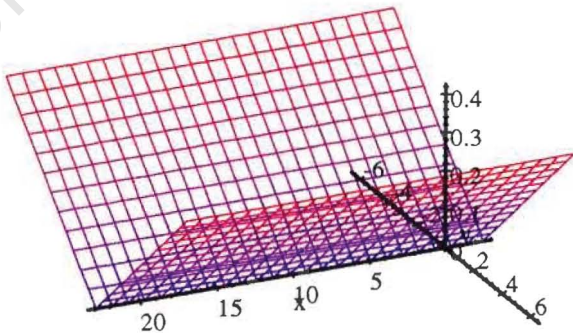


Figure 111: Plot of $\arccos(\bar{L} \cdot \bar{P})$ – Case 3

The analysis leads to the following results:

- Case 1. $\xi = 72.31$
- Case 2. $\xi = 55.12$
- Case 3. $\xi = 30.29$
- Case 4. $\xi = 0$

This means that for a mechanism that can point the fibre towards the optical axis, i.e. the tilt is confined to the WZ plane (Case 2), this will result in an improvement of 24% with respect to light loss compared to the current zoning method (Case 1 where the tilting is constrained to the X'Z' plane) and if the only degree of freedom added, was the tilt parameter, then there would be an improvement of 58%.

4.4.2 Possible Manipulating Elements

The following possible manipulating elements are in addition to the X-Y translation stages used in the HET design. It is noted that to provide angular adjustment to the probe, to align the fibre optic with the chief ray, the probe needs to be orientated so that it points to the interception of the exit pupil and the optical axis. For the angular adjustment addition to the HET scheme, this means that two degrees of freedom need to be added to the system: the first must tilt the fibre to the telecentric angle of the corresponding field position and another must angle the probe along a radial vector.

4.4.2.1 Nanomotors®:

It is possible to consider the actuation element proposed for use in the *ECHIDNA* (Gillingham, et al, 2000). The Nanomotor® (manufactured by Nanotechnik) is a small motor that uses piezoelectric crystal technology. It thus has the resolution at the atomic scale (sub-nanometre) and overcomes the limited stroke of a few microns, typical of other piezoelectric actuators. A linear table can be constructed from these actuators and is shown in Figure 112.

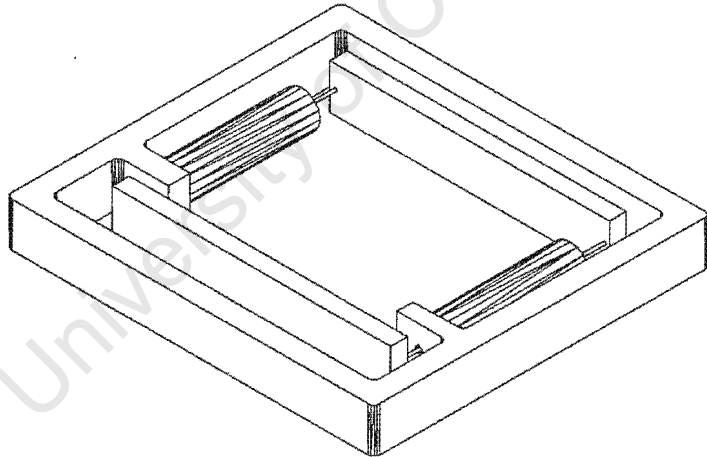


Figure 112: Nanomotor® linear table.

The advantage of such a positioning element is its compact size, while its disadvantage is a limited stroke of 10mm (where ~50mm is required for SALT), they therefore could not replace the *NEWPORT* linear translation stages.

Another configuration of Nanomotors® could be to arrange three motors in a triplet (see Figure 113) to achieve both the tip and tilt adjustments of the probe carrying the fibres. These could be mounted on X-Y linear translation stages.

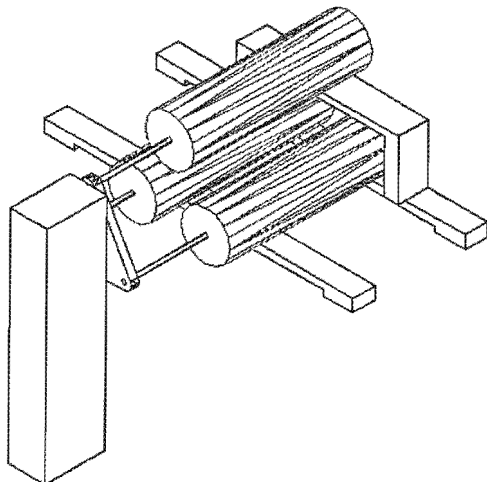


Figure 113: Nanomotor® arrangement into a triplet to provide tip and tilt of the probe.

The advantage is again that the motors are small and compact (6.35mm in diameter), however, the small force of these motors (~1N) is a disadvantage (Kleindiek, 2000).

4.4.2.2 *Shape Memory Alloys*

Materials that display properties of changing shape with temperature are called shape memory alloys. Deformed plastically when cold, they recover their original shape when heated above their transition temperature which causes a phase change. Because the transition temperature occurs over a range rather than at a defined temperature, shape memory alloys can be used in precise actuation (Hodgson, 1999). Copper based alloys and nickel titanium (Nitinol) are the most common types of shape memory alloys (TiNi Alloy Company, 2000; Shape Memory Applications, 1999). Wire which is drawn from this material, called “muscle wire”, contracts when it is heated, or has a current passed through it, and could be used in a fibre manipulating scheme, as shown in Figure 114. The weight of the probe is supported at the joint. Manoeuvring of the probe is achieved by contracting the top wires and relaxing the bottom wires to tilt the fibre. To tip the probe, there must be different forces on the horizontally displaced wires. There are two importance issues to be considered in such a design, namely: control and heat dissipation.

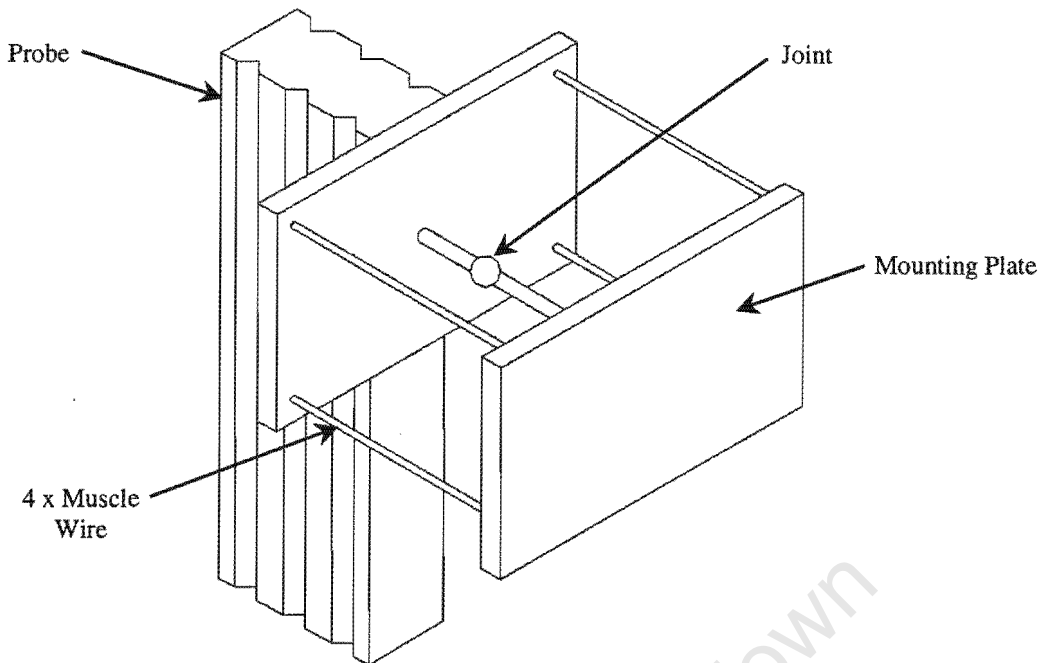


Figure 114: Scheme to manipulate fibres using “muscle wire”.

4.4.2.3 Piezoelectric Benders

These are a form of piezoelectric crystals called Ceramic Multilayer Benders (CMB) which are built up from thin layers of lead zirconate titanate (PZT) based ceramic materials (Ferroperm, 2001; Physik Instrumente, 2001). The fibre optics could be mounted to the bender and a voltage applied to attain the correct angle corresponding to the fibre position in the field of view (see Figure 115).

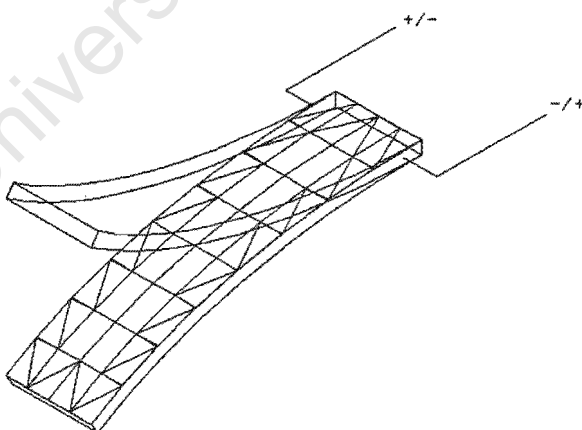


Figure 115: Piezoelectric bender.

Standard beam theory can be used to calculate forces required to tilt the fibres:

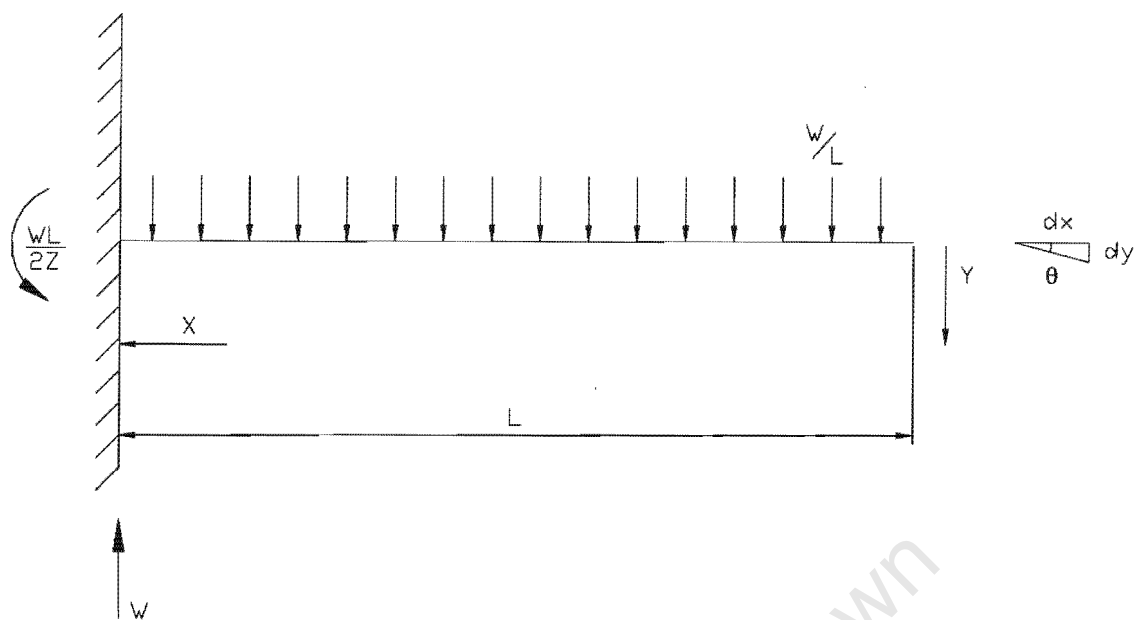


Figure 116: Force diagram for uniformly loaded beam. W = Total Load, Z = Section modulus of cross-section.

The deflection at a point is given as:

$$y = \frac{Wx^2}{24EI} [2L^2 + (2L - x)^2] \quad (\text{Green, 1992})$$

where $I = \frac{\pi}{64}d^4$ is the moment of inertia for a circular cross-section and E = Young's modulus; L = length and W = total load.

Then:

$$\theta = \frac{dy}{dx}$$

and

$$\frac{dy}{dx} = \frac{Wx}{6EI} (3L^2 - 3Lx + x^2)$$

at the end, $x = L$

$$\Rightarrow \theta = \frac{WL^2}{6EI}$$

so

$$\Rightarrow W = \frac{6EI\theta}{L^2}$$

if the following is assumed: L = 100mm, E = 48-83 Gpa for glass and the fibre diameter is in the range: 500 μm – 1200 μm , then:

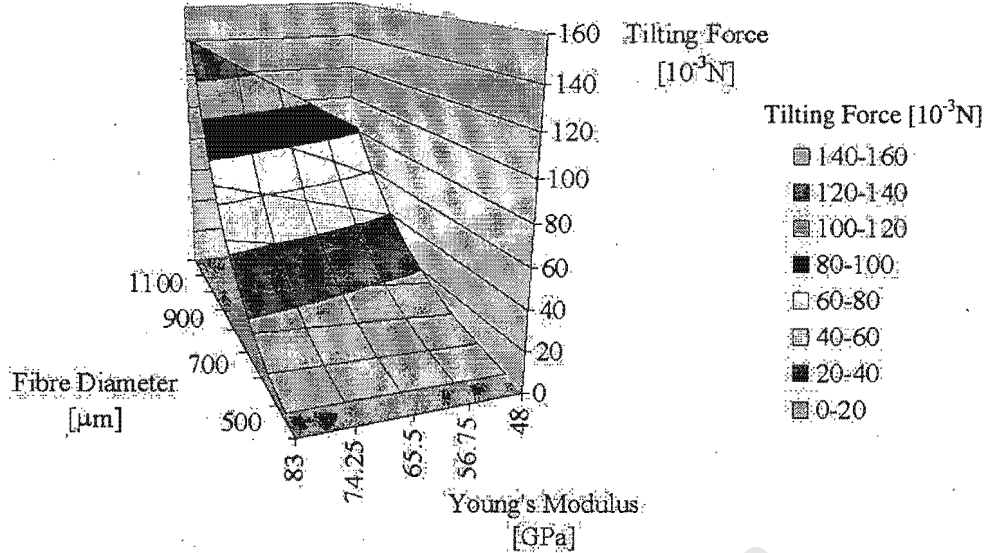


Figure 117: Tilting force required to bend fibre.

Figure 117 plots the change in force required to tilt the fibre, were the fibre to lie along the piezoelectric bender, for varying young's modulus and fibre diameter. It is recognised that the limits of this analysis is on the performance of the bender.

4.4.3 Concept Schemes

4.4.3.1 Concept One: Goniometric Cradles

NEWPORT Goniometric Cradles could be used to “rock” the probe carrying the fibres about the centre of the focal plane (Figure 118). The scheme has a linear stage mounted in the radial dimension to allow an individual probe access to a sector of the field of view. A tilting mechanism, such as the piezoelectric bender discussed above, is required but not shown in the figure.

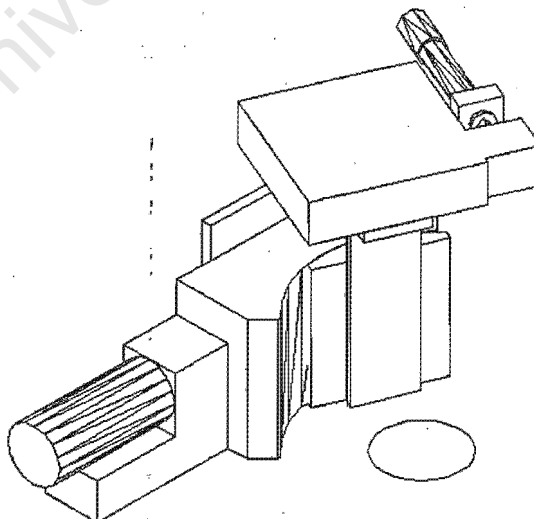


Figure 118: Goniometric cradle.

The advantage of such a scheme is that it simplifies the tilting of the fibres, since only one tilt angle is required as the fibre is always on a radial vector. The disadvantage is its height, since it is more than 150mm high and because only two could be accommodated on a level, the entire unit would exceed 750mm. This poses two problems, the length of the probes makes it susceptible to flexure and that an instrument of those dimensions cannot be accommodated on the Tracker.

4.4.3.2 *Concept Two: Cross mounted translations stages mounted on a tip-tilt stage.*

It is possible to mount two translation stages at 90° to each other on top of a tip-tilt platform as shown in Figure 119. The disadvantage of such a system is the volume required to populate an instrument with more than two modules. The tip-tilt platforms are manufactured by *NEWPORT* and provide ~5° angular adjustment along both axes.

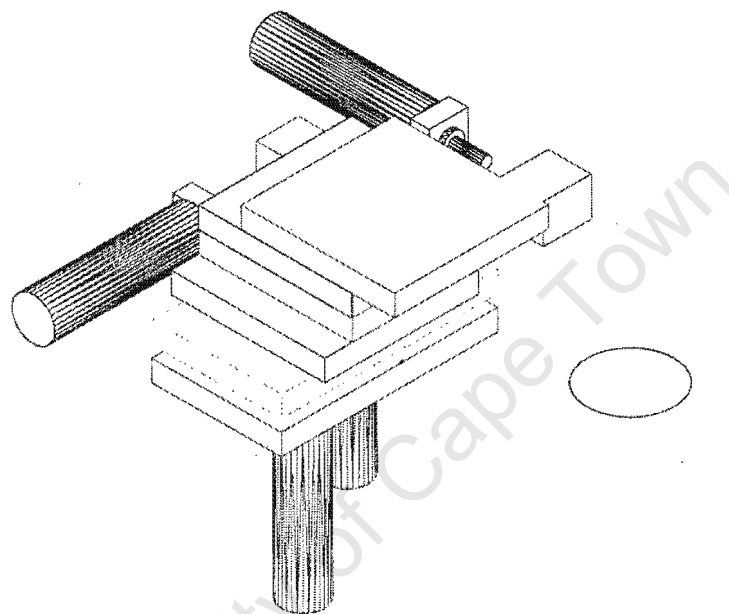


Figure 119: Tip Tilt Scheme.

4.5 CONCEPTS FOR THE TELECENTRIC CORRECTED FOCAL SURFACE

The telecentric angle corrected field, achieved with the doublet, has a curved focal surface with a sag of ~3mm. Because the telecentric angle is zero, the mechanism to position the fibres in the SALT's field of view is restricted to the X, Y and Z motions.

4.5.1 Concept One: Three Axis Modules

A possible solution to manipulate an object in X, Y and Z is to use linear translation stages mounted orthogonal to each other. All components are proprietary items so the design would be simple and cost effective. Using the following *NEWPORT* components:

1. 2 x M-436-A (Low Profile Crossed-Roller Bearing Translation Stage, metric, 50mm stroke, with aperture).
2. 1 x 360-90 (90° Angle Bracket).
3. 1 x M-426-A (Low Profile Crossed-Roller Bearing Translation Stage, metric, 25mm stroke, with aperture).
4. 3 x 850G closed loop precision actuators.

The following positioning module (Figure 120) can be imagined.

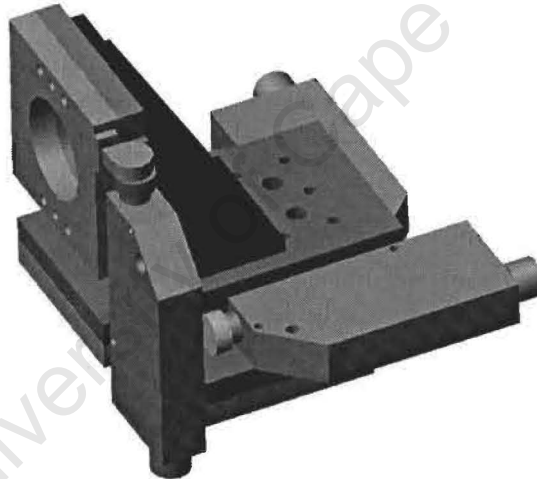


Figure 120: Three axis manipulator.

Ten modules could be arranged around the field in the following way:

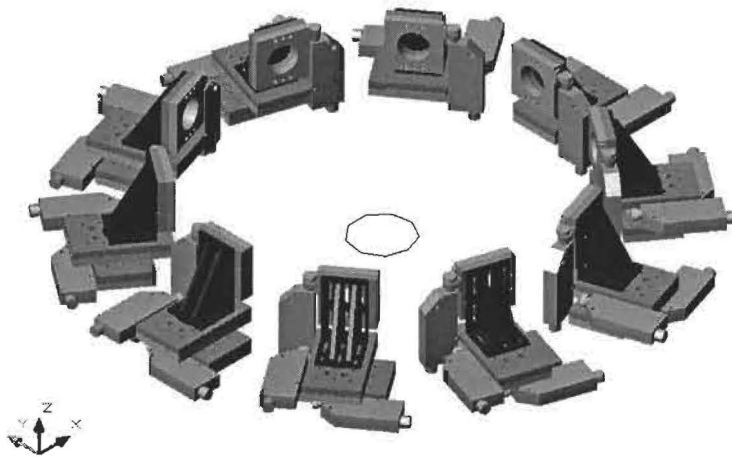


Figure 121: Layout for three axis manipulator.

leading to an extremely space inefficient scheme for positioning fibres (layout diameter / field diameter ≈ 10). Two tiers of five modules might reduce the volume required, however, to be accommodated on the SALT Instrument platform, a more compact solution needs to be found.

4.5.2 Concept Two: Parallelogram Flexure Mechanism

Using the following components:

1. 2 x M-436-A (Newport Low Stage, metric, 50mm stroke, with aperture).
2. 3 x 850G closed loop precision actuators.
3. 8 x Bendix flexures.

The two translation stages are mounted to a parallelogram flexure mechanism that can be sprung loaded to the rearward direction and actuated forward. This will keep the stages parallel to the base but will rise the level giving some Z-motion, the travel in the X direction will be extended according to $\Delta X = \sqrt{a^2 - (a - z)^2}$ where a is the length of the linkages between the two major plates. The linkage pivots are flexures to eliminate errors associated with backlash and stiction.

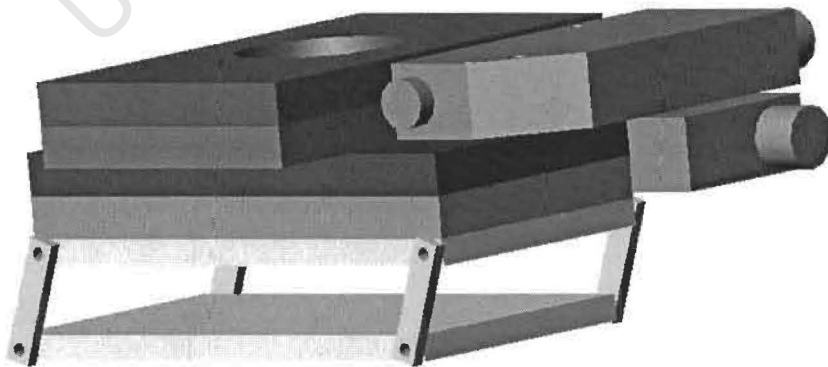


Figure 122: Parallelogram mechanism.

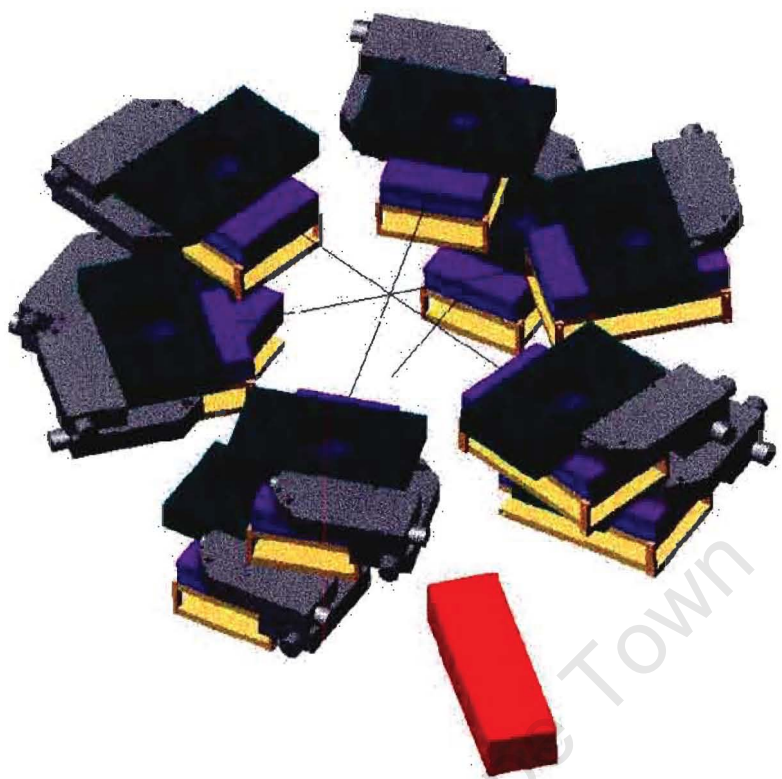


Figure 123: Layout for parallelogram mechanism.

The modules can then be arranged in two levels to reduce the overall diameter of the instrument (layout diameter / field diameter ≈ 6), and since they are low in profile the overall height is small. The red rectangular box represents a linear translation stage for positioning an Integral Field Unit or synthetic slits in the field.

4.6 CONCLUSION TO CONCEPT DEVELOPMENT

It has become clear over the course of this thesis, that the success of the Fibre Instrument Feed for SALT is dependent on the quality of its fibre optics and their implementation. In section three it is shown that because of the way the telescope works, with a fixed primary and a pupil that migrates off the mirror array, variations are introduced to the input beam that is injected into the fibre optics over the course of the track. Despite the scrambling properties of fibre optics, these variations manifest themselves in the output of the fibre optic, which in turn illuminates the spectrograph optics differently over the course of the track and thus increases the errors in quantities like line profile shape, which leads to radial velocity errors.

Section 4 sets the groundwork for the design and manufacture of the SALT's FIF. It proposes a thorough investigation to test different fibres, their scrambling and Focal Ratio Degradation properties. A test rig to this end is suggested and discussed. It is a simple design that can:

- control the speed of the injected beam into a test fibre and thus measure FRD,
- accommodate a mask to simulate the central obstruction in the injected beam and thus get a measure of scrambling,
- image the input beam to use in measurements of injected speed, optical transfer functions and throughput.
- easily accept changes in test fibres which means that fibres from different manufacturers, material types and mounting techniques can be tested.
- ensure proper alignment between the test and source fibres,
- be built on a small budget.

Following the proposed test rig investigation, an examination of possible mechanisms to position the fibre optics in the telescope's field of view is presented. It is shown that a redesign of the SAC for the SALT yields a field that is twice as large as the HET's. Suggested positioning elements for a flat focal plane include Nanomotors®, Muscle Wire (a Shape Memory Alloy), piezoelectric benders and proprietary items from *NEWPORT*, such as the Goniometric Table, Tip-Tilt Rotary tables and linear translation stages. An analysis is undertaken to examine the effect of the telecentric angle changes, in terms of a parameter ξ , a measure of misalignment between the fibre and the chief ray. It was found, as expected, that no light is lost if fibre manipulating scheme can align the fibre with the chief ray of the injected light. It is also shown that if one degree of freedom is added to the system, namely of tilt in one plane, an improvement of 58% can be realised. In addition, the HET's decision to mount their probes at a constant 1° is shown to be justified. After which, a method is shown that optically removes the exaggerated telecentric angle variation with a doublet. However, this lens adds field curvature to the focal surface with ~3mm sag that would require an X, Y and Z positioner rather than X, Y, θ and φ. Two methods are proposed to manipulate fibres in this corrected field. These both use *NEWPORT* linear translation stages. The first uses an angle bracket to mount three stages orthogonal to each other and the second uses two stages that are mounted to a flexured parallelogram mechanism. The latter scheme lends itself to the mass and volume constraints outlined in the specifications for the SALT's instrument platform.

5. CONCLUSIONS AND RECOMMENDATIONS

South Africa is building a large telescope – the Southern African Large Telescope or SALT – at the South Africa Astronomical Observatory's site in Sutherland that will be the largest single optical telescope in the southern hemisphere. It is based on the design of a telescope sited in west Texas – the Hobby-Eberly Telescope (HET). These telescopes now represent a new paradigm in telescope design that have a large fixed-altitude, segmented spherical mirror that are built for a fifth of the cost of a conventional telescope of the same size. However, for this price, only ~70% of the sky can be observed over the course of the year and observations are restricted to the time an object passes through a window 12° wide, offset $\sim 35^\circ$ from the vertical. Another consequence of the design is that the light collecting area of the telescope (the pupil) migrates off the primary mirror array, changing in size and shape, as an object is tracked across the sky (because of the Earth's rotation). An important role of SALT will be fibre-fed spectroscopy. It is important that the effects the moving pupil has on transmission of light through fibre optics is fully understood. This is one of the major aims of this thesis.

This thesis is also an investigation into the concept of a multiple object fibre feed system. It uses fibre optics as light waveguides to feed the light from the focal surface to the slit of a spectrograph mounted in an environmentally controlled room (temperature, humidity and vibration) beneath the telescope. This instrument, that positions the fibre optics, is called the Fibre Instrument Feed (FIF).

In the first major section (§2), the reader is given a basic understanding of telescopes and of optics. An introduction to the HET concept, a presentation of the properties of fibre optics and a history of multiple object spectroscopy follows. Finally, there is a discussion on the HET's Fibre Instrument Feed and an introduction to the “telecentric angle problem”.

The second major section (§3) involved work at the Pennsylvania State University on a fibre optic test rig that simulated the HET's pupil. It was used to investigate the effects that the migrating pupil has on the output beam of the fibre optic. The effects were characterised in terms of modulation (ratio of the trough depth to the peak intensity in the fibre's output beam profile) and FWHM (the width of the beam at half the maximum intensity) and were found to vary, in one case, from 17–37% and $\sim 3\%$, respectively. Such variations will cause systematic errors in precision radial velocity measurements. For these types of demanding observations, a fibre scrambler might need to be employed to increase the radial scrambling.

In the third and last major section (§4), it became clear while working on the HET's pupil simulator that more experiments on the behaviour of the fibre optics would have to be made, and a proposal to build a test rig that would characterise different fibres in terms of their scrambling and Focal Ratio Degradation is presented. It is recommended that fibres be tested of similar length ($\sim 30\text{m}$) to the length between the instrument on the telescope and the spectrograph in the room beneath. This rig will ensure the best possible fibres for use with SALT's FIF. This was followed by a presentation of various methods of positioning fibres on the focal surface. First it examined means of positioning fibres in a flat field, similar to the HET's, that would require X, Y, θ and ϕ motions, because of the telecentric angle variation. This telecentric angle variation can be described as the chief ray of a light bundle increasing its angle from the plane's normal, as its radial position in the field increases. A solution is shown whereby the telecentric angle variation is removed optically with a doublet that results in a curved field. The positioner for such a field needs only to manipulate the fibre in X, Y and Z. A design of two perpendicularly mounted linear translation stages on a parallelogram flexure mechanism is recommended.

APPENDICES

University of Cape Town

Appendix A. ADDITIONAL PHOTOGRAPHS

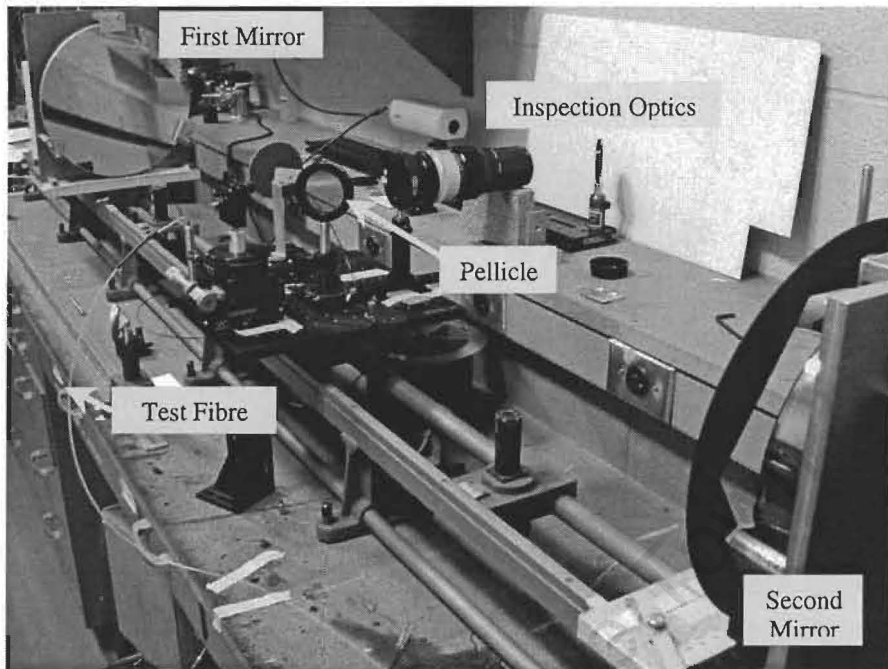


Figure 124: Bench mounted pupil simulator. At the far end, the first mirror is seen which collimates the light onto the second mirror (lower right). This focuses the light via the pellicle beamsplitter into the test fibre. The inspection optics are seen to the right of the central assembly.

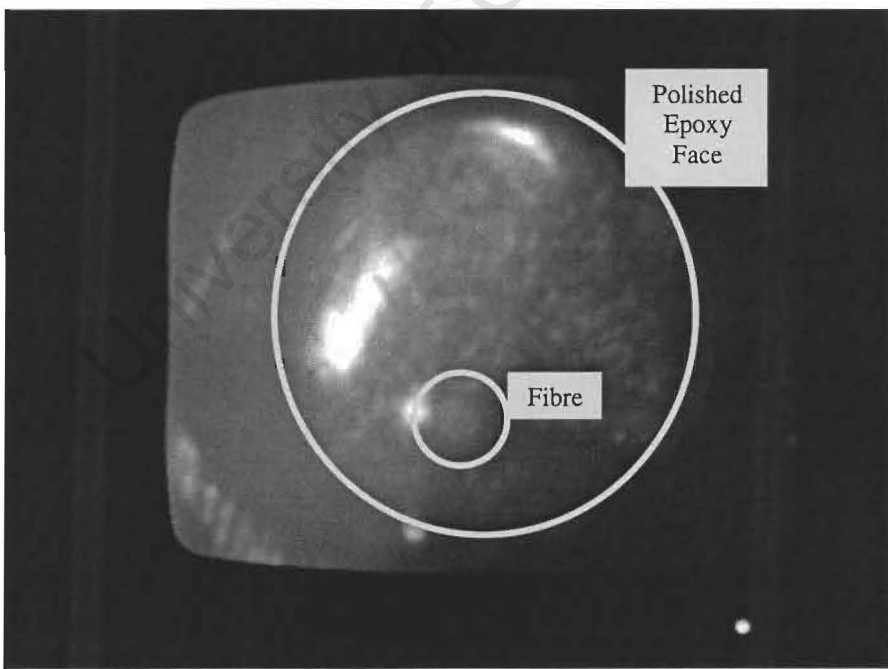


Figure 125: Fibre magnified on monitor. The light spot to the left of the indicated fibre is the focused beam from the simulator.

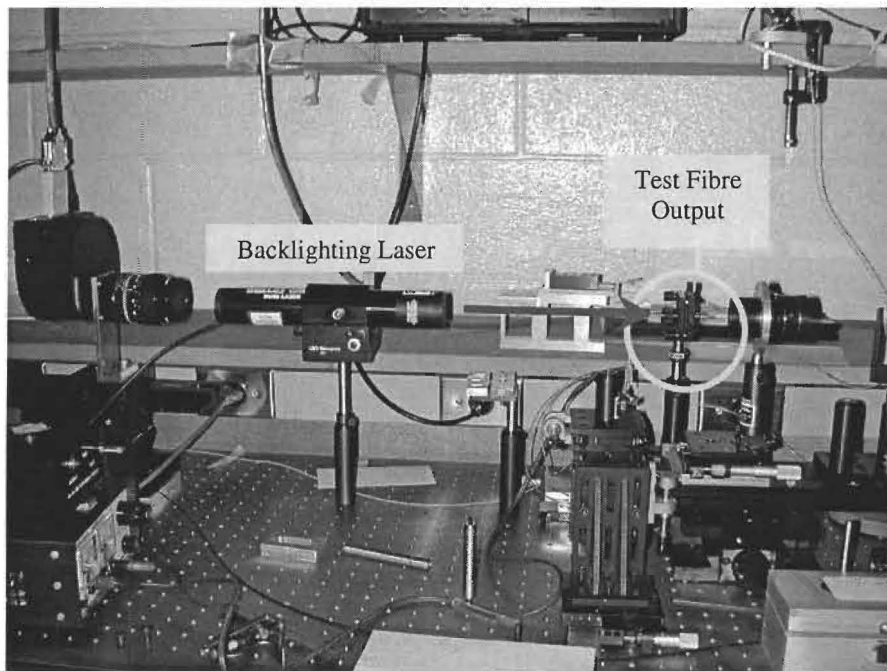


Figure 126: Backlighting test fibre with a laser. This fills the fibre with low order modes that can be used to position (tip/tilt) the input (or other end) of this fibre. Alignment is ensured when the laser spot is focused on the output of the source fibre after the reflections on the second and first mirrors.

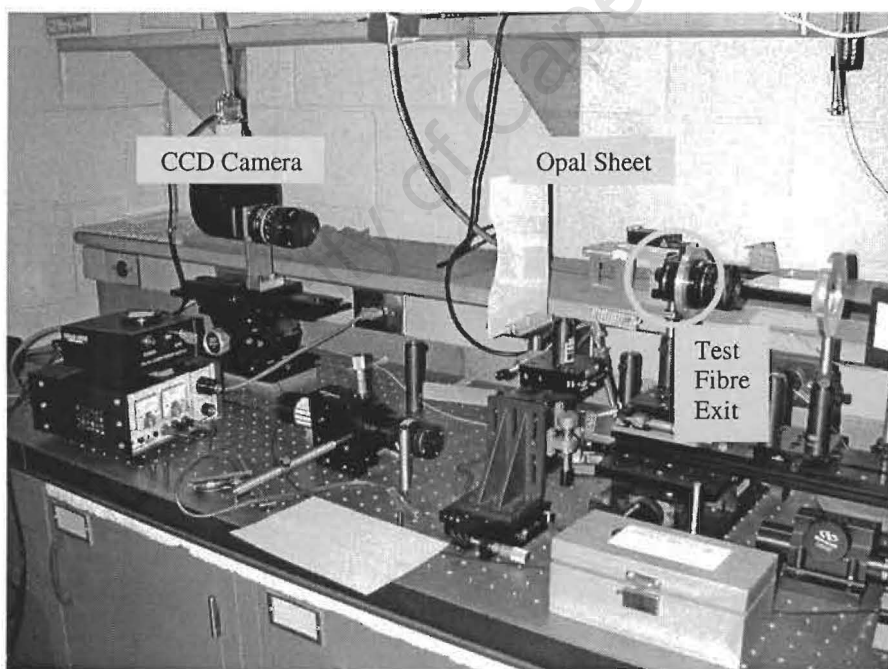


Figure 127: Original far field imaging with opal sheet.

Appendix B. EXPERIMENTAL APPARATUS

The following apparatus was used in the HET pupil simulator experiment (section three):

1. *NEWPORT* Model 780 Quartz-Tungsten halogen lamp.
2. *EDSCOMP* 60x microscope objective.
3. *NEWPORT* 5-Axis Fibre Ferrule mount.
4. Adjustable radial lens chuck.
5. Filter holder.
6. Colour filters.
7. Neutral density filters.
8. Opal diffusing glass.
9. FO#1 – 9m *POLYMICRO* FHP200240270.
10. FO#1 – 6m *POLYMICRO* FHP320385500.
11. FO#1 chuck mounted on *NEWPORT* linear stage.
12. MIR#1 – D = 12.5inch; R = 69.5inch spherical mirror.
13. MIR#2 – D = 8.011inch; R = 69.625inch spherical mirror.
14. Cardboard baffle, diameter 3inch.
15. Internal hex 200mm A/F mask.
16. Pellicle “folding” beamsplitter.
17. FO#2 – 9m *POLYMICRO* 400 μ m
18. FO#2 – 30m *POLYMICRO* 600 μ m
19. FO#2 positioner mounted on (*NEWPORT*) 2 linear and 1 rotation stages.
20. *SBIG* ST-6 & ST-8 CCD cameras.
21. TV CCD inspection camera.
22. 200, 135, 55, 50mm photographic lens.
23. 25mm SQ fold mirror.
24. Spectrograph.
25. *NIKON* CoolPix 950, digital camera.

Appendix C. SOURCE BEAM

The digital camera (*NIKON CoolPix 950*) was used to capture an image of the source projected onto an opal sheet (shown in Figure 128). The sheet was placed between the source fibre and the first mirror (see Figure 32, page 44).



Figure 128: Source beam taken with digital camera.

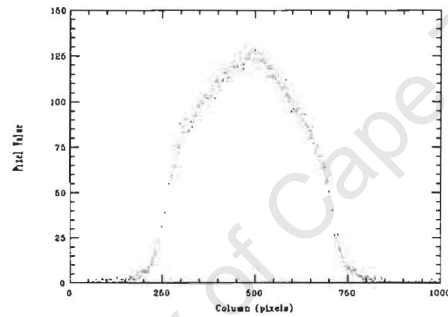


Figure 129: Source beam cross-section.

It is noted that there is a central peak to the beam profile. Ideally this should have a square profile but this perhaps more gaussian profile has to be accepted and can be dealt with. If the input and the output far field patterns are known then it is possible to obtain the optical transfer function of the fibre.

Appendix D. COLOUR TESTS

Aim and Method:

The objective is to investigate the colour dependency of the fibre scrambling by using various filters.

Colour is examined using five filters and a source fibre of 200 μm to illuminate the pupil Simulator. Far field images of the test fibre are projected onto an opal sheet and recorded with the *SBIG ST-8* CCD camera.

Apparatus and Notes:

1. Pupil Simulator and Far Field Test Rig.
2. 200 μm source fibre (length 5m).
3. 400 μm test fibre (length 9m).
4. Red Filter - 590/3.0/2
5. Yellow Filter - 530/3.0/2
6. Green Filter - BG18/2.0/2
7. Blue/Green Filter - BG14/2.0/2
8. Blue Filter - BG12/1.0/2

The names of the filter colours are arbitrary and are given for convenience in this experiment.

Errors (from measuring the curves directly from the print out i.e. before VisualBASIC Code in EXCEL was used):

Assuming that the errors are random and gaussian:

$$\delta(x+y) = \delta(x-y) = \sqrt{(\delta x)^2 + (\delta y)^2}$$

$$\frac{\delta(xy)}{xy} = \frac{\delta(x/y)}{x/y} = \left[\left(\frac{\delta x}{x} \right)^2 + \left(\frac{\delta y}{y} \right)^2 \right]^{1/2}$$

let

a = maximum intensity

b = trough intensity

c = background intensity

$$\text{Modulation } M = \frac{a-b}{a-c} = \frac{d}{e}$$

$$\delta d = \delta(a-b) = \sqrt{(\delta a)^2 + (\delta b)^2}$$

$$\delta e = \delta(a-c) = \sqrt{(\delta a)^2 + (\delta c)^2}$$

$$\frac{\delta M}{M} = \frac{\delta(d/e)}{d/e} = \left[\left(\frac{\delta d}{d} \right)^2 + \left(\frac{\delta e}{e} \right)^2 \right]^{1/2}$$

now

$$\delta M = M \left[\frac{(\delta a)^2 + (\delta b)^2}{(a-b)^2} + \frac{(\delta a)^2 + (\delta c)^2}{(a-c)^2} \right]^{1/2}$$

let $\delta a = \delta b = \delta c = \delta x$

$$\delta M = M \left[\frac{2(\delta x)^2}{(a-b)^2} + \frac{2(\delta x)^2}{(a-c)^2} \right]^{1/2}$$

similarly for FWHM & FW13.5, we can write

$$\delta F = F \left[\left(\frac{\delta f}{f} \right)^2 + \left(\frac{\delta g}{g} \right)^2 \right]^{1/2}$$

where f and g are the errors on the measurements on either side of the profile.

Colour Results:

The figures shown below are far field cross-sections. They are asymmetric because they are results pre-realignment of the rig. It is obvious from the figures the influence the misalignment of the first mirror had on the results.

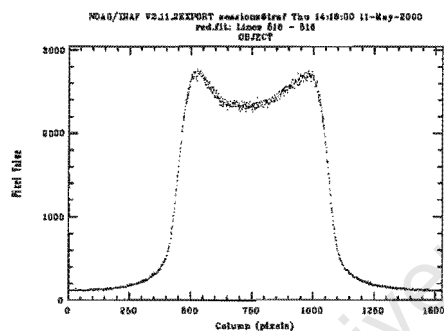


Figure 130: Red filter (10 second exposure).

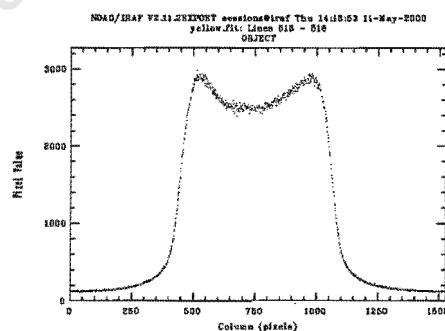


Figure 131: Yellow filter (10 second exposure).

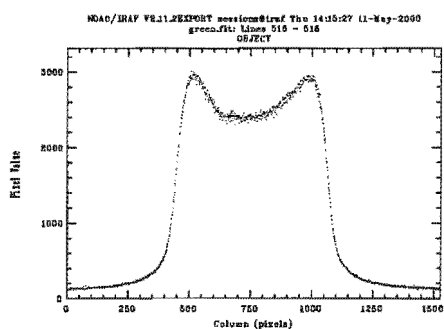


Figure 132: Green filter (90 second exposure).

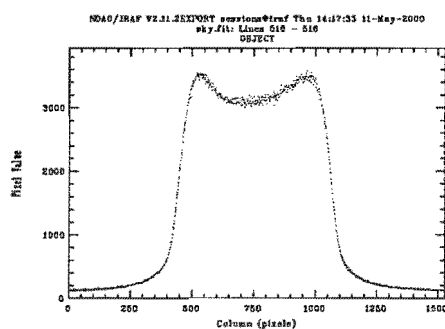


Figure 133: Blue/Green filter (60 second exposure).

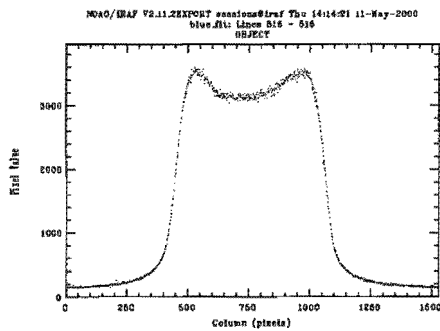


Figure 134: Blue filter (180 second exposure).

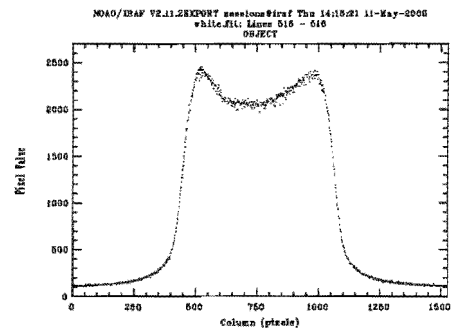


Figure 135: White - no filter (7 second exposure).

Analysis:

Modulation was measured directly on the plot with a vernier, it was assumed that the measurement error on the vertical axis was $\pm 1\text{mm}$ and on the horizontal axis, $\pm 0.25\text{mm}$. The errors are conservatively estimated to be less than 1% but this does not include systematic error due to profile variation.

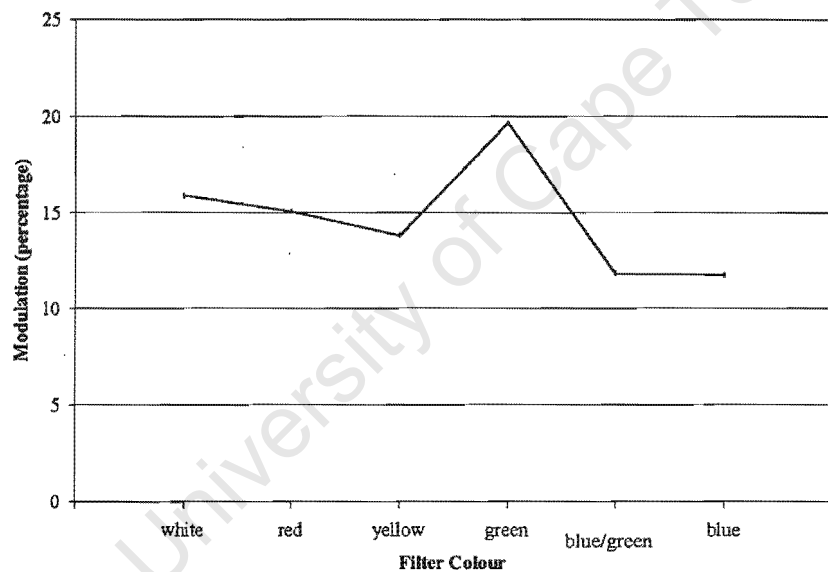


Figure 136: Plot of Modulation vs. Colour.

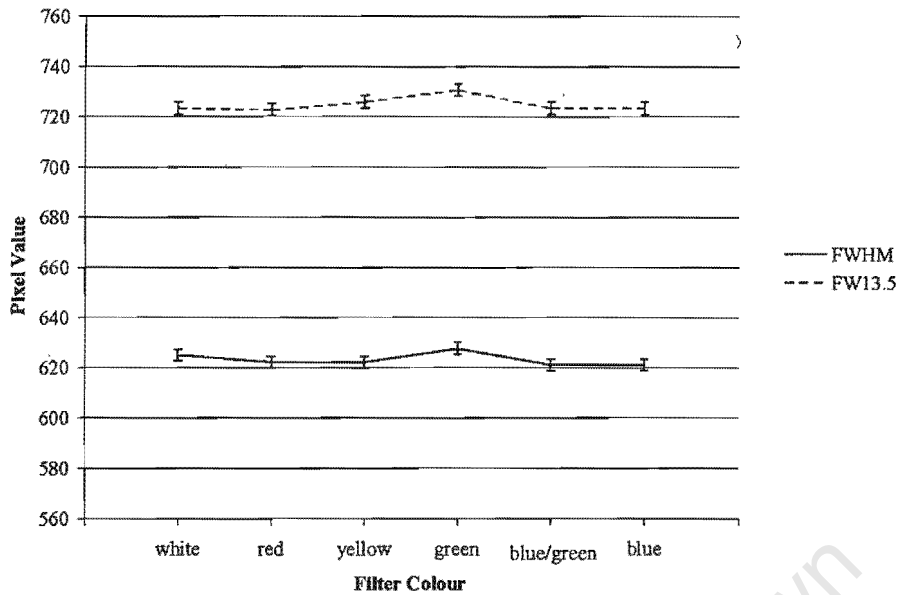


Figure 137: Filter Colour vs. FWHM & FW 13.5.

Conclusion:

The results indicate that the filters have some effect on the results. It is also noted that different filters have different bandpasses, hence the varying results, especially for the green filter. It was deduced from this experiment that all results would be recorded with a red filter to ensure that the data obtained was not colour dependent.

Appendix E. CODE TO CALCULATE THE INTENSITY VS. TIME DATA OF THE SOURCE LAMP

This code knits consecutive data series together to produce a time sequence of the lamp's brightness.

```
Sub setup()
    Dim n, Num
    Dim i, x, y
    Dim t1, t2
    n = 1
    Let Num = 5 'number of data sets to knit together.
    For i = 1 To Num
        Let file$ = "c:\data\20000316\n" + Format(i) + ".ivt"
        Open file$ For Input As #1
            ' extract time of first measurement on the file.
            For x = 1 To 3
                Line Input #1, Line$
            Next x

            t1 = Mid(Line$, 7, 2) * 3600 + Mid(Line$, 10, 2) * 60 + Mid(Line$, 13, 2)

            ' throw away header stuff.
            For x = 4 To 14
                Line Input #1, Line$
            Next x

            Line$ = t1 + Mid(Line$, 8, 7) & "," & Right(Line$, 7)
            Range("a" + Format(n)).FormulaR1C1 = Line$: n = n + 1

            ' write value into worksheet cell.
            Do Until EOF(1)
                Line Input #1, Line$
                element1 = t1 + Mid(Line$, 8, 7)
                Line$ = element1 & "," & Right(Line$, 7)
                Range("a" + Format(n)).FormulaR1C1 = Line$: n = n + 1
            Loop
            Close #1
        If i < Num Then
            Let file$ = "c:\data\20000316\n" + Format(i + 1) + ".ivt"
            Open file$ For Input As #2
                For x = 1 To 3
                    Line Input #2, Line$
                Next x
                t2 = Mid(Line$, 7, 2) * 3600 + Mid(Line$, 10, 2) * 60 + Mid(Line$, 13, 2)
            Close #2
            ' put time spacing until the time for the next file.
            For y = 1 To Int((t2 - (t1 + 600)) / 0.2)
                Line$ = element1 + 0.2 * y
                Range("a" + Format(n)).FormulaR1C1 = Line$: n = n + 1
            Next y
        End If
    Next i
End Sub
```

Appendix F. ALIGNMENT TESTS

Aim and Method:

The aim of this experiment was to measure the modulation and full widths of the test fibre far field patterns for different telecentric angles of input. The pupil simulator was used in this experiment. Additionally, this gave an indication of the sensitivity of the profiles to misalignments.

Results:

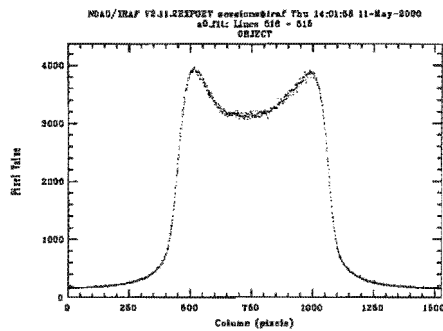


Figure 138: 0.00 degrees.

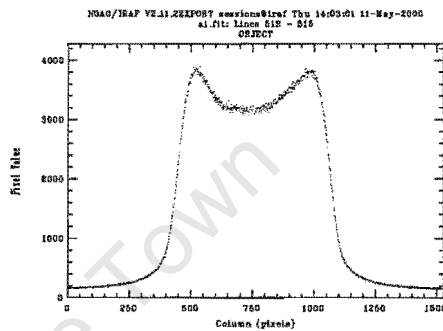


Figure 139: 0.25 degrees.

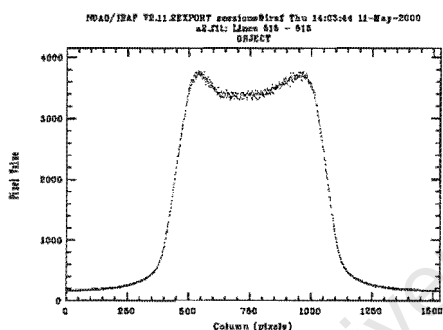


Figure 140: 0.50 degrees.

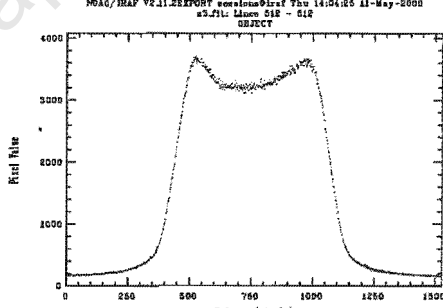


Figure 141: 0.75 degrees.

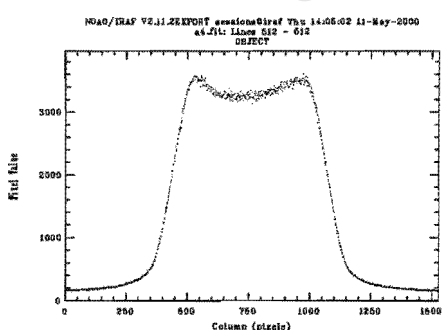


Figure 142: 1.00 degrees.

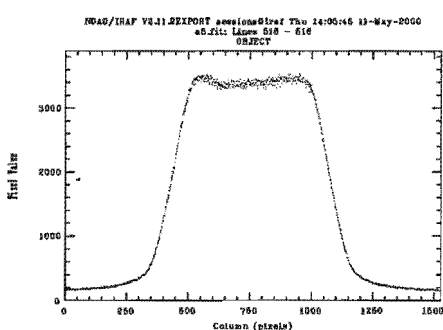


Figure 143: 1.25 degrees.

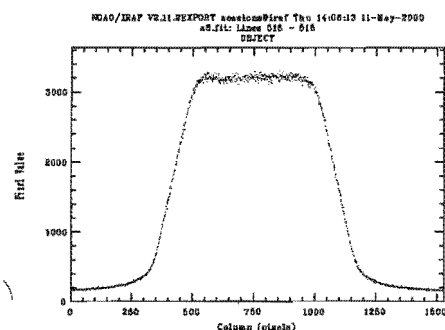


Figure 144: 1.50 degrees.

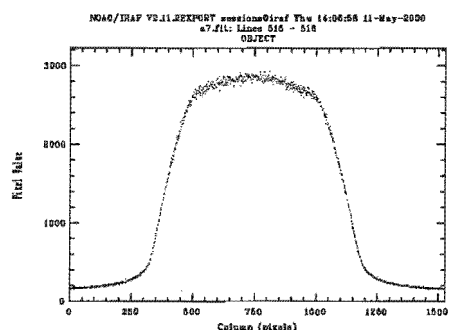


Figure 145: 1.75 degrees.

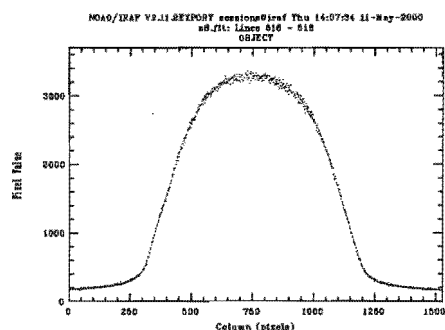


Figure 146: 2.00 degrees.

Analysis:

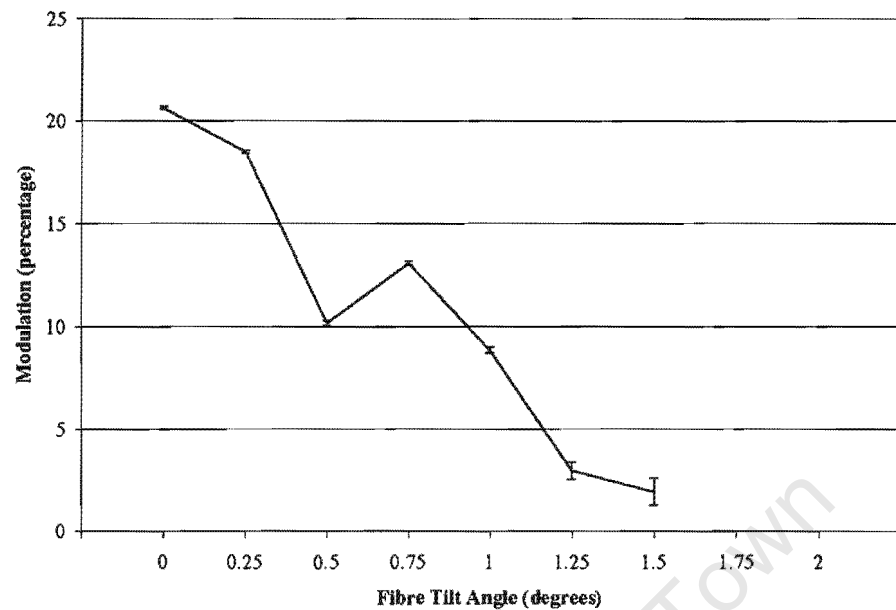


Figure 147: Plot of Modulation vs. Tilt Angle.

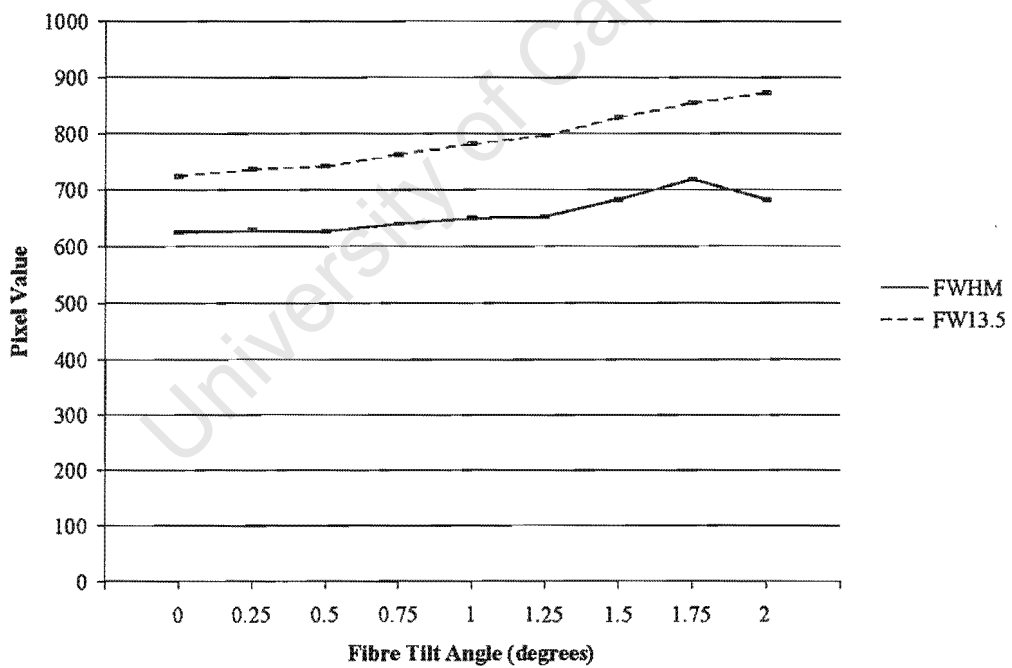


Figure 148: Plot of Pixel Value of FWHM & FW13.5 vs. Tilt Angle.

Discussion:

It was seen that when the pupil structure was injected into the test fibre the modulation reduces and the full widths increase. The rig was thus sensitive to misalignment. The laser could be used in its backlighting mode (see § 3.2.3) to ensure proper alignment.

Appendix G. JUSTIFICATION ON TAKING THE BARE FIELD

Objective:

The objective was to determine whether the images of the “bare field”, that is, where the exiting beam from the fibre optic was projected directly onto the CCD, were truly far field representations. The ferrule was put up against the glass window of the CCD and the field was imaged. The CCD was then stepped away in equal increments. If the values for modulation were to plateau, then the “bare field” is ensured to be the far field.

Results:

Code	Distance between fibre exit and chip
10	2.8mm
11	5.3mm
12	7.8mm
13	10.3mm
14	12.8mm
15	15.3mm
16	17.8mm
17	20.3mm
18	22.8mm
19	25.3mm
110	27.8mm
111	30.3mm
112	32.8mm

Table 4: Distance between fibre and chip related to code used.

IRAF was used in this instance to reduce the data.

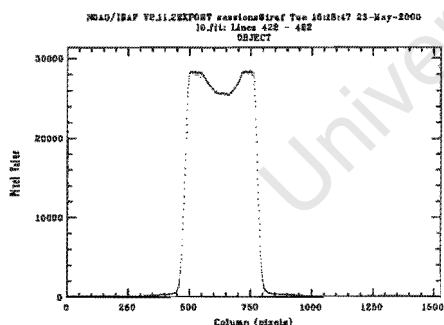


Figure 149: 10 Cross-section – d = 2.8mm.

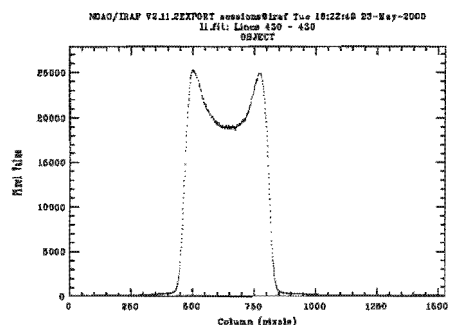


Figure 150: 11 Cross-section – d = 5.3mm.

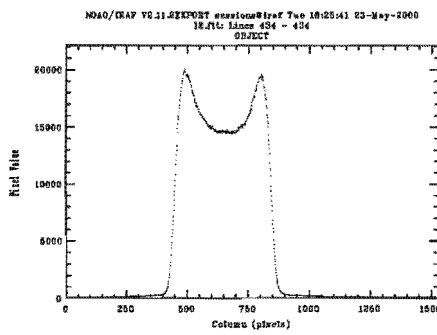


Figure 151: I2 Cross-section – $d = 7.8\text{mm}$.

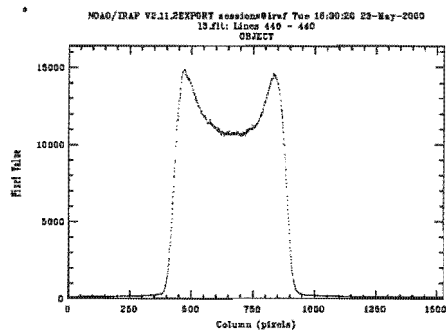


Figure 152: I3 Cross-section – $d = 10.3\text{mm}$.

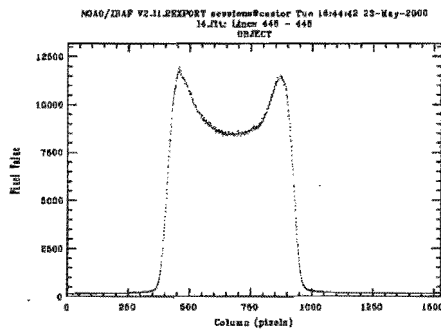


Figure 153: I4 Cross-section – $d = 12.8\text{mm}$.

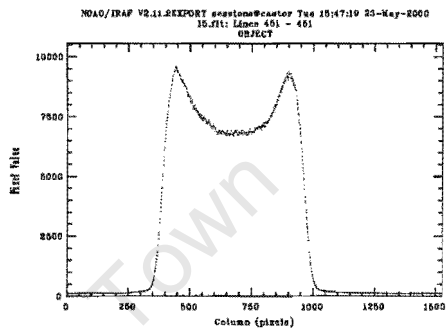


Figure 154: I5 Cross-section – $d = 15.3\text{mm}$.

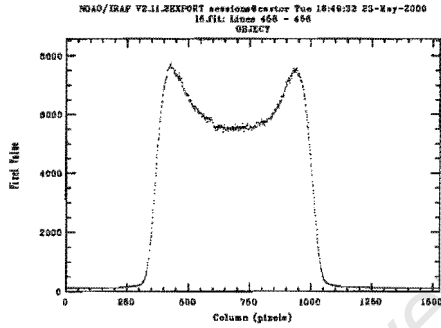


Figure 155: I6 Cross- section – $d = 17.8\text{mm}$.

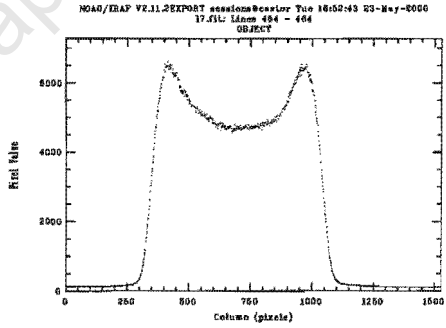


Figure 156: I7 Cross-section – $d = 20.3\text{mm}$.

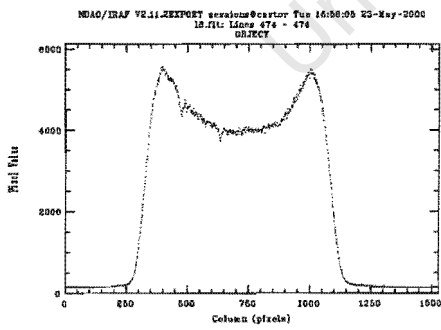


Figure 157: I8 Cross-section – $d = 22.8\text{mm}$.

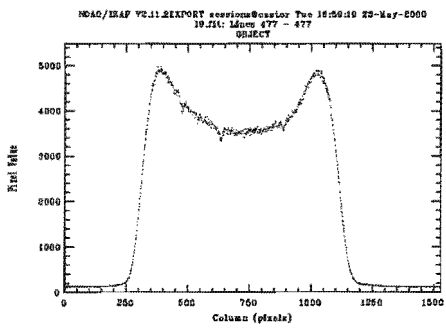


Figure 158: I9 Cross-section – $d = 25.3\text{mm}$.

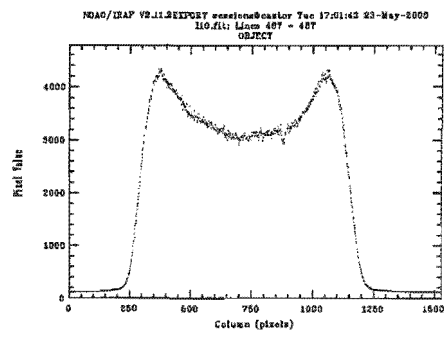


Figure 159: I10 Cross-section – d = 27.8mm.

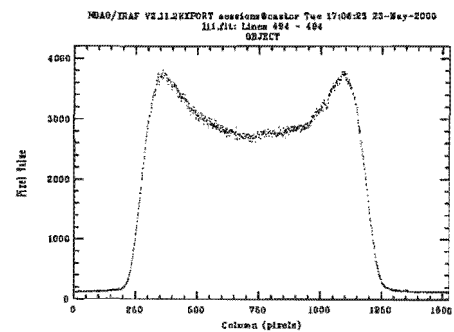


Figure 160: I11 Cross-section – d = 30.3mm.

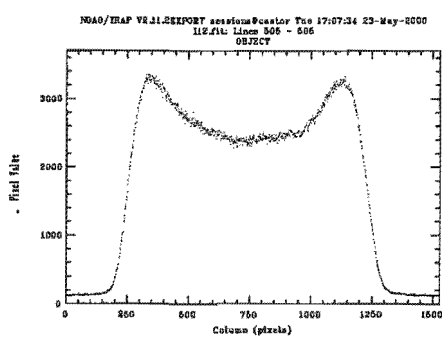


Figure 161: I12 Cross-section – d = 32.8mm.

Analysis:

The modulation and full width curves are over-plotted below in Figure 162:

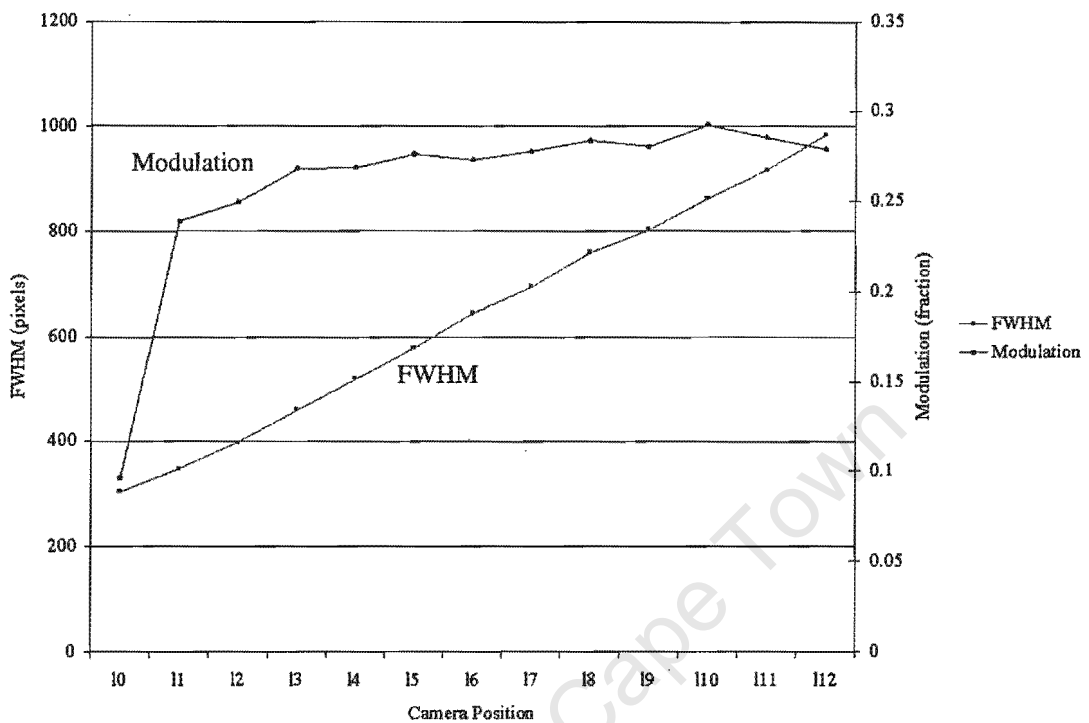


Figure 162: FWHM and modulation vs. camera position.

In the first position (10) it would appear that modulation is severely decreased, however this is due to the camera saturating at approximate counts of 32,000 (flat top in Figure 149; despite using 16 bit [65,536] digitisation). The following image (11) does not exhibit any indication of saturation (Figure 150) and thus the experiment is not void.

It is clear that modulation plateaus, meaning that this “bare field” is in fact a good representation of the far field.

The plot of the FWHM is very close to linear. This implies that the camera was stepped at accurate equal increments.

Appendix H. VISUALBASIC CODE FOR IMAGE REDUCTION IN EXCEL

Objective:

The objective was to write a code that could handle the entire data set. It calculated profile full width, modulation, centroid and the cross-sections for each mask position in each image set (i.e. 7 mask positions x 5 image sets).

Code:

```
Public picture(1 To 1020, 1 To 1530)
Dim a, b, h, i, j, k, l, r, x As Integer
Dim LineLength As Integer, LineCounter As Integer
Dim Truck$, Line$, FileName$
Dim squash(1 To 1530) As Double
Dim element As Double, MomentLeft As Double, MomentRight As Double
Dim flag As Boolean, LineBalance As Boolean
Dim LineCentroid As Integer, ColumnCentroid As Integer
Dim criteria As Double, enclosed As Double, t1 As Double, t2 As Double
Dim peak As Integer, Trough As Integer
Dim LineCut(1 to 1530) As Integer

Sub main()
    For ImageSet = 31 To 35
        Let flag = False
        With Sheets("Sheet" & Format(ImageSet - 30))
            .Select
            .Name = "Set " & Format(ImageSet)
        End With
        Sheets("Set 35").Select
        For m = -6 To 6
            Let t1 = Timer
            'load array
            FileName$ = "d:/data/text/bfs0m" & Format(m) & "n" & Format(ImageSet) & ".txt"
            Call LoadArray(FileName$)

            'find criteria: twice background
            criteria = 0
            For i = 1 To 5
                For j = 1 To 5
                    criteria = criteria + picture(i, j) + picture(1021 - i, 1531 - j)
                Next j
            Next i
            criteria = (criteria / 50) * 2

            'find centroid
            LineCentroid = centroid(1020, 1530, criteria)
            ColumnCentroid = centroid(1530, 1020, criteria)

            'print Cross-Section values
            If flag = False Then
                Range("a1").Formula = "Cross-Sections:"
            End If

            Range(Chr(104 + m) & "2").Formula = "m" & Format(m)

            For i = 1 To 1530
                If flag = False Then Range("a" & Format(i + 2)).Formula = i
                Range(Chr(104 + m) & Format(i + 2)).Formula = picture(LineCentroid, i)
            Next i

            Call frd(LineCentroid, ColumnCentroid, criteria, m)
```

```

Call Engine(m, criteria, LineCentroid)

Let flag = True
Next m
Next ImageSet

End Sub
Sub Engine(m, c, l)

peak = Application.WorksheetFunction.Max(Range(Chr(104 + m) & "3:" & Chr(104 + m) & "1532"))

i = 765
Do Until picture(l, i) > picture(l, 765) + 100
    i = i - 1
Loop
trough1 = i

i = 765
Do Until picture(l, i) > picture(l, 765) + 100
    i = i + 1
Loop
trough2 = i

Trough = Application.WorksheetFunction.Min(Range(Chr(104 + m) & Format(trough1 + 2) & ":" & Chr(104 + m)
& Format(trough2 + 2)))

For i = 1 To 1530
    Let LineCut(i) = Range(Chr(104 + m) & Format(i + 2))
    Select Case LineCut(i)
        Case peak: Let xPeak = i
        Case Trough: Let xTrough = i
    End Select
Next i

Let delta = 5

PeakAve = Application.WorksheetFunction.Average(Range(Chr(104 + m) & Format((xPeak - delta) + 2) & ":" &
Chr(104 + m) & Format((xPeak + delta) + 2)))

TroughAve = Application.WorksheetFunction.Average(Range(Chr(104 + m) & Format((xTrough - (3 * delta)) +
2) & ":" & Chr(104 + m) & Format((xTrough + (3 * delta)) + 2)))

BackAve = c / 2

'MODULATION
modulation = (PeakAve - TroughAve) / (PeakAve - BackAve) * 100

'FWHM
F1 = BackAve + (PeakAve - BackAve) / 2
j = 1
Do Until LineCut(j) > F1
    j = j + 1
Loop
Let F50x1 = j - 2
j = 1530
Do Until LineCut(j) > F1
    j = j - 1
Loop
Let F50x2 = j + 2

'FW13.5
F2 = BackAve + (PeakAve - BackAve) * 0.135
j = 1
Do Until LineCut(j) > F2
    j = j + 1
Loop
Let F135x1 = j - 2
j = 1530
Do Until LineCut(j) > F2
    j = j - 1
Loop
Let F135x2 = j + 2

If flag = False Then

```

```

Range("ae1").Formula = "Characteristics:"
Range("ae3").Formula = "xPeak:"
Range("ae4").Formula = "Peak:"
Range("ae5").Formula = "xTrough:"
Range("ae6").Formula = "Trough:"
Range("ae7").Formula = "Trough1:"
Range("ae8").Formula = "Trough2:"
Range("ae9").Formula = "Back:"
Range("ae10").Formula = "FWHM:"
Range("ae11").Formula = "FWL3.5:"
Range("ae12").Formula = "Mod:"
Range("ae13").Formula = "Time:"
End If

Range("a" & Chr(108 + m) & "2").Formula = "m" & Format(m)
Range("a" & Chr(108 + m) & "3").Formula = xPeak
Range("a" & Chr(108 + m) & "4").Formula = PeakAve
Range("a" & Chr(108 + m) & "5").Formula = xTrough
Range("a" & Chr(108 + m) & "6").Formula = TroughAve
Range("a" & Chr(108 + m) & "7").Formula = trough1
Range("a" & Chr(108 + m) & "8").Formula = trough2
Range("a" & Chr(108 + m) & "9").Formula = BackAve
Range("a" & Chr(108 + m) & "10").Formula = F50x2 - F50x1
Range("a" & Chr(108 + m) & "11").Formula = F135x2 - F135x1
Range("a" & Chr(108 + m) & "12").Formula = modulation
Let t2 = Timer
Let t2 = Timer
Range("a" & Chr(108 + m) & "13").Formula = (t2 - t1) / 60

End Sub

Sub LoadArray(FileNames$)

Open FileName$ For Input As #1

For i = 1 To 1020
Line Input #1, Line$
x = 1: LineLength = Len(Line$)

For j = 1 To 1530
Truck$ = ""
Do Until Asc(Mid(Line$, x, 1)) = 9 Or x = LineLength
Truck$ = Truck$ & Mid(Line$, x, 1): x = x + 1
Loop

If x <> LineLength Then
picture(i, j) = Val(Truck$)
Else
picture(i, j) = Val(Truck$ & Mid(Line$, x, 1))
End If

x = x + 1

Next j
Next i

Close #1
End Sub

Function centroid(a, b, c)

For i = 1 To a
element = 0
For j = 1 To b
If b > a Then
element = element + picture(i, j)
Else
element = element + picture(j, i)
End If
Next j
squash(i) = element / b
Next i

Let LineBalance = False
Let x = 2

```

```
Do Until LineBalance = True
Let MomentLeft = 0
Let y = x - 1
Do Until y = 0
  If squash(y) > c Then MomentLeft = MomentLeft + ((x - y) * c)
  y = y - 1
Loop
Let MomentRight = 0
Let y = x + 1
Do Until y = a + 1
  If squash(y) > c Then MomentRight = MomentRight + ((y - x) * c)
  y = y + 1
Loop
If MomentLeft >= MomentRight Then Let LineBalance = True
x = x + 1
Loop

centroid = x - 1

End Function
```

Appendix I. PROGRAM TO FIND THE CENTROID

1. Aim and Method:

The objective was to develop a code that finds the centroid of a profile accurately so that the cross-section for different images could be obtained.

Several approaches were taken (using the image shown in Figure 163):

1. Intensity moment balance was taken with the background.
2. Intensity moment balance was taken without the background.
3. The width of beam was measured in each row.
4. The centroid was calculated by a method described in the ST-8 Manual.

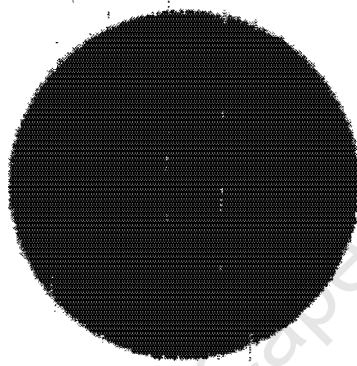


Figure 163: The image used in this appendix - bfs0m0n32.jpg

2. Results:

Code used to load file into array

```
Public picture(1 To 1020, 1 To 1530)

Sub zzz()
    Let FileName$ = "c:/data/20000531/bfs0m0n32.txt"
    Open FileName$ For Input As #1
    For i = 1 To 1020
        Line Input #1, Line$
        x = 1: LineLength = Len(Line$)
        For j = 1 To 1530
            Truck$ = ""
            Do Until Asc(Mid(Line$, x, 1)) = 9 Or x = LineLength
                Truck$ = Truck$ & Mid(Line$, x, 1): x = x + 1
            Loop
            If x <> LineLength Then
                picture(i, j) = Val(Truck$)
            Else
                picture(i, j) = Val(Truck$ & Mid(Line$, x, 1))
            End If
            x = x + 1
        Next j
    Next i
    Close #1
End Sub
```

Time taken to run: 73 seconds.

Using Method 1 (Intensity moment balance with background):

```
Sub BalanceFinder()
    Let t1 = Timer
    Sheets("sheet3").Select
    For i = 1 To 1020
        element = 0
        For j = 1 To 1530
            element = element + picture(i, j)
        Next j
        Squash(i) = element / 1530
        Range("a" & Format(i)).Formula = i
        Range("b" & Format(i)).Formula = Squash(i)
    Next i
    Let LineBalance = False
    Let x = 2
    Do Until LineBalance = True
        Let MomentLeft = 0
        Let y = x - 1
        Do Until y = 0
            MomentLeft = MomentLeft + ((x - y) * Squash(y))
            y = y - 1
        Loop
        Let MomentRight = 0
        Let y = x + 1
        Do Until y = 1021
            MomentRight = MomentRight + ((y - x) * Squash(y))
            y = y + 1
        Loop
        If MomentLeft >= MomentRight Then Let LineBalance = True
        x = x + 1
    Loop
    Range("c1").Formula = "linecut:"
    Range("d1").Formula = x - 1
    Let t2 = Timer
    Range("c2").Formula = "time:"
    Range("d2").Formula = t2 - t1
End Sub
```

Time taken to run: 3.7 seconds

The code calculates the “centre of luminosity” to be at line 479, as seen in Figure 164 by the dashed line.

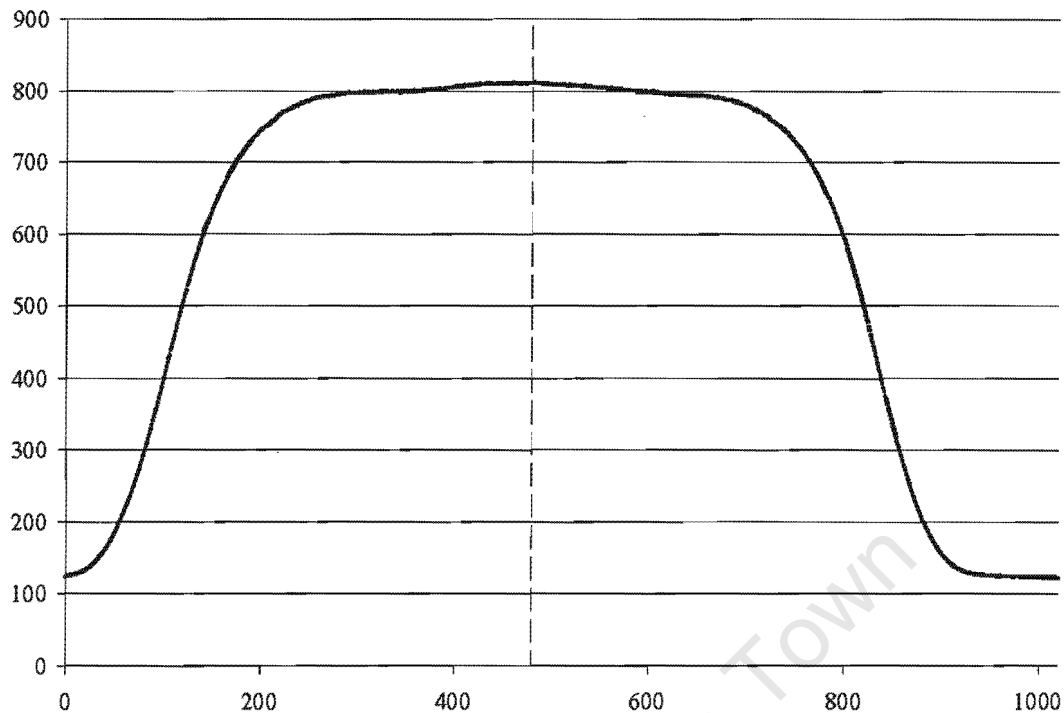


Figure 164: Plot of average line pixel values vs. line number for method 1.

It is seen that this is not the centre of the beam.

Using Method 2 (Intensity moment balance without background):

```

Sub BalanceFinder2()
Let t1 = Timer
Sheets("sheet4").Select
For i = 1 To 1020
    element = 0
    For j = 1 To 1530
        element = element + picture(i, j)
    Next j
    Squash(i) = element / 1530
    Range("a" & Format(i)).Formula = i
    Range("b" & Format(i)).Formula = Squash(i)
Next i
Let LineBalance = False
Let x = 2
Do Until LineBalance = True
    Let MomentLeft = 0
    Let y = x - 1
    Do Until y = 0
        If Squash(y) > 200 Then MomentLeft = MomentLeft + ((x - y) * Squash(y))
        y = y - 1
    Loop
    Let MomentRight = 0
    Let y = x + 1
    Do Until y = 1021
        If Squash(y) > 200 Then MomentRight = MomentRight + ((y - x) * Squash(y))
        y = y + 1
    Loop
    If MomentLeft >= MomentRight Then Let LineBalance = True
    x = x + 1
Loop
Range("c1").Formula = "linecut:"
```

```

Range("d1").Formula = x - 1
Let t2 = Timer
Range("c2").Formula = "time:"
Range("d2").Formula = t2 - t1
End Sub

```

Time taken to run: 3.7 seconds

The code calculates the “centre of luminosity” to be at line 470, as seen in Figure 165 by the dashed line. It only uses those points with pixel values above 200.

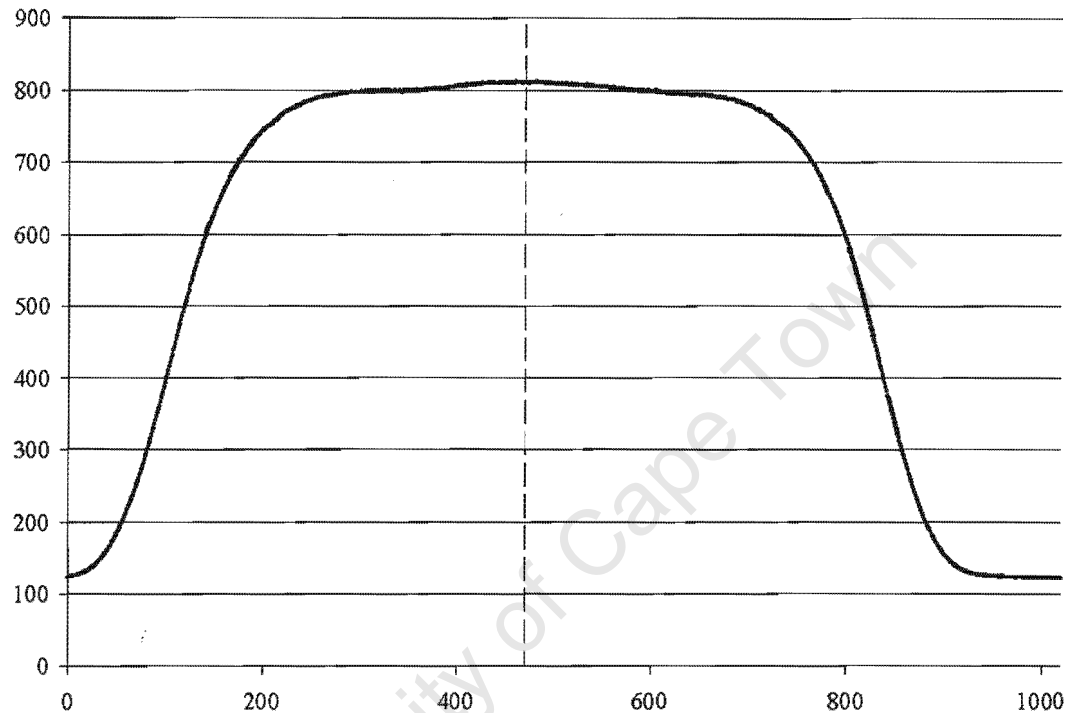


Figure 165: Plot of average line pixel values vs. line number for method 2.

The dashed line appears to be in the centre of the beam.

Using Method 3 (Measuring the width of the beam in each line):

```

Sub BalanceFinder3()
    Let t1 = Timer
    Sheets("sheet5").Select
    maxvalue = 0
    For i = 1 To 1020
        For j = 1 To 1530
            If picture(i, j) > maxvalue Then maxvalue = picture(i, j)
        Next j
    Next i
    For i = 1 To 1020
        j = 0
        Do
            j = j + 1
        Loop Until j = 1530 Or picture(i, j) > maxvalue / 2
        Let x1 = j
        j = 1531
        Do
            j = j - 1
        Loop Until j = 1 Or picture(i, j) > maxvalue / 2
    Next i
End Sub

```

```

Let x2 = j
Range("a" & Format(i)).Formula = i
If Sgn(x2 - x1) = 1 Then Range("b" & Format(i)).Formula = x2 - x1
Next i
Let spotWidth = Application.WorksheetFunction.Max(Range("b1:b1530"))
Range("c1").Formula = "SpotWidth:"
Range("d1").Formula = spotWidth
Let t2 = Timer
Range("c2").Formula = "time:"
Range("d2").Formula = t2 - t1
End Sub

```

Time taken to run: 7.9 seconds



Figure 166: Plot of beam width vs. line number for method 3.

The line numbers corresponding to the maximum value obtained using this method are:

- a. 459
- b. 461
- c. 462
- d. 474
- e. 477
- f. 484

The mean value: 469.5

This is within a tenth of a percent of the result in method 2.

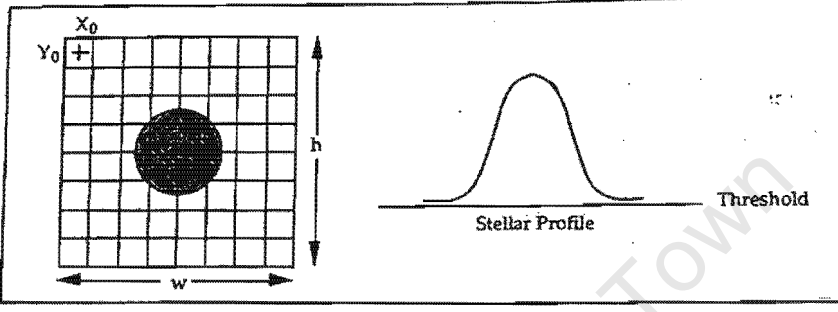
Using Method 4 (Calculation of Centroid):

Reference:

CCD Camera Operating Manual for the ST-7 and ST-8
Santa Barbara Instrument Group
First Revision, December 1994
Page 74

6.7.3. Calculation of Centroids

The centroid calculation is directly analogous to a center-of-mass calculation for an object if you represent the local mass density with the pixel intensity values and allow a discrimination level at the average background level. This is shown in the following figures and formulas:



$$\text{Threshold} = \frac{\sum_{i=0}^{w-1} \sum_{j=0}^{h-1} P(i, j)}{h \times w}$$

where in the formula above $P(i, j)$ represents the intensity value of the pixel at $x=X_0+i$, $y=Y_0+j$. Also the *Threshold* value which will be used as a discrimination level in the centroid calculation is taken over the background area and represents the average pixel level in the background area.

$$X_{\text{centroid}} = X_0 + \frac{\sum_{i=0}^{w-1} \sum_{j=0}^{h-1} i \times (P(i, j) - \text{Threshold})}{\sum_{i=0}^{w-1} \sum_{j=0}^{h-1} P(i, j) - \text{Threshold}}$$

$$Y_{\text{centroid}} = Y_0 + \frac{\sum_{i=0}^{w-1} \sum_{j=0}^{h-1} j \times (P(i, j) - \text{Threshold})}{\sum_{i=0}^{w-1} \sum_{j=0}^{h-1} P(i, j) - \text{Threshold}}$$

where in the formulas above should the quantity $P(i, j) - \text{Threshold}$ be less than zero, zero is substituted on a pixel-by-pixel basis.

Figure 167: Excerpt from manual for method 4.

The method described here is that of Method 2.

Conclusion:

From the above results from the various methods, we shall use Method 2 for the calculation of the centroid to be used in obtaining future cross-sections.

Appendix J. COMPARING CENTROID RESULTS TO THOSE USING IRAF

Aim:

The objective is to compare the centroid calculated by IRAF to the VisualBASIC code based on that written in Appendix I.

Results

	<i>IRAF</i>	<i>METHOD 1</i>	<i>METHOD 2</i>
Line	469	470 (0.2%)	470 (0.2%)
Column	748	760 (1.6%)	761 (1.6%)

Table 5: Method 1 & 2 results compared to IRAF, the brackets are percentages of the IRAF result.

In Summary and Conclusion:

Method 1 compresses the image to a one dimensional array and then “balances” the “beam” about a fulcrum by taking moments (pixel distance from fulcrum x intensity).

Method 2 recognises that the image is not symmetric and so instead of taking “intensity moments” (as Method 1), it balances the beam without the weighted intensity and only considers those pixels above a threshold value.

Since the two results are, at worst, within 1.6%, the difference is considered negligible. The VB results are used with confidence. In addition, they provide convenient results that can be used in other calculations from the image instead of asking for user input.

Appendix K. CODE TO FIND THE FOCAL RATIO DEGRADATION

Objective:

A code was written to find the centroid, then take incremental steps out in radius from that point, and add the counts in each pixel to the enclosed energy value within that radius, to plot enclosed energy vs. output f/number.

Code:

```
Sub frd(lc, cc, c, m)
    'look at enclosed energy
    Dim ee()
    r = 125
    Do Until picture(lc, cc + r) < c
        r = r + 5
    Loop
    Let rmax = r
    eemax = rmax / 5 - 25
    ReDim ee(eemax)

    For i = 1 To 1020
        For j = 1 To 1530
            rpixel = ((lc - i) ^ 2 + (cc - j) ^ 2) ^ 0.5
            If rpixel <= rmax Then
                Let r = rmax
                Do Until r = 120
                    If rpixel < r Then ee(r / 5 - 25) = ee(r / 5 - 25) + picture(i, j)
                    r = r - 5
                Loop
            End If
        Next j
    Next i

    'HouseKeeping
    If flag = False Then
        Range("p1").Formula = "FRD - Enclosed Energy:"
        Range("p2").Value = "f/#"
        For i = 0 To eemax
            Range("p" & Format(i + 3)).Value = 33.3 / (2 * (i + 25) * 5 * 9 / 1000)
        Next i
    End If

    If 119 + m <= 122 Then
        Range(Chr(119 + m) & "2").Formula = "m" & Format(m)
    Else
        Range("a" & Chr(93 + m) & "2").Formula = "m" & Format(m)
    End If
    'frd
    For i = 0 To eemax
        If 119 + m <= 122 Then
            Range(Chr(119 + m) & Format(i + 3)).Value = ee(i) / ee(eemax) * 100
        Else
            Range("a" & Chr(93 + m) & Format(i + 3)).Value = ee(i) / ee(eemax) * 100
        End If
    Next i

End Sub
```

Appendix L. OPTIMISING FRD CODE

The original code used (Appendix K) would take approximately 25 minutes to run. To analyse many images it was realised that this time would have to be reduced.

The original code [sub frd2(...)] below was like using a bulldozer to go through every pixel and identified whether it was contained within a certain radius of the centroid and then tallied up the intensities. The program would then repeat itself for the next increment in radius until it had enclosed the entire spot.

The next code [sub frd(...)] worked the other way around. It still rastered through the image, however, it immediately dismissed the pixels that were not going to be enclosed and while it was on a particular pixel it cycled through the radii. This decreased the time to approximately 3 minutes, less than 15% expensive in computing time!

```
Sub frd(lc, cc, c, m)
    'look at enclosed energy
    Dim ee()
    r = 125
    Do Until picture(lc, cc + r) < c
        r = r + 5
    Loop
    Let rmax = r
    eemax = rmax / 5 - 25
    ReDim ee(eemax)

    For i = 1 To 1020
        For j = 1 To 1530
            rpixel = ((lc - i) ^ 2 + (cc - j) ^ 2) ^ 0.5
            If rpixel <= rmax Then
                Let r = rmax
                Do Until r = 120
                    If rpixel < r Then ee(r / 5 - 25) = ee(r / 5 - 25) + picture(i, j)
                    r = r - 5
                Loop
            End If
        Next j
    Next i

    For i = 0 To eemax
        Range("c" & Format(i + 2)).Value = (i + 25) * 5
        Range("d" & Format(i + 2)).Value = ee(i)
    Next i

End Sub

Sub frd2(lc, cc, c)
    'look at enclosed energy
    r = 125
    Do Until picture(lc, cc + r) < c
        enclosed = 0
        For i = 1 To 1020
            For j = 1 To 1530
                If (lc - i) ^ 2 + (cc - j) ^ 2 < r ^ 2 Then Let enclosed = enclosed + picture(i, j)
            Next j
        Next i
        Range("a" & Format(r / 5 - 23)).Formula = r
        Range("b" & Format(r / 5 - 23)).Formula = enclosed
        r = r + 5
    Loop

End Sub
```

Appendix M. SCRAMBLING EFFECTS

Objective:

The objective is to manipulate the exit beam from the test fibre to the exit beam of the pupil simulator to get an idea of the scrambling involved.

Apparatus:

1. Pupil Simulator.
2. Source fibre, 5m, 200 μm core.
3. Test fibre, 9m, 400 μm core.

Results:

To look at the input beam:

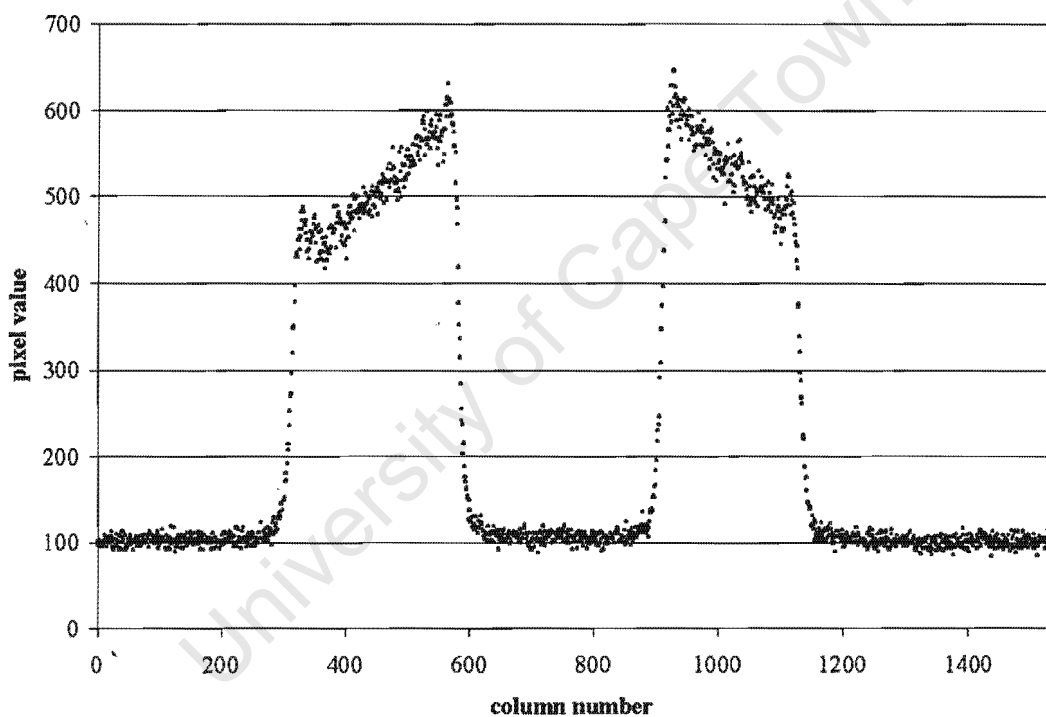


Figure 168: Input beam to fibre.

The f/number of this beam ($f/4.57$) is known. The following widths are then measured:

FW150	841
FW200	831
FW400	808

Table 6: Full widths

Where $\text{FW}(x)$ corresponds to the width at (x) pixel value.

From this table assume a width of 830 pixels or 7.47mm (for 9 μ m pixels) then $f = f/\# (d) = 4.57 (7.47) \approx 34$ mm. And then place the CCD this distance (~34mm) behind the exit face of the test fibre and record the far field pattern.

Overplotting the two data sets:

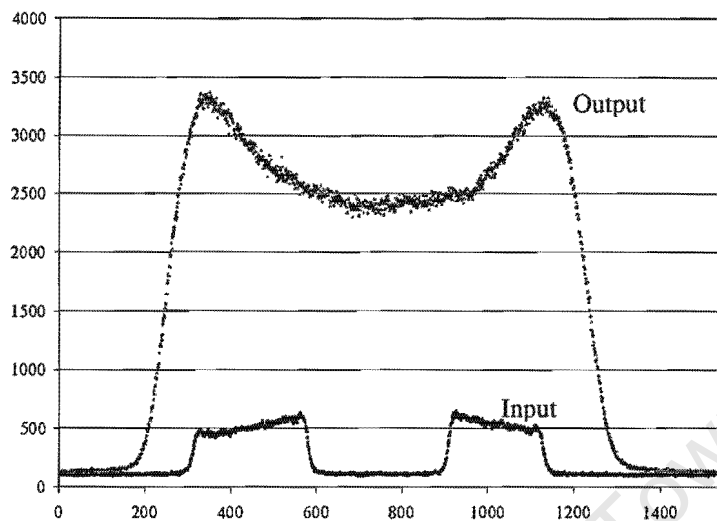


Figure 169: Plot of the input and output profiles to and from the fibre.

The intensities are different because the input beam was recorded with a very fast exposure time to ensure that the CCD did not saturate.

Using the following code:

```

Sub start()
    Dim pup(1528), out(1528)
    Sheets("Sheet3").Select
    For i = 0 To 1528
        pup(i) = Range("b" & Format(i + 2))
        out(i) = Range("c" & Format(i + 2))
    Next i
    puppeak = Application.WorksheetFunction.Max(Range("b2:b1530"))
    outpeak = Application.WorksheetFunction.Max(Range("c2:c1530"))
    pupback = Application.WorksheetFunction.Min(Range("b2:b1530"))
    outback = Application.WorksheetFunction.Min(Range("c2:c1530"))
    pupF = pupback + (puppeak - pupback) / 2
    outF = outback + (outpeak - outback) / 2
    i = 0
    Do Until pup(i) > pupF
        i = i + 1: Loop: Let pupx1 = i
    i = 1528
    Do Until pup(i) > pupF
        i = i - 1: Loop: Let pupx2 = i
    i = 0
    Do Until out(i) > outF
        i = i + 1: Loop: Let outx1 = i
    i = 1528
    Do Until out(i) > outF
        i = i - 1: Loop: Let outx2 = i
    For i = 0 To 1528
        Range("d" & Format(i + 2)).Formula = i + 1 + (1000 - (pupx1 + pupx2) / 2)
        Range("e" & Format(i + 2)).Formula = pup(i)
        Range("f" & Format(i + 2)).Formula = i + 1 + (1000 - (outx1 + outx2) / 2)
        Range("g" & Format(i + 2)).Formula = out(i)
    Next i
End Sub

```

The following graph is plotted where both beams are centred about 1000 on the horizontal axis.

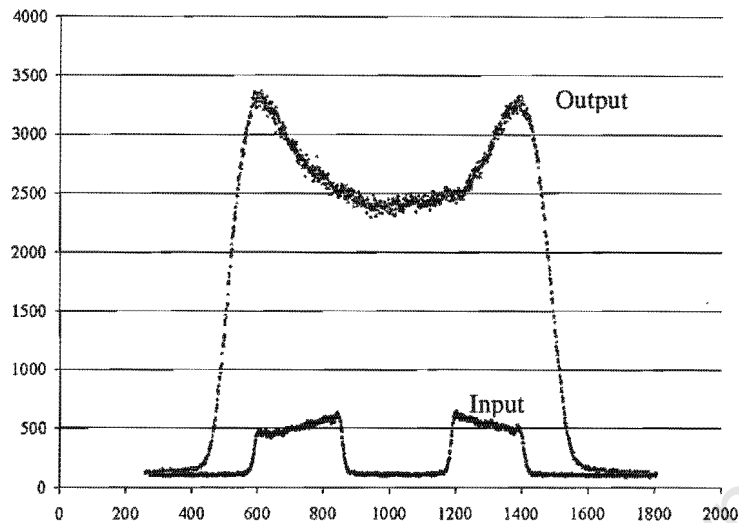


Figure 170: Overplot of the two curves with their centroids coinciding about 1000 on the X-Axis.

Now if we subtract the background and scale to the same flux we get:

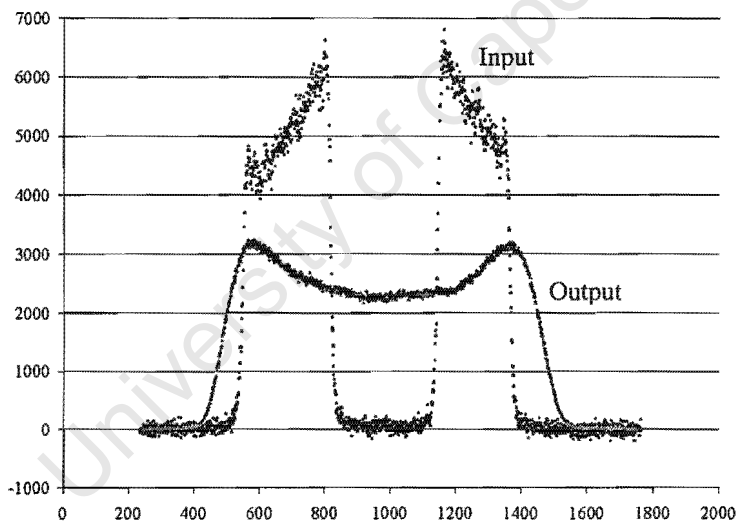


Figure 171: Scaled flux levels, where the areas under both curves are now equal. The scale factor in this case, $k = 13$.

Where the following code is used:

```
Sub start()
    Dim pup(1528), out(1528)
    Sheets("flux").Select
    For i = 0 To 1528
        pup(i) = Range("b" & Format(i + 2))
        out(i) = Range("c" & Format(i + 2))
    Next i
    pupback = Application.WorksheetFunction.Average(Range("b2:b101"))
    outback = Application.WorksheetFunction.Average(Range("c2:c101"))
    pupF = pupback + (puppeak - pupback) / 2
    outF = outback + (outpeak - outback) / 2

```

```

i = 0
Do Until pup(i) > pupF
i = i + 1: Loop: Let pupx1 = i
i = 1528
Do Until pup(i) > pupF
i = i - 1: Loop: Let pupx2 = i
i = 0
Do Until out(i) > outF
i = i + 1: Loop: Let outx1 = i
i = 1528
Do Until out(i) > outF
i = i - 1: Loop: Let outx2 = i
For i = 0 To 1528
    Range("d" & Format(i + 2)).Formula = i + 1 + (1000 - (pupx1 + pupx2) / 2)
    Range("e" & Format(i + 2)).Formula = pup(i) - pupback
    Range("f" & Format(i + 2)).Formula = i + 1 + (1000 - (outx1 + outx2) / 2)
    Range("g" & Format(i + 2)).Formula = out(i) - outback
Next i
fluxpup = Application.WorksheetFunction.Sum(Range("e2:e1530"))
fluxout = Application.WorksheetFunction.Sum(Range("g2:g1530"))
k = 1
Do Until fluxpup > fluxout
    For i = 0 To 1528
        Range("i" & Format(i + 2)).Formula = k * (pup(i) - pupback)
    Next i
    fluxpup = Application.WorksheetFunction.Sum(Range("i2:i1530"))
    k = k + 0.5
Loop
End Sub

```

In the final result $k = 13$, where k is the factor to scale the input beam by so that the area underneath both curves are equal.

Appendix N. BREAKDOWN FOR SUGGESTED TEST RIG

<i>Item</i>	<i>Source</i>	<i>Part Number</i>	<i>Description</i>	<i>Notes</i>
1	NP	M-SA-30 x 30	Solid Aluminium Breadboard	750mm * 750mm, M6 Holes, 25mm Spacing
2	ES	K35-264	Sorbothane Vibrational Mounts	Pack of 4 (Imperial Units)
3	NP	M-443-4	Low Profile Precision Ball Bearings Translation Stage	Range = 102mm
4	NP	M-423	Low Profile Precision Ball Bearings Translation Stage	Range = 25mm
5	NP	SM-50	Vernier Micrometer	Range = 50mm
6	NP	SM-25	Vernier Micrometer	Range = 25mm
7	NP	FP-2	Fibre Optic Positioners	5-Axis
8	ES	K53-907	Zero Aperture Series - Iris Diaphragm	Aperture Range 25.0 - 0.0
9	ES	K54-863	Iris Diaphragm Mount	NB: Imperial Thread
10	ES	K39-485	Pellicle Beamsplitter	Clear Aperture 2inch 50R/50T OD = 2 1/2inch (62.5mm)
11	ES	K03-605	3-Screw Adjustable Ring Mount	ID = 77mm
12	ES	K32-498	Tech Spec Achromatic Lens	d = 30mm f = 75mm, ET = 8.4mm, CT = 11.4mm
13	ES	K45-217	Tech Spec Achromatic Lens	d = 30mm f = 125mm, ET = 5.5mm, f/5 [NOTE #1]
14	ES	K45-415	Tech Spec Achromatic Lens	d = 30mm f = 200mm, ET = 6.5mm [NOTE #2]
15	ES	K54-983	Metric Optic Mount	Max Component Thickness: 12mm
16	ES	K54-937	Mounting Posts - 60mm	(Metric Units)
17	ES	K36-496	SS Mounting Posts - 2.5inch	(Imperial Units)
18	NP	M-VPH-3	Post Holders - 76mm	M6 Thread
19	ES	K39-244	Monochrome High Res **	0.5" 6.4*4.8mm Chip, 1/4-20 mount, Power Supply Included
20	ES	K37-822	Toshiba Monitor	Video In - NTSC/EIA (Y-C), Power In 120V, 60Hz
21			Cable	RCA to Y-C

Table 7: Table of Apparatus, Notes and Descriptions

<i>Item</i>	<i>Source</i>	<i>Part Number</i>	<i>Page</i>	<i>Quantity</i>	<i>Item Price</i>	<i>Price</i>
1	NP	M-SA-30 x 30	OM-15-14	1	\$715.00	\$715.00
2	ES	K35-264	p 106	1	\$15.25	\$15.25
3	NP	M-443-4	OM-17-21	1	\$271.00	\$271.00
4	NP	M-423	OM-17-20	1	\$215.00	\$215.00
5	NP	SM-50	OM-16-10	2	\$175.00	\$350.00
6	NP	SM-25	OM-16-10	1	\$88.00	\$88.00
7	NP	FP-2	P-6-29	4	\$349.00	\$1,396.00
8	ES	K53-907	p 125	1	\$44.00	\$44.00
9	ES	K54-863	p 125	1	\$26.00	\$26.00
10	ES	K39-485	p 59	1	\$217.00	\$217.00
11	ES	K03-605	p 116	1	\$60.00	\$60.00
12	ES	K32-498	p 29	2	\$55.20	\$110.40
13	ES	K45-217	p 29	1	\$55.20	\$55.20
14	ES	K45-415	p 29	1	\$55.20	\$55.20
15	ES	K54-983	p 115	4	\$33.75	\$135.00
16	ES	K54-937	p 110	8	\$9.00	\$72.00
17	ES	K36-496	p 111	3	\$10.50	\$31.50
18	NP	M-VPH-3	OM-14-2	10	\$13.50	\$135.00
19	ES	K39-244	p 209	1	\$385.00	\$385.00
20	ES	K37-822	p 213	1	\$330.00	\$330.00
21						

Table 8: Table of apparatus, costs.

Note:

1. NP: *NEWPORT* 1999/2000 Catalogue:
 - a. OM: Optics & Mechanics.
 - b. P: Photonics.
 2. ES: Edmund Scientific Optics 2000 Catalogue.
 3. Assuming the availability of filters, microscope objectives and mounts to construct the source assembly in this design.
- NOTE #1 $f/5$ chosen to ensure that the exiting light from the source fibre expands to full beam diameter, also a microscope objective is used to launch the light into the source fibre because it has a small f -number and will excite a large number of modes in the fibre.
 - NOTE #2 $f = 200$ will result in a magnification of 2.67, assuming a max cladding diameter of $\sim 700\mu\text{m}$, this will result in an image on the chip of $\sim \phi 2\text{mm}$.

University of Cape Town

REF E R E N C E S

- Avila, G. & S. D'Odorico, (1993). Fibre Optics in Astronomical Instruments at ESO, *ASP Conf Series*, **37**, pp.90-105.
- Barden, S.C., et al, (1993). Hydra – Kitt Peak Multi-Object Spectroscopic System, *ASP Conf Series*, **37**, pp.185-202.
- Barden, S.C., (1993). Fibre Optics in Astronomy II - Conference Overview, *ASP Conf Series*, **37**, pp.410-414.
- Barden, S.C., (1995). Review of Fiber Optic Properties for Astronomical Spectroscopy. *Proc. SPIE*, **2476**, pp.2-9.
- Barden, S.C., (1998). Review of Fibre-Optic Properties for Astronomical Spectroscopy. *ASP Conf Series*, **152**, pp.14-19.
- Barwig, H., et al, (1998). The Impact of Fiber Optics on Photometry: the Design of Two High-Speed Multi-Channel Instruments, *ASP Conf Series*, **152**, pp.320-328.
- Bedding, T., P. Gray & F. Watson, (1993). *AUTOFRED*: A Robotic Fibre Positioner for *FLAIR II*, *ASP Conf Series*, **37**, pp.181-184.
- Bell, A.G., (1880). Selenium and the photophone. *The Electrician*, pp.214,215,220,221 cited by Senior, J.M., (1985). *Optical Fiber Communications, Principles and Practice* (P.J. Dean, Ed), Prentice-Hall, London.
- Barna, J.W., (1998). The Hobby-Eberly Telescope, Introduction: Simplicity, Complexity, Simplicity, in Sebring, T.A., (1998). *West Texas Time Machine: Creating the Hobby-Eberly Telescope*, Little Hands of Concrete, Austin. pp.9-24.
- Baruch, J.E.F., et al, (1988). Developments in Fibre-Optic Techniques for Spectro-Photometry on Large Telescopes, *ASP Conf Series*, **3**, pp.195-201.
- Booth, J.A., et al, (2000). Development of the Segment Alignment Maintenance System (SAMS) for the Hobby-Eberly Telescope, *Proc SPIE*, **4003**, pp.176-187.
- Buckley, D.A.H., (2000). The Southern Africa Large Telescope (SALT) and the potential for galactic dynamical studies, *Astrophysics & Space Science*, **269-270**, pp.549-555.
- Buckley, D.A.H., D. O'Donoghue, N.J. Sessions, K.H. Nordsieck, (2000). Instrumentation Options for the Southern African Large Telescope (SALT), *Proc. SPIE*, **4008**, p.72.
- Buckley, D.A.H. & N.J. Sessions, (2000). *A Concept Proposal for a Fibre Instrument Feed for SALT*.
- Cherin, A.H., (1983). *An Introduction to Optical Fibers* (T.M. Slaughter, Ed), McGraw-Hill, New York.
- Einarsson, G.H., (1996). *The Principles of Lightwave Communications*, John Wiley & Sons, Chichester.
- Fabricant, D.G., (1988). The DECASPEC: A Fiber Optics Manipulator for Multi-Object Spectroscopy, *ASP Conf Series*, **3**, pp.170-173.
- Ferroperm, (2001). url: <http://www.ferroperm.com/>
- Geary, J.C., et al, (1986). A Faint-Object Grism Spectrograph with Multiple Slits and CCD Detector, *Proc. SPIE*, **627**, pp.509-516.
- Gillingham, P., et al, (2000). ECHIDNA – A Multi-Fibre Positioner for the Subaru Prime Focus, *Proc. SPIE*, **4008**, pp.1395-1403.
- Gray, P. M., (1986). Anglo-Australian Observatory Fibre System. *Proc. SPIE*, **627**, pp.96-104.
- Gray, P.M., (1988). Fiber Optics in Astronomy – Conference Overview, *ASP Conf Series*, **3**, pp.285-291.
- Green, R.E., Ed., (1992). *Machinery's Handbook* (24th Ed.), Industrial Press Inc, New York, p225-226.
- Heacox, W.D., (1986). On the Application of Optical-Fibre Image Scramblers to Astronomical Spectroscopy, *Astron.J.*, **92**, pp219-229.
- Heacox, W.D., (1988). Wavelength-Precise Slit Spectroscopy with Optical Fibre Image Scramblers, *ASP Conf Series*, **3**, pp.204-236.
- Hecht, E., (1987). *Optics* (2nd Ed.), Addison-Wesley, USA.
- Hill, J.M., et al, (1980). Multiple Object Spectroscopy: The Medusa Spectrograph, *ApJ*, **246**, L69-72.
- Hill, J.M., et al, (1982). Multiple Object Fiber Optic Spectroscopy, *Proc. SPIE*, **331**, pp.279-288.
- Hill, J.M. & M.P. Lesser, (1986). Deployment of the MX Spectrometer, *Proc. SPIE*, **627**, pp.303-320.
- Hill, J.M., (1988). The History of Multiobject Fiber Spectroscopy, *ASP Conf Series*, **3**, pp.77-92.
- Hoag, A.A., (1976). Faint Blue Objects in the Field of M67. *Pub ASP*, **88**, pp.860-864.
- Hodgson, D.E., et al, (1999). Shape Memory Alloys, url: <http://www.sma-inc.com/SMAPaper.html>
- Horner, S.D., L.W. Ramsey & L.G. Engel, (1997). Fibre Instrument Feed Critical Design Review, HET.
- Horner, S.D., L.G. Engel & L.W. Ramsey, (1998a). The Hobby-Eberly Telescope Fibre Instrument Feed, *ASP Conf Series*, **152**, pp.247-252.
- Horner, S.D., L.G. Engel & L.W. Ramsey, (1998b). The Hobby-Eberly Telescope Medium Resolution Spectrometer and Fibre-Instrument-Feed, *Proc. SPIE*, **3355**, pp.399-408.
- Hunter, T.R. & L.W. Ramsey, (1992). Scrambling Properties of Optical Fibers and the Performance of a Double Scrambler. *Pub ASP*, **104**, pp.1244-1251.
- Keck, D.B., (1976). Optical Fibre Waveguides, in *Fundamentals of Optical Fibre Communications*, ed. M.K. Barnoski, Academic Press, New York.

- Kleindiek, S., (2000). Kleindiek Nanotechnik, url: <http://hanotechnik.com/>
- Krisciunas, K., (1988). *Astronomical Centres of the World*, Cambridge University Press, Cambridge. p.248.
- Lewis, I.J., K. Glazebrook & K. Taylor, (1998). The Anglo-Australian Observatory 2dF Project: A Status Report after the first year of Scientific Operation, *Proc. SPIE*, 3355, pp.828-833.
- Lu, G., et al, (1998). Optical Fibre for UV-IR Broadband Spectroscopy, *Proc. SPIE*, 3355, pp.884-891.
- Mantel, K.H., et al, (1993). The MEKASPEK Project – A New Step Towards the Utmost Photometric Accuracy, *Proc. IAU Coll.*, 136, pp.172-177.
- Mantel, K.H., (1999). Multi-Channel Spectrophotometer MEKASPEK, url: <http://bigbang.usm.uni-muenchen.de:8002/USM/WDST/inst/meka/>
- Mertz, L.N., (1996). *Excursions in Astronomical Optics*, Springer-Verlag, New York, p.5.
- Nagel, S.R., (1993). Lightwave Communications Using Optical Fibers. E12. Printed In Halliday, D., R. Resnick, & J. Walker, (1993). *Fundamentals of Physics, Extended* (4th Ed.), John Wiley & Sons, USA.
- Nelson, G.W., (1988). Introduction to Fiber Optics. *PASP*, 3, pp.2-22.
- Nof, S.H., Ed., (1999). *Handbook of Industrial Robotics* (2nd Ed.), John Wiley & Sons, New York. p.91-2.
- O'Donoghue, D., (2000). The Correction of Spherical Aberration in the Southern African Large Telescope (SALT), *Proc. SPIE*, 4003, pp.363-372.
- Parker, Q.A. & F.G. Watson, (1995). *FLAIR* System Users Guide - Part 1. (http://www.ast.cam.ac.uk/AAO/local/www/cgt/flair_manual/part1.html).
- Parker, S.P. Ed, (1997). *McGraw-Hill Dictionary of Astronomy*, McGraw-Hill, USA.
- Parry, I. R. & P.M. Gray, (1986). An Automated Multiobject Fibre Optic Coupler for the Anglo-Australian Telescope, *Proc. SPIE*, 627, pp.118-124.
- Parry, I.R. & R.M. Sharples, (1988). AUTOFIB – Current Status, *ASP Conf Series*, 3, pp.93-97.
- Parry, I.R., (1998). The Astronomical Uses of Optical Fibers, *ASP Conf Series*, 152, pp.3-13.
- Physik Instrumente, (2001). url: physikinstrumente.com
- Pitz, E., (1988). Multi-Object Fibre Feed "Spaltspinne", *ASP Conf Series*, 3, pp.163-169.
- Pitz, E., (1993). The Multi-Object Fibre Feed "Spaltspinne" – Final Hardware Report, *ASP Conf Series*, 37, pp.20-25.
- Pitz, E., et al, (1993). The Tautenburg "Feldspinne", *ASP Conf Series*, 37, pp.166-170.
- Ramsey L. W., (1995). Hobby-Eberly Telescope Medium Resolution Spectrograph, *Proc SPIE*, 2476 ,pp.20-32.
- Ramsey L.W., (1988). Focal Ratio Degradation in Optical Fibers of Astronomical Interest. *ASP Conf Series*, 3, pp.26-40.
- Ramsey, L.W., (1998). Fiber-Optic Instrumentation and the Hobby-Eberly Telescope, *ASP Conf Series*, 152, pp.235-246.
- Ramsey, L.W., et al, (1998). The early performance and present status of the Hobby-Eberly telescope, *Proc. SPIE*, 3352, pp.34-42.
- Ridpath, I., Ed, (1997). *A Dictionary of Astronomy*, Oxford University Press, Oxford.
- Sessions, N.J., D.A.H. Buckley & B.I. Reed, (2000). Fibre Instrument Feed for the Southern African Large Telescope (SALT), *Proc. IFAC*, pp.283-288.
- Shape Memory Applications, (1999). url: www.sma-inc.com
- Stobie, R.S., (1998). 'The Plans and Status of SALT', Science with SALT: proceedings of the SALT/HET Workshop (Buckley, D.A.H, Ed). pp.9-17.
- Stobie, R.S., et al, (1999). SALT Collateral Benefits Plan Draft, 8th July.
- Stobie, R.S., et al, (2000). Design of the Southern African Large Telescope, *Proc SPIE*, 4003, pp.355-362.
- Stone, J., (1972). Optical Transmission in Liquid-Core Quartz Fibers. *AppPhysL*, 20, pp.239-240.
- TiNi Alloy Company, (2000). url: www.sma-mems.com
- Tubbs, E.F., et al, (1982). Multiple Object Fiber Optics Spectrograph Feed for the Hale Telescope, *Proc. SPIE*, 331, pp.289-295.
- Watson, F.G., (1986). A Wide-Field Multi-Object Spectroscopy (MOS) System, *Proc. SPIE*, 627, pp.787-796.
- Watson, F.G., (1988). Multi-Object Spectroscopy with *FLAIR*, *ASP Conf Series*, 3, pp.125-132.
- Watson, F.G., et al, (1993). A Second Generation *FLAIR* System, *ASP Conf Series*, 37, pp.171-180.
- Weik, M.H., (1989). *Fiber Optics Standard Dictionary* (2nd Ed.), Van Nostrand Reinhold, New York.

University of Cape Town

University of Cape Town